Supporting Information

Single-Crystalline Twelve-Connected Nanographene-Based Covalent Organic Frameworks

Saber Mirzaei,[1‡] M. Saeed Mirzaei,[1,2‡] Mei-Yan Gao,[1] Felipe Gándara,[3] Kaiyu Wang,[1] Francesco Tavani,[1,4] Heqing Zhu,[1,5] Davide M. Proserpio,[6] and Omar M. Yaghi[1*]

[1]*Department of Chemistry, University of California, Berkeley, Berkeley, California 94720, United States.*
[2]*Department of Food Science, College of Agriculture and Life Sciences, Cornell University, Ithaca, NY, 14853, United States.*
[3]*Instituto de Ciencia de Materiales de Madrid (ICMM-CSIC), Sor Juana Inés de la Cruz 3, 28049 Madrid, Spain.*
[4]*Dipartimento di Chimica, Università degli Studi di Roma La Sapienza, P.le A. Moro 5, I-00185 Rome, Italy.*
[5]*Materials Sciences Division, Lawrence Berkeley National Laboratory, Berkeley, California 94720, United States.*
[6]*Dipartamento di Chimica, Universita degli Studi di Milano, Milano 20133, Italy.*

[‡]*These authors contributed equally.*

**Correspondence: yaghi@berkeley.edu (O.M.Y.)*

Table of Contents

Supplemental Methods

S1. General Experimental Methods and Materials

Chemicals. Triflouoacetic acid (≥ 99.0%) was purchased from Honeywell. Glacial acetic acid, aniline, tetrakis(triphenylphosphine)palladium(0) (99%), 1,4-Dioxane (ACS reagent, ≥ 99.0%), and tetrahydrofuran (THF, ACS reagent, ≥ 99.0%), were purchased from Sigma-Aldrich Co. Acetone (AR, ≥ 99.9%), dichloromethane (DCM, ACS reagent, ≥ 99.5%), ethyl acetate (ACS reagent, ≥ 99.5%), and methanol (AR, ≥ 99.8%) were purchased from Fisher Scientific. 4-formylphenylboronic acid, 2,3,6,7,14,15-hexakis(4-aminophenyl)triptycene (**HAPT**) and 1,3,6,8-Tetrakis(4-aminophenyl)pyrene (**PyTTA**) were purchased from Ambeed and were used as received.

Solution-state Nuclear Magnetic Resonance Spectroscopy (NMR). Solution-state nuclear magnetic resonance (NMR) spectroscopy experiments were conducted at 500 MHz for ^{1}H and 125 MHz for ^{13}C using a Bruker spectrometer equipped with an Avance-III console. Chemical shifts were referenced using the solvent resonances as internal standards (δ ^{1}H: 7.26 ppm for $CDCl_3$; δ ^{13}C: 77.16 ppm for $CDCl_3$; δ ^{1}H: 2.50 ppm for DMSO-d_6; δ ^{13}C: 39.51 ppm for DMSO-d_6).

Solid-State Nuclear Magnetic Resonance Spectroscopy (ssNMR).

^{1}H and ^{13}C solid-state NMR spectra were recorded at B_0= 9.4 T (400.2 MHz for ^{1}H) using a Bruker BioSpin spectrometer equipped with an AVANCE NEO console and a 3.2 mm double resonance HX magic angle spinning probe tuned to both ^{1}H (400.2 MHz) and ^{13}C (100.6 MHz). Samples were loaded in 3.2 mm zirconia rotors and closed using Vespel® caps. Samples were spun at the magic angle at νR = 20 kHz using dry nitrogen. ^{1}H and ^{13}C chemical shifts were referenced with respect to tetramethylsilane using the CH resonance of adamantane as a secondary external reference at $\delta_{iso}(^{13}C)$ = 38.48 ppm and $\delta_{iso}(^{1}H)$ = 1.8 ppm.

The $^{1}H \rightarrow ^{13}C$ CP transfer used a contact time τ_{CP}, during which a constant RF-field equal to 68 kHz was applied on the ^{13}C, while the ^{1}H RF-field amplitude was linearly ramped from 84.4 to 93.74 kHz. CP contact time (τ_{CP}) used was 2 ms. During ^{13}C acquisition, high-power ^{1}H decoupling was applied using the SPINAL-64 (Small Phase Incremental Alternation with 64 steps)[1] decoupling scheme with an RF-field amplitude set to 84.75 kHz.

Single-component Sorption Isotherm Measurements. N_2 and Ar sorption isotherms at 77 K and 87 K were measured using a Micromeritics ASAP 2420 Accelerated Surface Area and Porosimetry System. Powder samples were activated under a dynamic vacuum using a Micromeritics ASAP 2420 Accelerated Surface Area and Porosimetry System before measurement. A liquid nitrogen or liquid Ar bath was used to maintain a temperature at 77 or 87 K for each measurement. Ultra-high-purity (Praxair, 99.999%) N_2, Ar and He gases were used throughout the adsorption experiments.

Powder X-ray Diffraction (PXRD). PXRD patterns were collected using a Bruker D8 Advance X-ray diffractometer equipped with a Cu anode and a Ni filter (Cu Kα, λ = 1.5406 Å) in Bragg-Brentano geometry. The samples were mounted on a zero-background holder and leveled using a glass slide. The step size was 0.02° with an exposure time of 2 s per step.

Synchrotron PXRD measurements were performed using a wavelength of 0.1665 Å on beamline 28-ID-1 at the National Synchrotron Light Source (NSLS-II), Brookhaven National Laboratory. Calibration of the PXRD patterns was performed with CeO_2 powder as a standard, and pyFAI[2] was employed for azimuthal integration. The samples were loaded into 1.0 mm Kapton tubes prior to data collection.

Single Crystal X-ray Structure (SCXRD). SCXRD measurements were conducted on a Rigaku XtaLab P200 diffractometer equipped with dual-beam microfocus Cu Kα X-ray radiation sources paired with a Pilatus3 R 200K-A Shutterless Detector. Single crystals suitable for X-ray structure analysis were mounted on a Kapton MiTeGen MicroMount, minimally coated with Paratone N oil, and placed within a cold gas stream generated by an Oxford Cryosystems 800 Series Cryostream. Data from Rigaku's diffractometer was integrated and corrected using CrysAlisPro software (version 1.171.43.143a, Rigaku Oxford Diffraction, 2024). Absorption corrections were applied using SADABS.[3] Space groups were assigned based on analysis of systematic absences and E-statistics, and confirmed through successive structure refinements. PLATON[4] was employed to check for missed higher symmetry and to identify potential twinning. Structural solutions were achieved through SHELXT intrinsic phasing, and subsequent refinement was accomplished by full-matrix least squares on F^2 using SHELXL within the Olex2 software package.[5-7] The SQUEEZE option of PLATON was used to eliminate the contribution of disordered guest molecules to the reflection intensities.[8] Crystallographic data reported in this paper is summarized in Tables S1. These crystal structures have been deposited into the Cambridge Crystallographic Data Centre (CCDC).

COF-612: The structure was refined in the hexagonal space group $P\bar{6}c2$ (no. 188), with unit cell parameters $a = b = 38.024(2)$ Å, $c = 31.110(4)$ Å, and V = 38953(6) Å³ (Table S1). Data were truncated at a resolution of 1.6 Å, as I/σ(I) values beyond this limit fall below 2 and are therefore statistically insignificant. Given this limited resolution, several constraints were applied during the refinement. Phenyl rings were refined as freely rotating groups with idealized geometry (AFIX 66), with equivalent anisotropic displacement parameters (ADPs) imposed on all atoms within each ring. Additionally, a solvent mask was applied to account for disordered electron density in the pore channels. All non-hydrogen framework atoms were located in the difference Fourier maps, with the exception of those involved in the imine bond. In this case, only a single electron density maximum could be identified, at a position corresponding to the midpoint of the expected C=N bond. This is consistent with the experimental resolution, which is insufficient to resolve the individual atomic positions across a carbon–nitrogen double bond (~1.28 Å). Based on this solution, a geometrically complete structural model was obtained by force-field optimization using the Universal Force Field (UFF) as implemented in Materials Studio.

Elemental Microanalysis. Elemental analysis was performed in the Microanalytical Laboratory of the College of Chemistry at UC Berkeley, using a Perkin Elmer 2400 Series II CHNS elemental analyzer.

UV-Vis Absorption Spectroscopy (UV-Vis). The optical absorption spectrum was acquired using a UV-Vis spectrometer (UV-2600, Shimadzu). A background scan was conducted solely for the quartz slides before performing measurements.

Photoluminescence Spectroscopy (PL): PL spectra were collected by a home-built photoluminescence spectroscopy system. A continuous-wave solid-state laser at 375 nm (Coherent OBIS 375LX) was focused obliquely onto the sample as the excitation source. An excitation filter (bandpass, 375 nm/6 nm) was used to narrow the laser emission linewidth. PL images were captured using a microscope objective (50x, numerical aperture [NA] = 0.55) before being sent to the grating-based spectrograph (Princeton Instruments, SP-2300i) through an optical fiber for spectrum analysis. A 390-nm longpass filter was used to filter out the laser signal. The spectrograph was equipped with a diffraction grating of 150 lines/mm and coupled with a charge-coupled device (CCD) detector with optimized detection efficiency by liquid nitrogen cooling to -120℃.

Thermogravimetric Analyses (TGA). TGA curves were recorded on a TA Q600 thermal analysis system under nitrogen flow, ramping at 10 °C min^{-1} from room temperature (typically 25 °C) to 800 °C. Ultrahigh-purity-grade N_2 was used for all TGA measurements.

Fourier-transform infrared (FT-IR) Spectra.

FT-IR spectra were collected on a Bruker ALPHA Platinum ATR-FT-IR Spectrometer equipped with a single reflection diamond ATR module. Spectra were collected on the neat samples and at room temperature (25 °C). Spectra are plotted in transmittance (%) against the wavenumbers (cm^{-1}).

S2. Synthesis of compounds

***Scheme S1*. The general synthetic approach.**

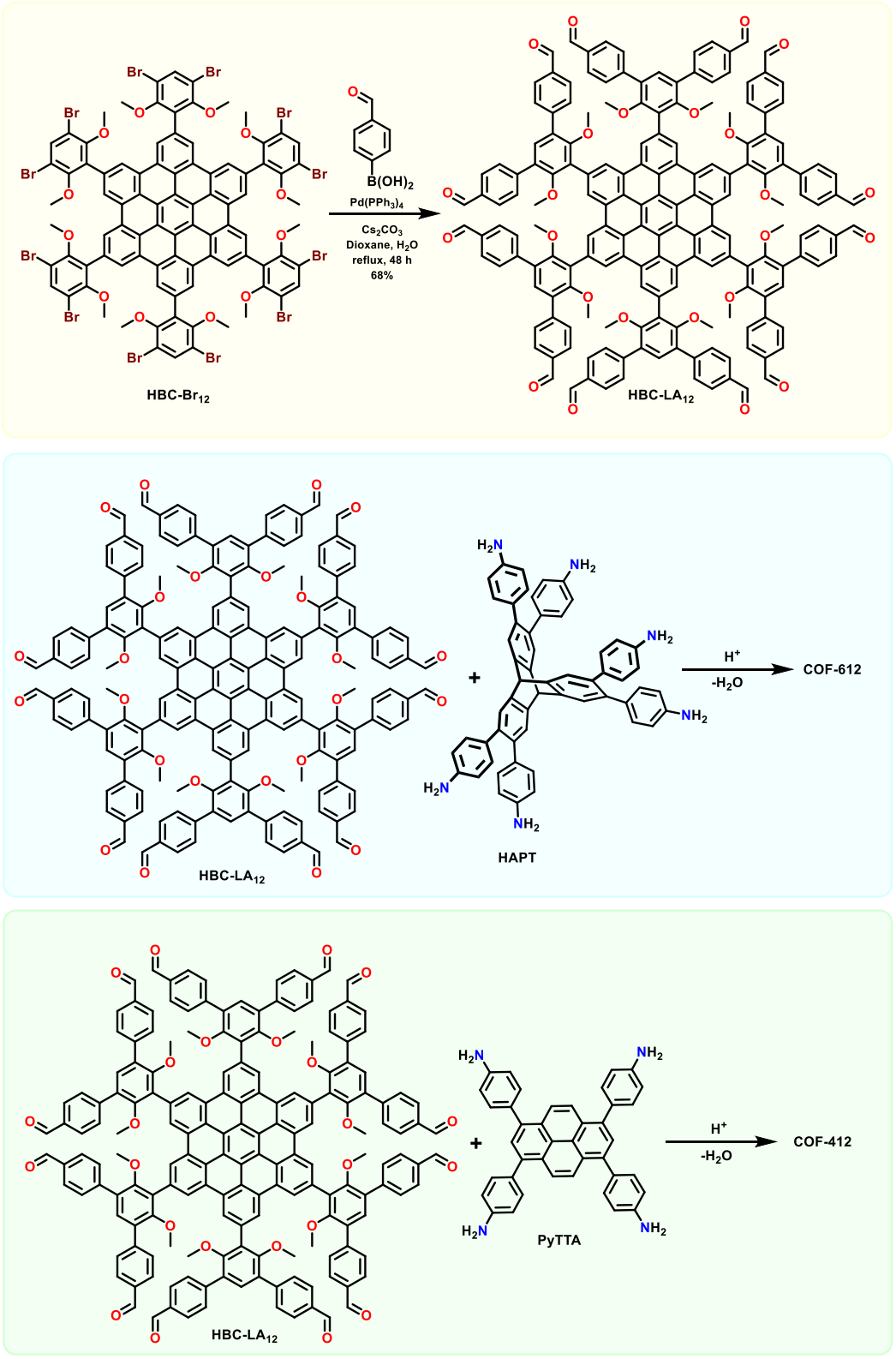

Synthesis of compound **HBC-LA$_{12}$**:

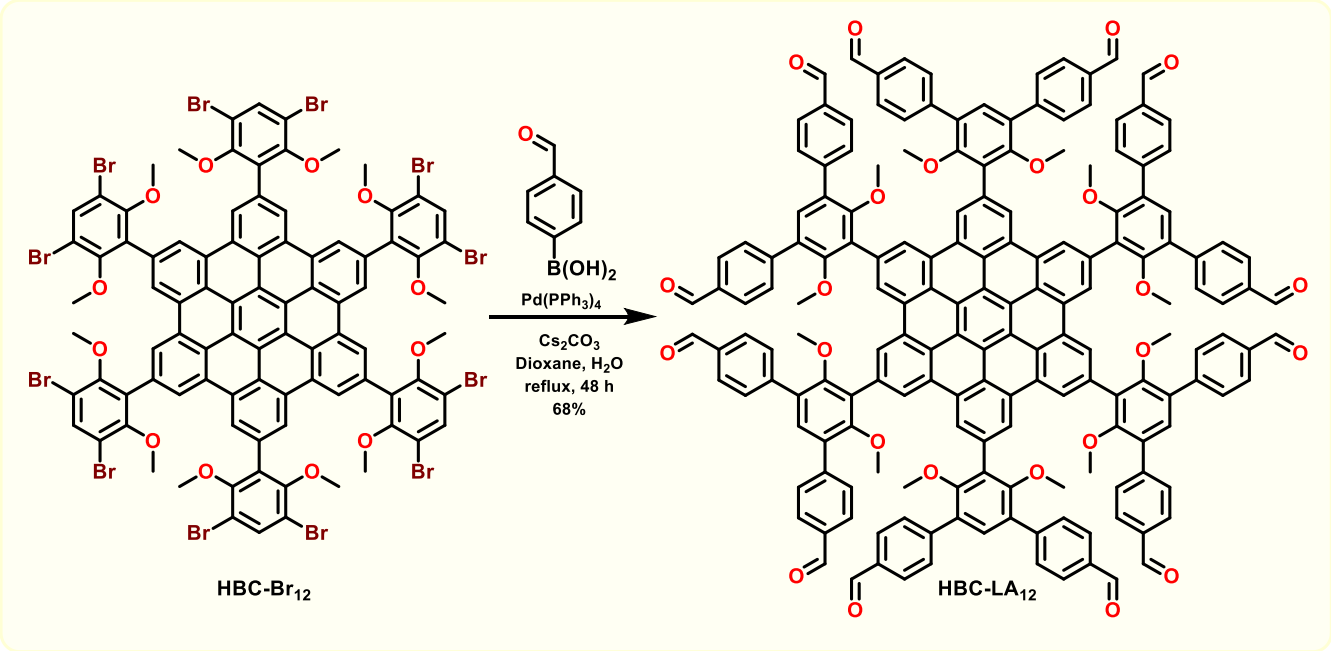

HBC-Br$_{12}$ was synthesized according to the reported procedure.[9] In a 500 mL Schlenk flask, HBC-Br$_{12}$ (3.0 g, 1.32 mmol), 4-formylphenylboronic acid (4.5 g, 48.11 mmol, 36.5 equiv.), and Cs_2CO_3 (7.0 g) were combined. The flask was evacuated and backfilled with nitrogen, after which 1,4-dioxane (200 mL) and water (20 mL) were added. The reaction mixture was degassed for 30 min under stirring at 40 °C using an oil bath. $Pd(PPh_3)_4$ (0.6 g, 0.52 mmol, 0.6 equiv.) was then added, and the mixture was degassed for an additional 15 min. The reaction was heated to 110 °C under a nitrogen atmosphere with a condenser connected to an oil bubbler and maintained under these conditions for 48 h. After cooling to room temperature, the solvent was removed under reduced pressure. The residue was washed with water and methanol, dissolved in dichloromethane, and purified by flash column chromatography on silica gel using dichloromethane followed by 30% ethyl acetate in hexanes to remove impurities. Final elution with 5% methanol in dichloromethane afforded the desired product as a brown solid, which was further washed with methanol. Yield: 68% (2.3 g, 0.89 mmol). High-quality single crystals of HBC-LA$_{12}$ were obtained by slow evaporation from dioxane.

^{1}H NMR (500 MHz, $CDCl_3$, 20 °C): δ 10.10 (s, 2H), 9.58 (s, 2H), 8.01 (d, 4H), 7.92 (d, 4H), 7.60 (s, 1H), and 3.36 (s, 6H) ppm.

^{13}C NMR (125 MHz, $CDCl_3$, 20 °C): δ 192.0, 156.8, 144.3, 135.6, 133.3, 132.7, 131.1, 130.9, 130.1, 130.0, 1253, 124.8, 121.9 and 61.5 ppm.

Elemental analysis for $C_{198}H_{162}O_{36}$: calculated C 80.73%, H 4.44%; found C 78.86%, H 4.52%.

Synthesis of **COF-612**:

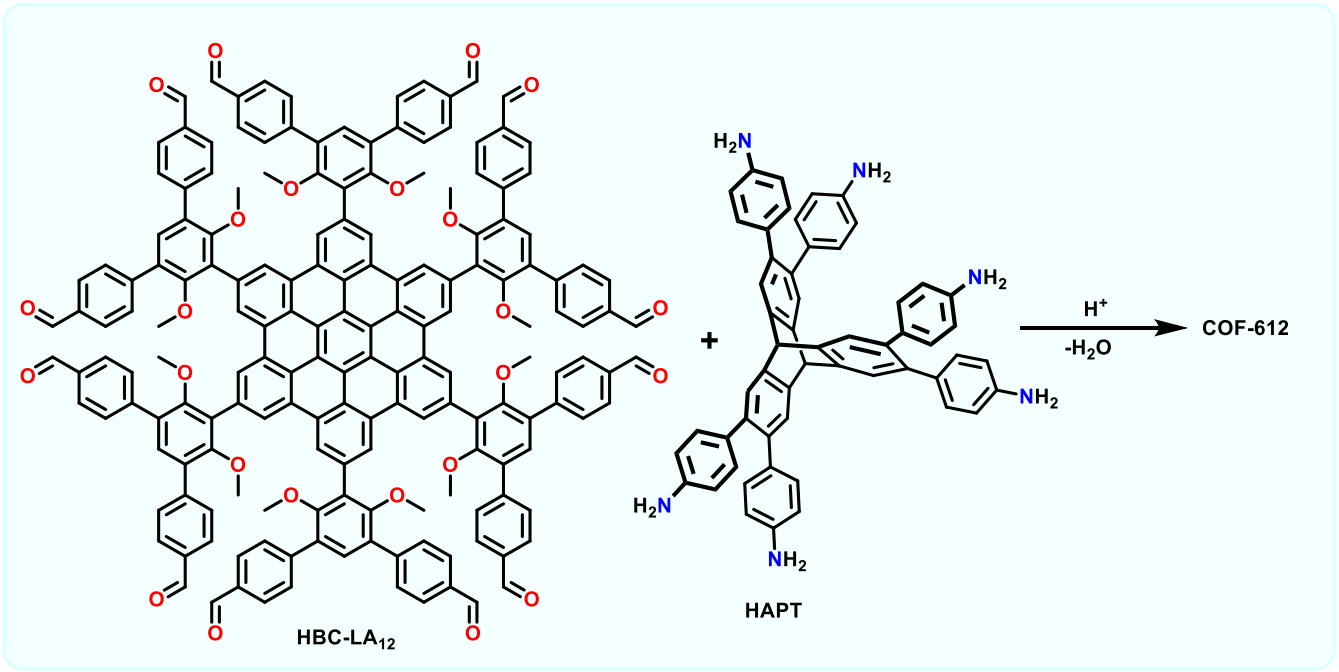

Method A:

In a 20 mL scintillation vial, HBC-LA_{12} (100 mg, 0.039 mmol) was dissolved in 5 mL THF. Then, aniline (1 ml, 282 equiv.) and 1 mL of CH_3COOH (glacial) were added. 2,3,6,7,14,15-hexakis(4-aminophenyl)triptycene (HAPT) (62 mg, 0.077 mmol, ~2.0 equiv.) was dissolved in tetrahydrofuran (5 mL) and added to the solution. The mixture was allowed to stand at 40 °C for 12 days. The crystal size reached ~25 μm after this time. The as-synthesized crystals were immersed in fresh THF (15 mL) for 6 h and the process repeated three times to exchange the guest molecules in the pores and were then exchanged with methanol (15 mL) for three times and subjected to supercritical CO_2 ($scCO_2$) drying process. The activated sample was then used for characterizations without further purification. Yield: 94 mg, 60%.

Elemental analysis for $C_{286}H_{178}N_{12}O_{12}$: calculated C 86.43%, H 4.51%, N 4.23%; found C 79.75%, H 4.92%, N 3.94%.

Method B (larger crystal synthesis):

In a 20 mL scintillation vial, HBC-LA_{12} (25 mg, 0.0096 mmol) was dissolved in 3.75 mL of THF. Then, 0.5 mL of CF_3COOH (6.0 M) and aniline (0.5 ml, 1146 equiv.) were added. HAPT (15.5 mg, 0.019 mmol) was dissolved in THF (3.75 mL) and added to the solution. The mixture was allowed to stand at room temperature. The brown single crystals of COF-612 were crystallized, and the crystal size reached ~20 μm in one day and ~100 μm after four days. The as-synthesized crystals were immersed in fresh THF (15 mL) for 6 h and the process repeated three times to exchange the guest molecules in the pores and were then exchanged with methanol (15 mL) for three times and subjected to supercritical CO_2 ($scCO_2$) drying process. The activated sample was then used for characterizations without further purification. Yield 28%.

Synthesis of **COF-412**:

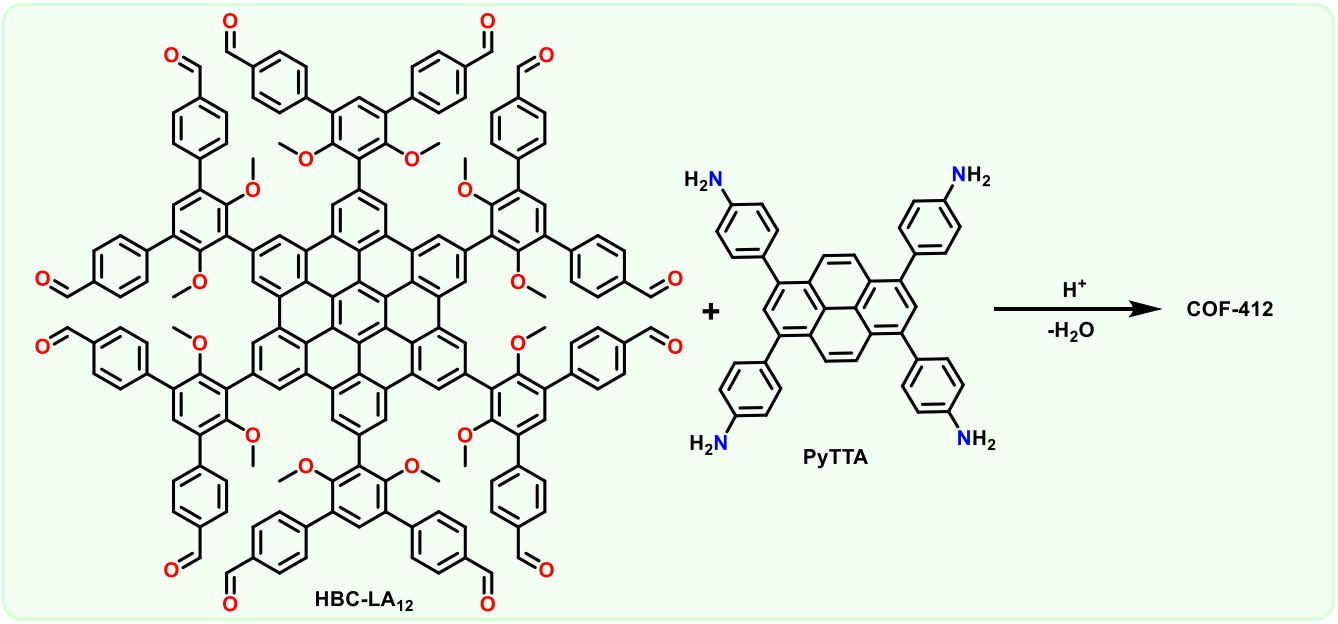

In a 20 mL scintillation, HBC-LA_{12} (32 mg, 0.0124 mmol) was dissolved in 6 mL of THF. Then, 0.8 mL of 6.0 M TFA and aniline (0.6 ml, 520 equiv.) was added. 1,3,6,8-Tetrakis(4-aminophenyl)pyrene (PyTTA) (21.0 mg, 0.0371 mmol, 3.0 eq.) was dissolved in 6 mL THF and added to the solution at once and immediately after the addition of aniline. The mixture was allowed to stand at room temperature. [CAUTION] The chemicals should be added in the order indicated. Otherwise, considerable amorphous precipitate may form. The greenish single crystals of COF-412 were obtained, and the crystal size reached ~10 μm after 24 hours. After 3 days, the solvent was carefully decanted. The solid was then soaked in THF (15 mL) for 3 h, and the supernatant was decanted. This soaking/decantation process was repeated twice more with fresh THF. The solid was subsequently soaked in methanol (MeOH, 15 mL) for 3 h, and the supernatant was decanted; this was repeated twice more with fresh MeOH. The washed material was dried using scCO2 activation to afford the product as a greenish-brown solid. Yield: 23 mg, 47%. Note: 0.8 mL of aniline yields crystals up to ~30 μm after four days, though the yield decreases to ~15%.

Elemental analysis for $C_{294}H_{180}N_{12}O_{12}$: calculated C 86.70%, H 4.45%, N 4.13%; found C 81.46%, H 5.00%, N 3.85%.

S3. Crystal data and structure refinement

Table S1. Crystallographic data for **HBC-LA$_{12}$** and **COF-612**.

	HBC-LA$_{12}$	**COF-612**
CCDC Number	2531485	2541218
Chemical formula	$C_{103}H_{89}O_{20}$	$C_{265}N_6O_{12}$
Formula weight	1646.74	3458.71
Space group	*P–1*	*P–6c2*
***a* (Å)**	9.2711(2)	38.024(2)
***b* (Å)**	26.2949(4)	38.024(2)
***c* (Å)**	26.3344(4)	31.110(4)
***α* (deg)**	61.892(2)	90
***β* (deg)**	80.2790(10)	90
***γ* (deg)**	85.507(2)	120
***V* (Å^3)**	5581.41(19)	38953(6)
Z	2	2
μ (mm^{-1})	0.552	0.146
T (K)	100	100
***R*$_1$ (*wR*$_2$)**	0.0865 (0.2976)	0.1074 (0.3538)
Reflections collected	122048	47009
Goodness-of-fit on F^2	1.072	1.332
Radiation type	Cu Kα	Cu Kα

Figure S1. The molecular crystal structure of HBC-LA_{12}. Thermal ellipsoids are set at 50% probability level. Hydrogen atoms and solvent molecules are omitted for clarity.

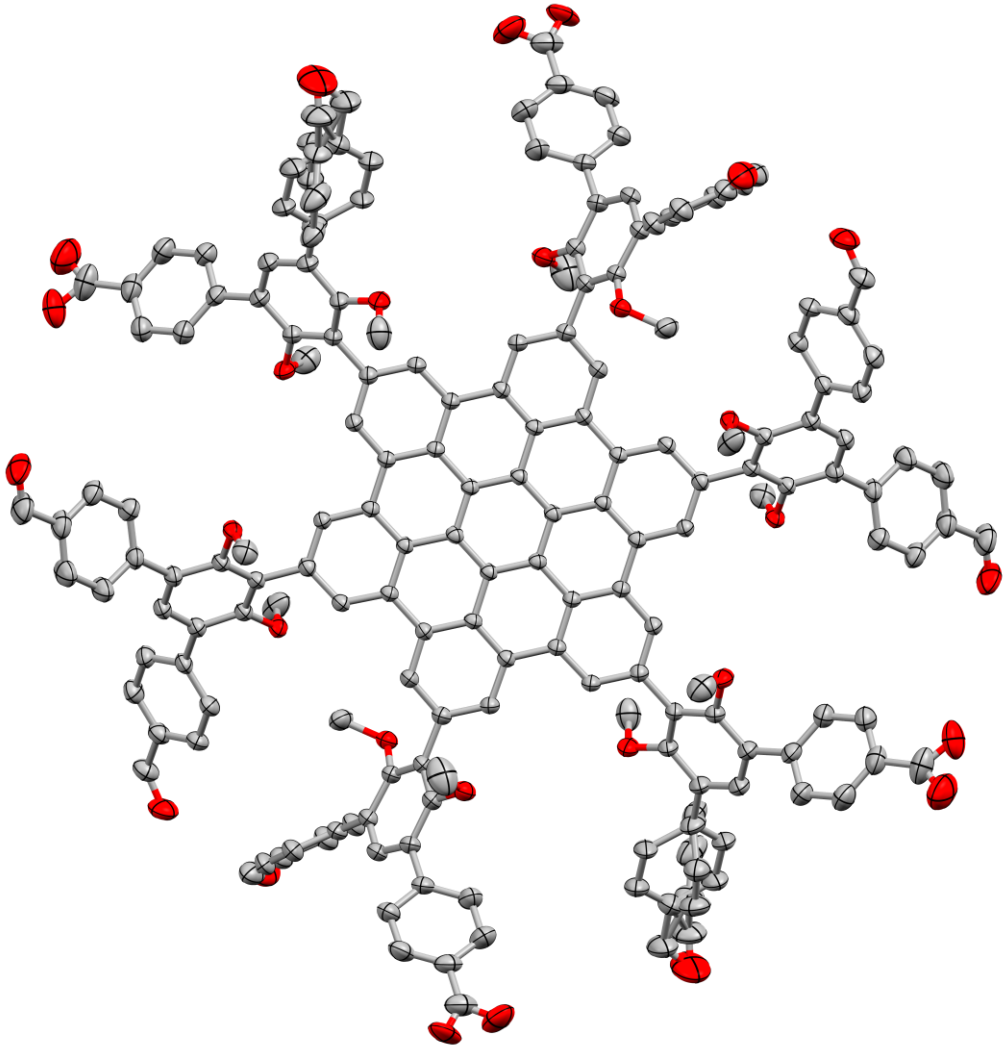

Figure S2. The least-squares-fit planes of HBC-LA_{12} defined by the HBC core unit and phenyl rings are shown. The value is the average of three dihedral angles (~51°); the smallest and largest angel is 47° and 58°, respectively.

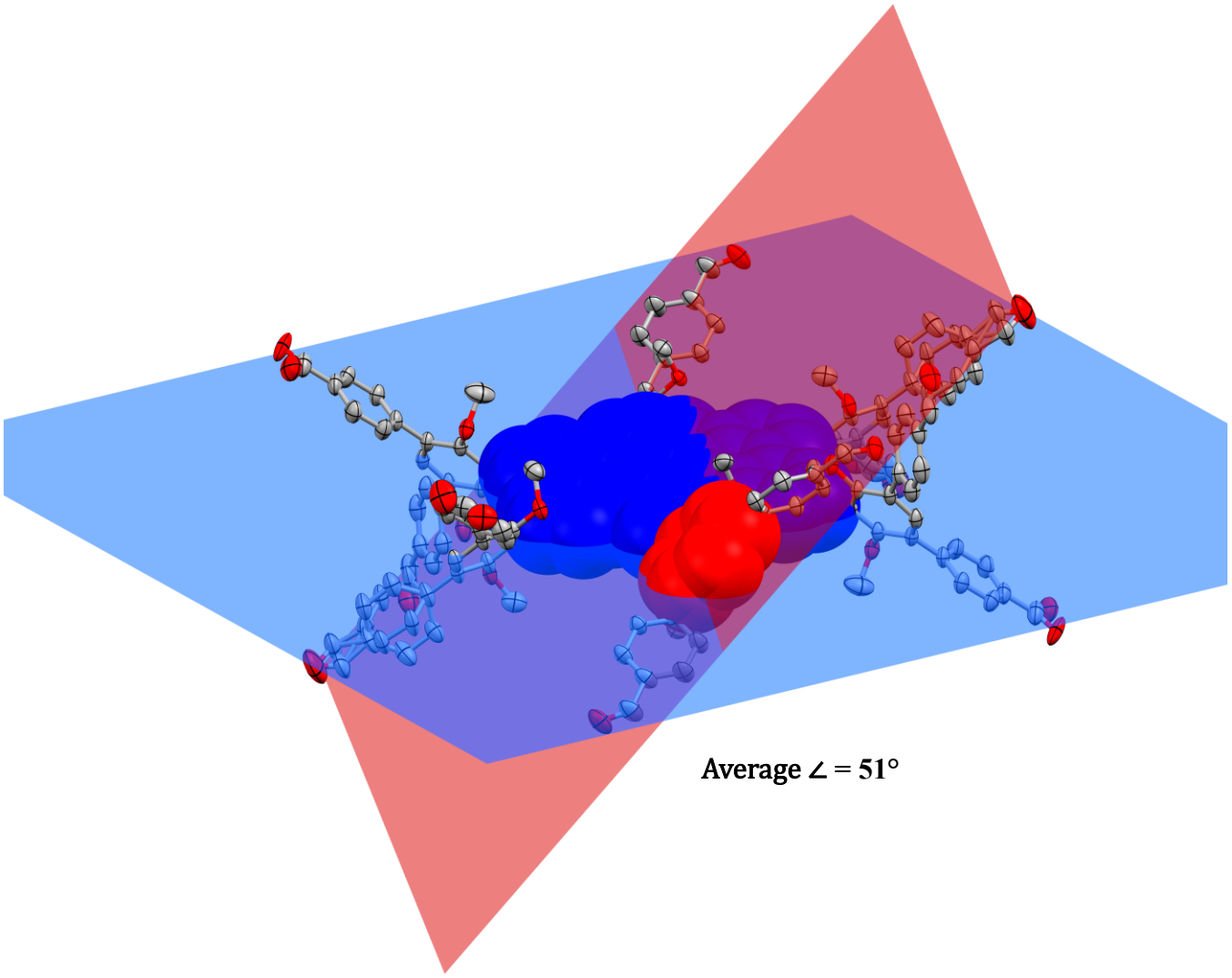

Figure S3. The image of SCXRD data collection of COF-612 using Cu Kα X-ray radiation source.

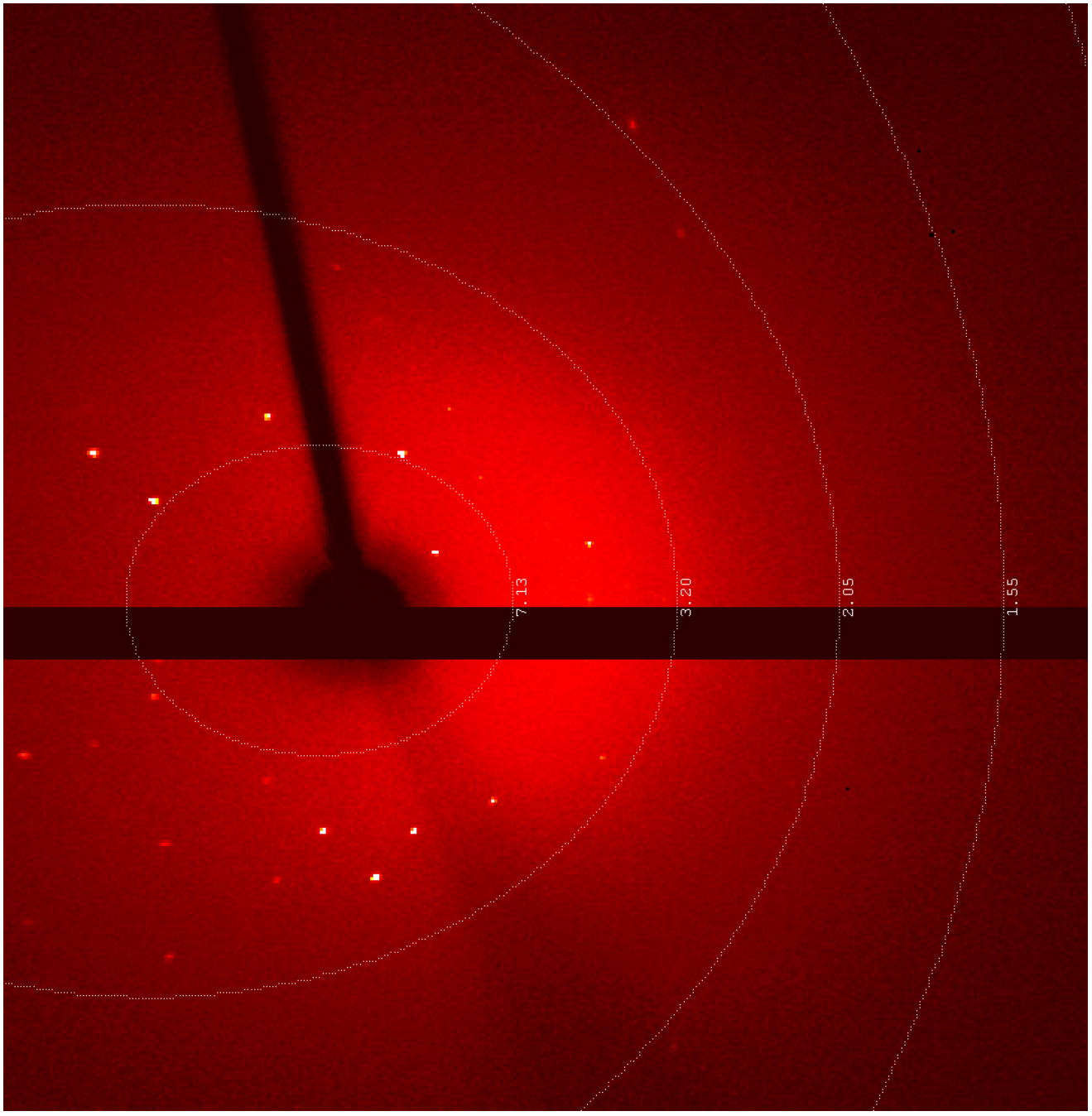

Figure S4. Top view of the simulated crystal structure of COF-612 and zoomed-in cages. Hydrogen atoms are omitted for clarity.

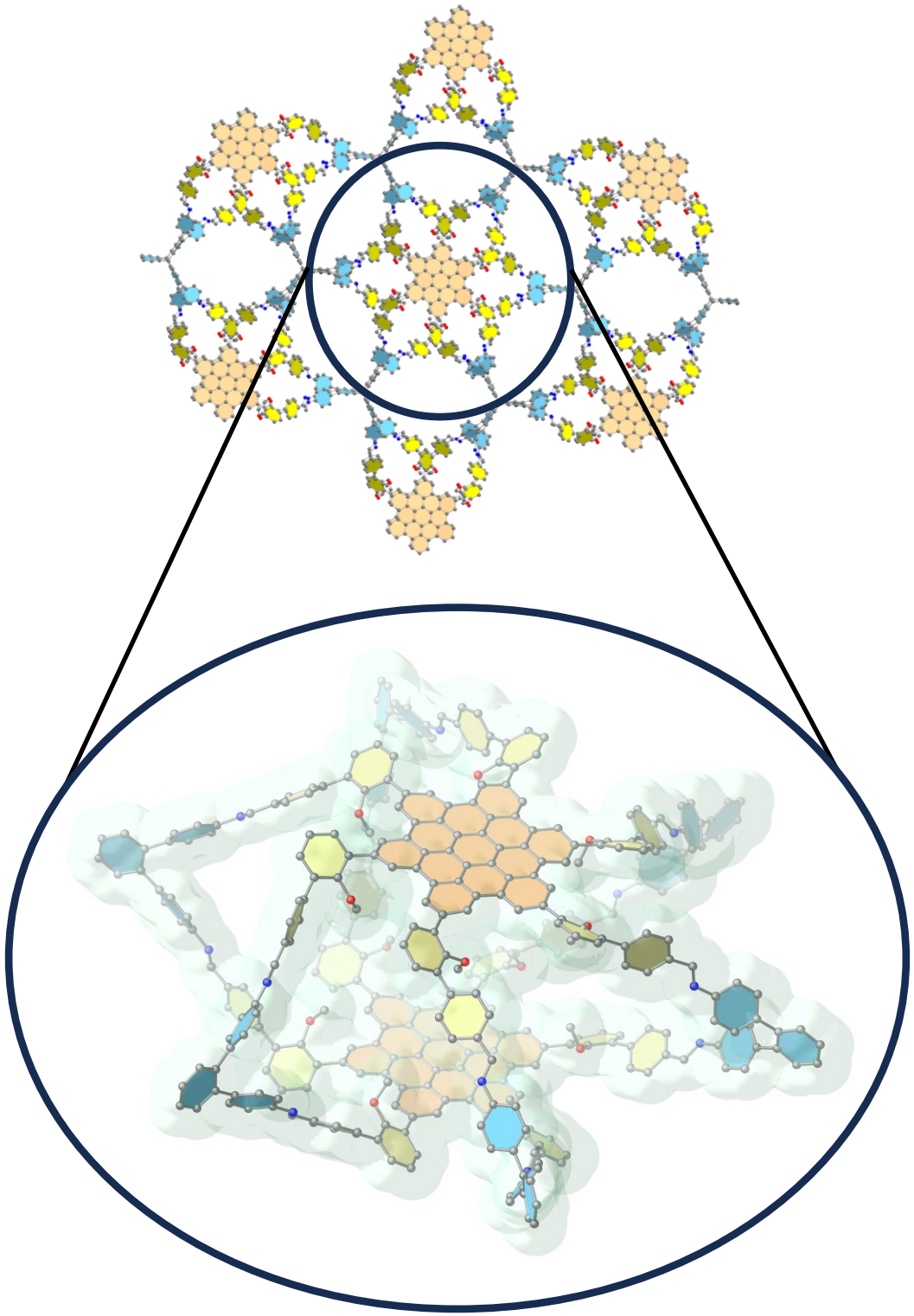

Figure S5. The least-squares-fit planes of COF-612 structure defined by the HBC core units are shown. The distance between two planes is ~15 Å, not considering the Van der Waals radius of carbon.

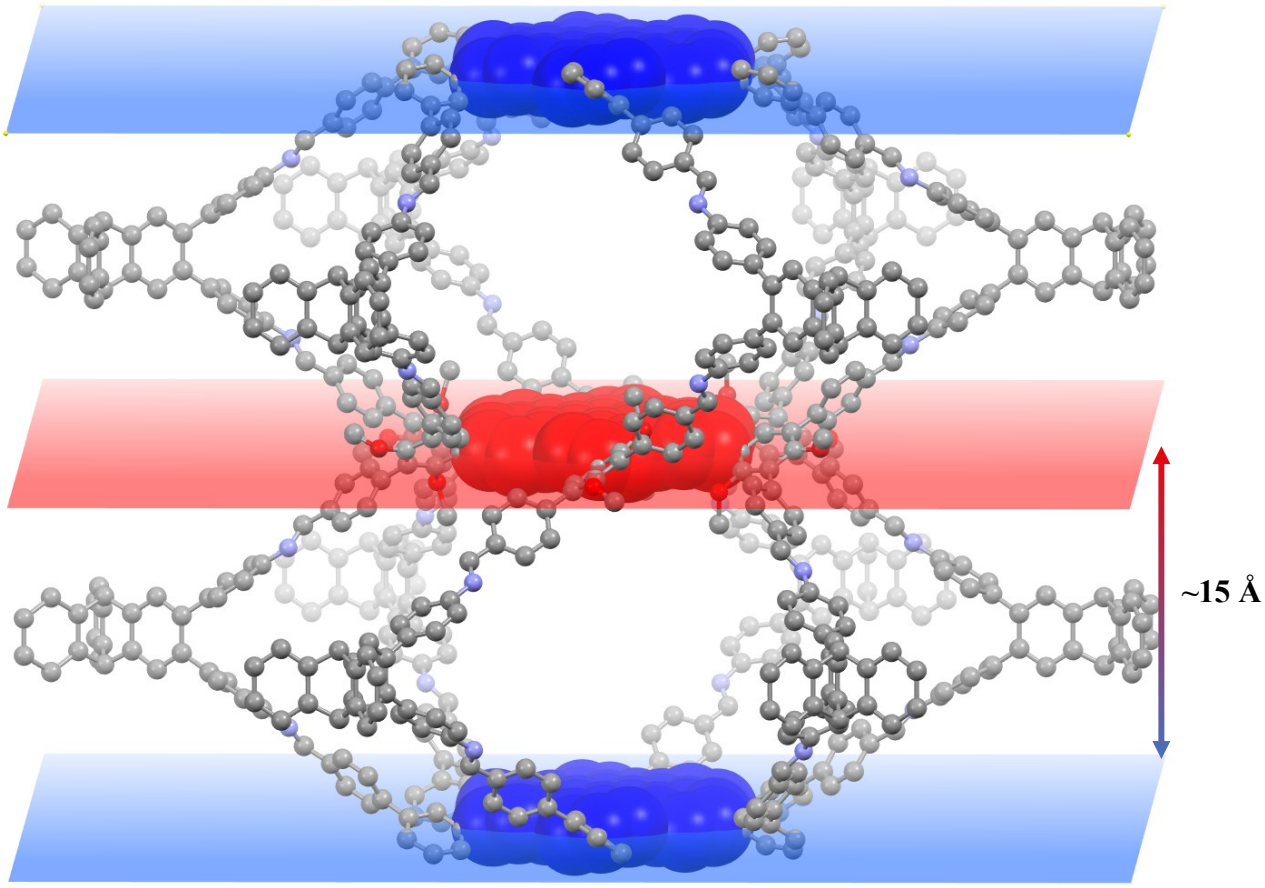

Figure S6. The least-squares-fit planes of COF-412 structure defined by the HBC core units are shown. The distance between two planes is ~22 Å, not considering the Van der Waals radius of carbon.

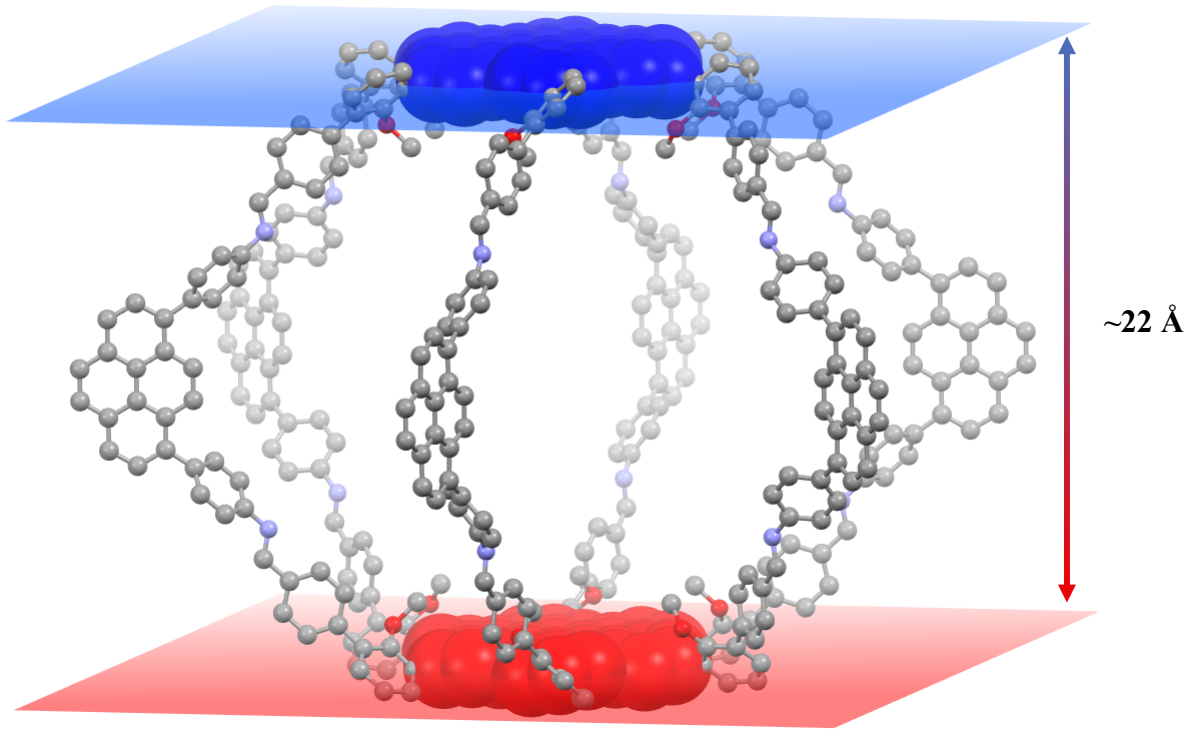

Figure S7. Microscope image of HBC-LA_{12}.

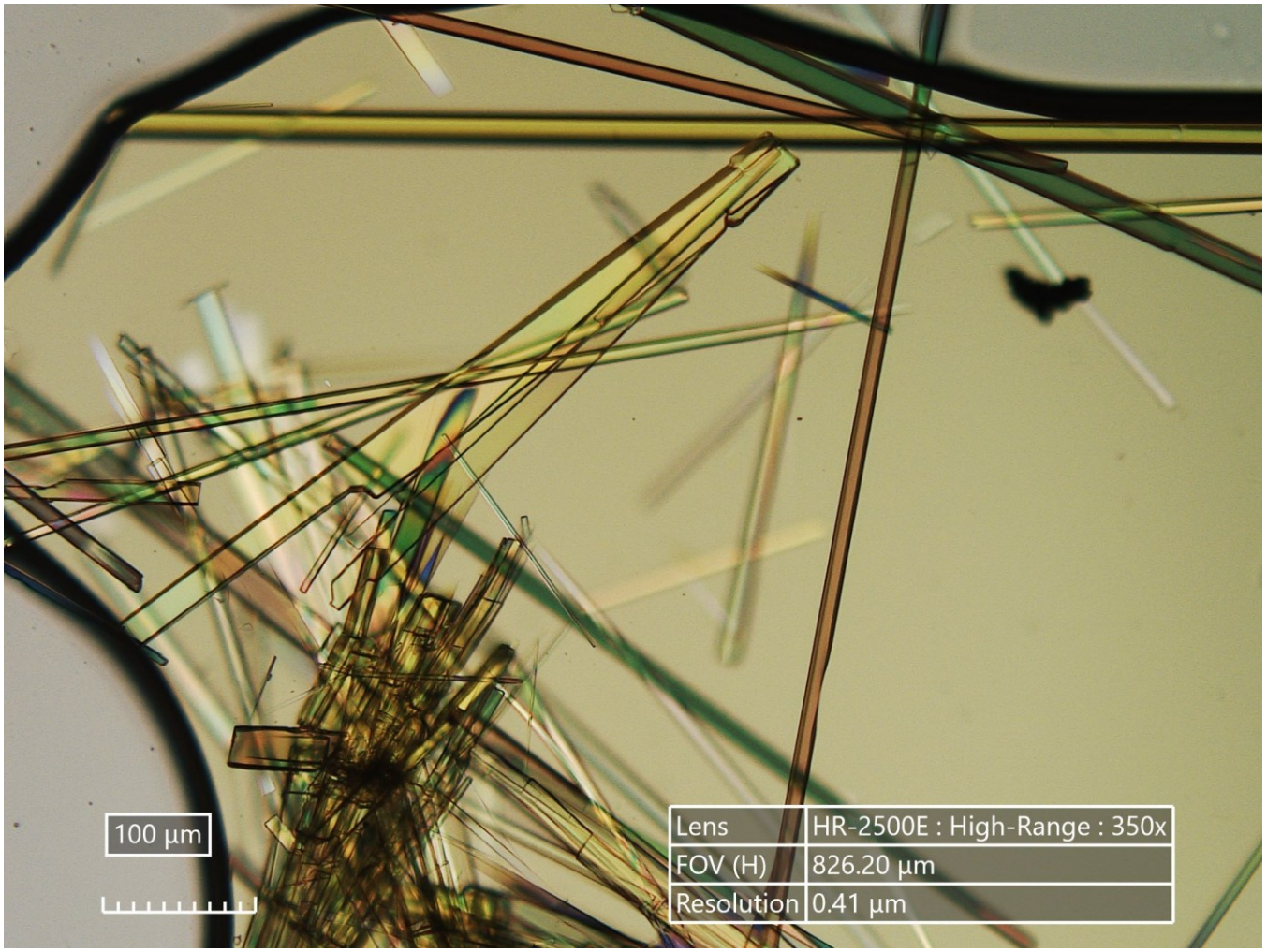

Figure S8. Microscope image of COF-612 obtained by method A.

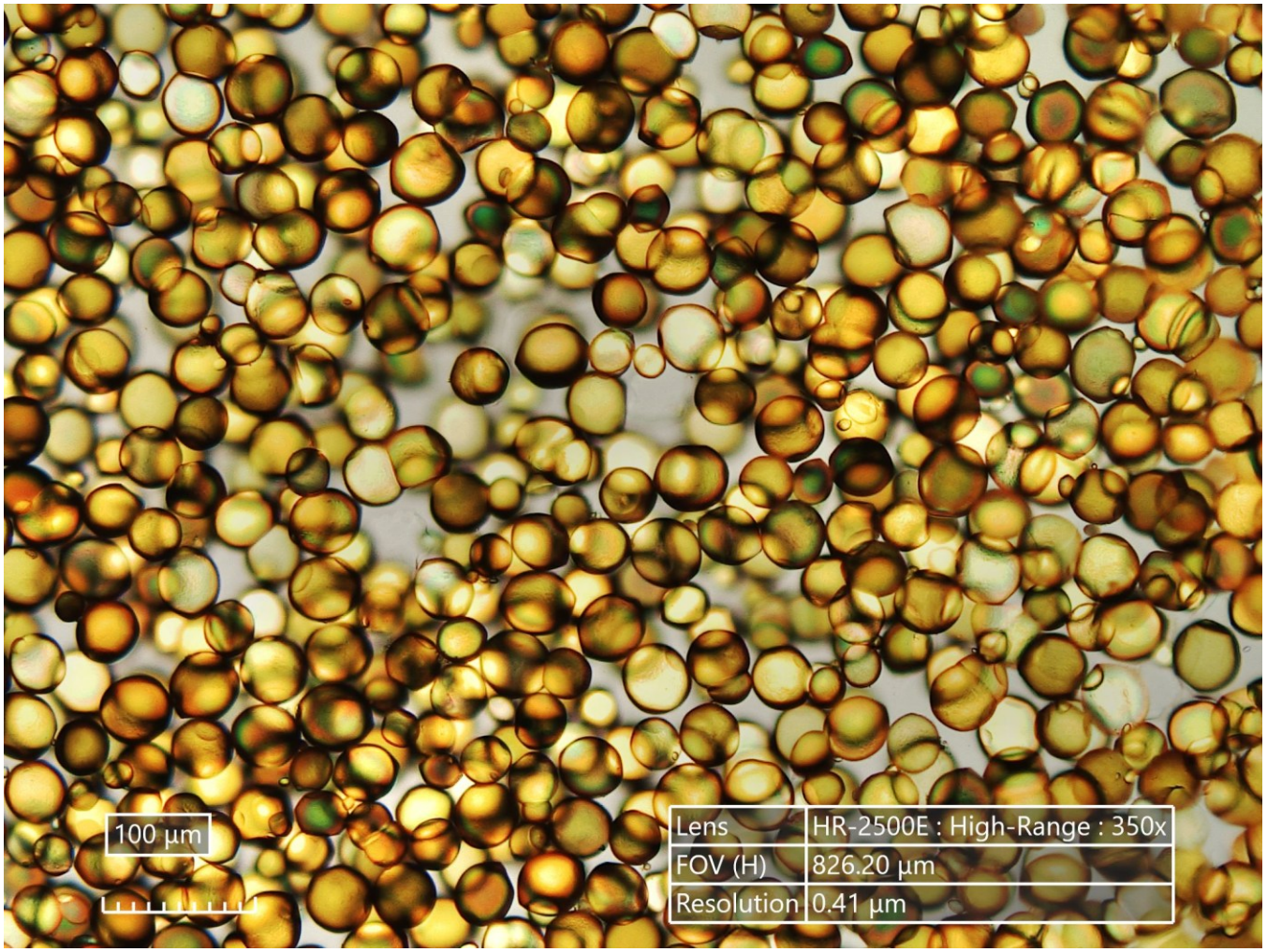

Figure S9. Microscope image of COF-612 obtained by method B.

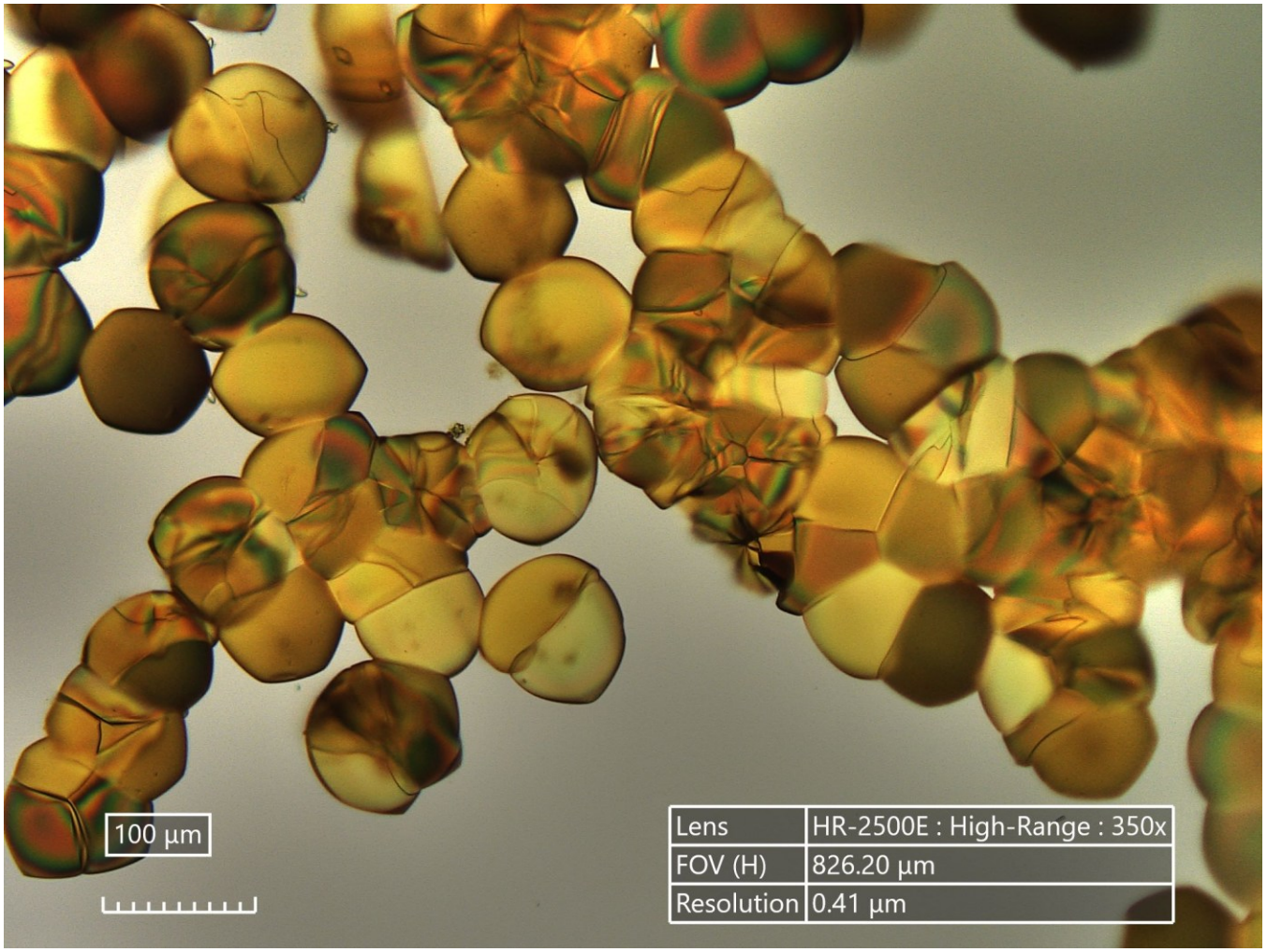

Figure S10. Microscope image of COF-412 obtained by 0.6 mL of aniline.

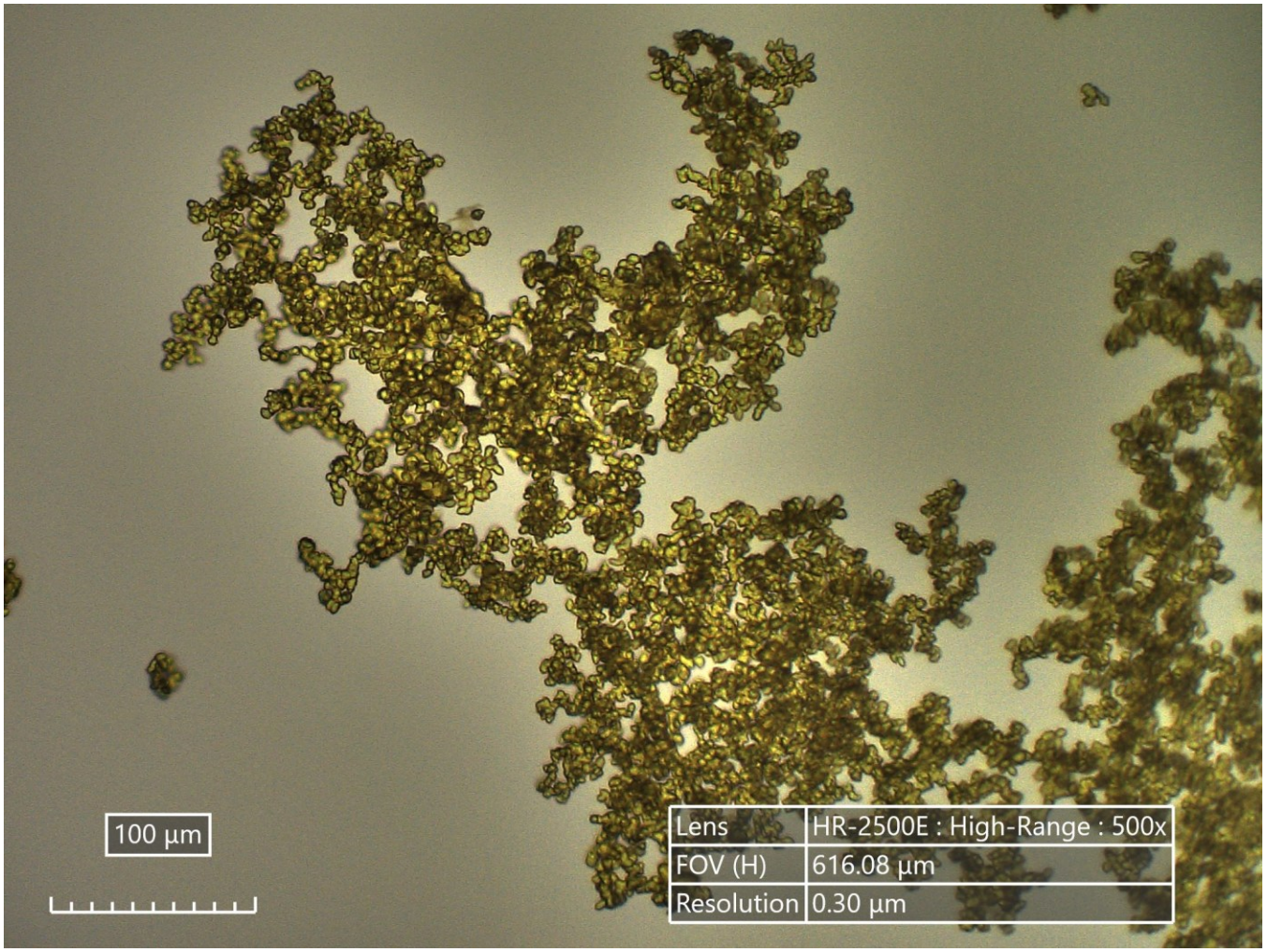

Figure S11. Microscope image of COF-412 obtained by 0.8 mL of aniline.

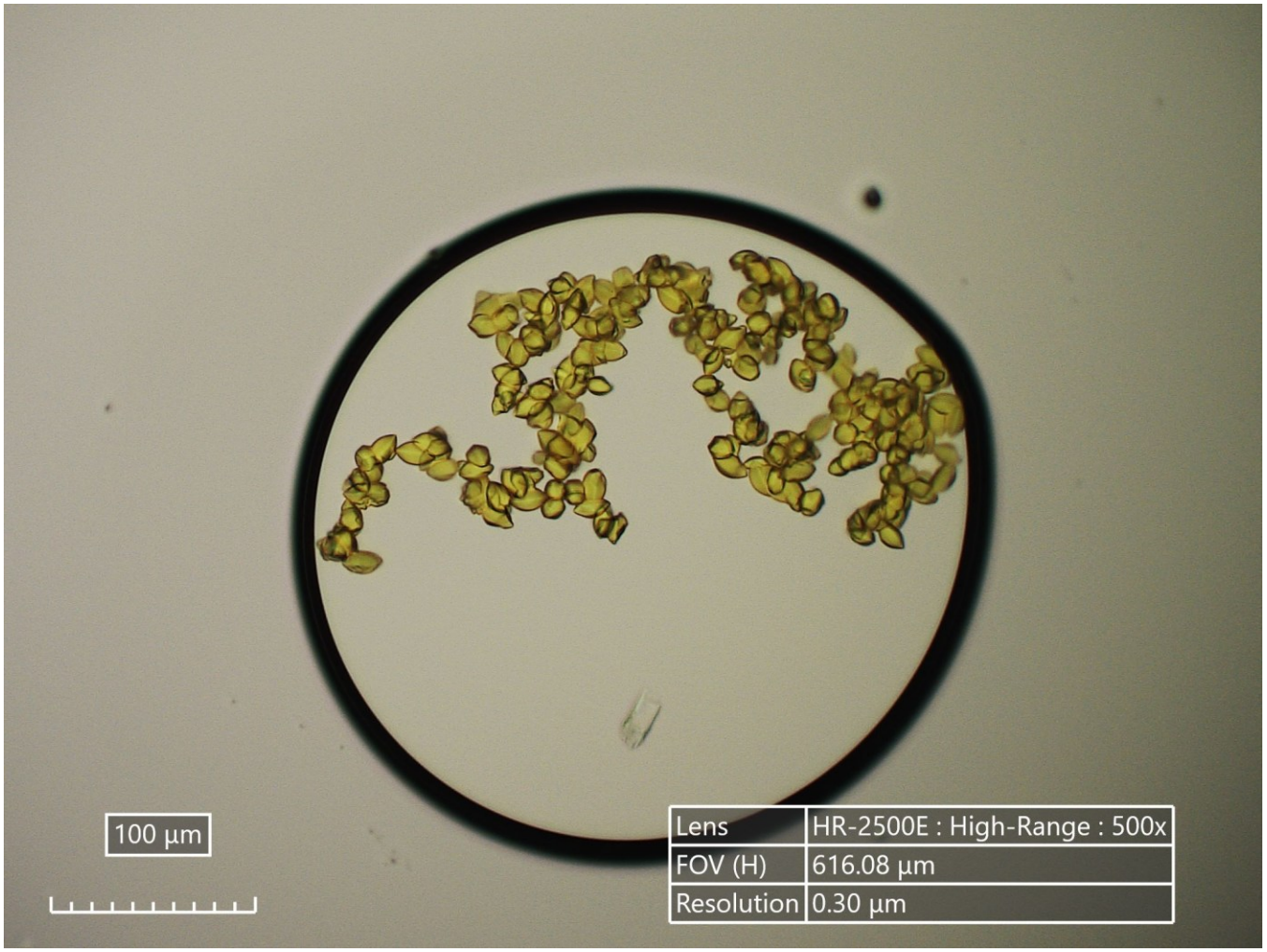

Figure S12. Side-view (top) and top-view (bottom) augmented representations of the **kez-a** topology.

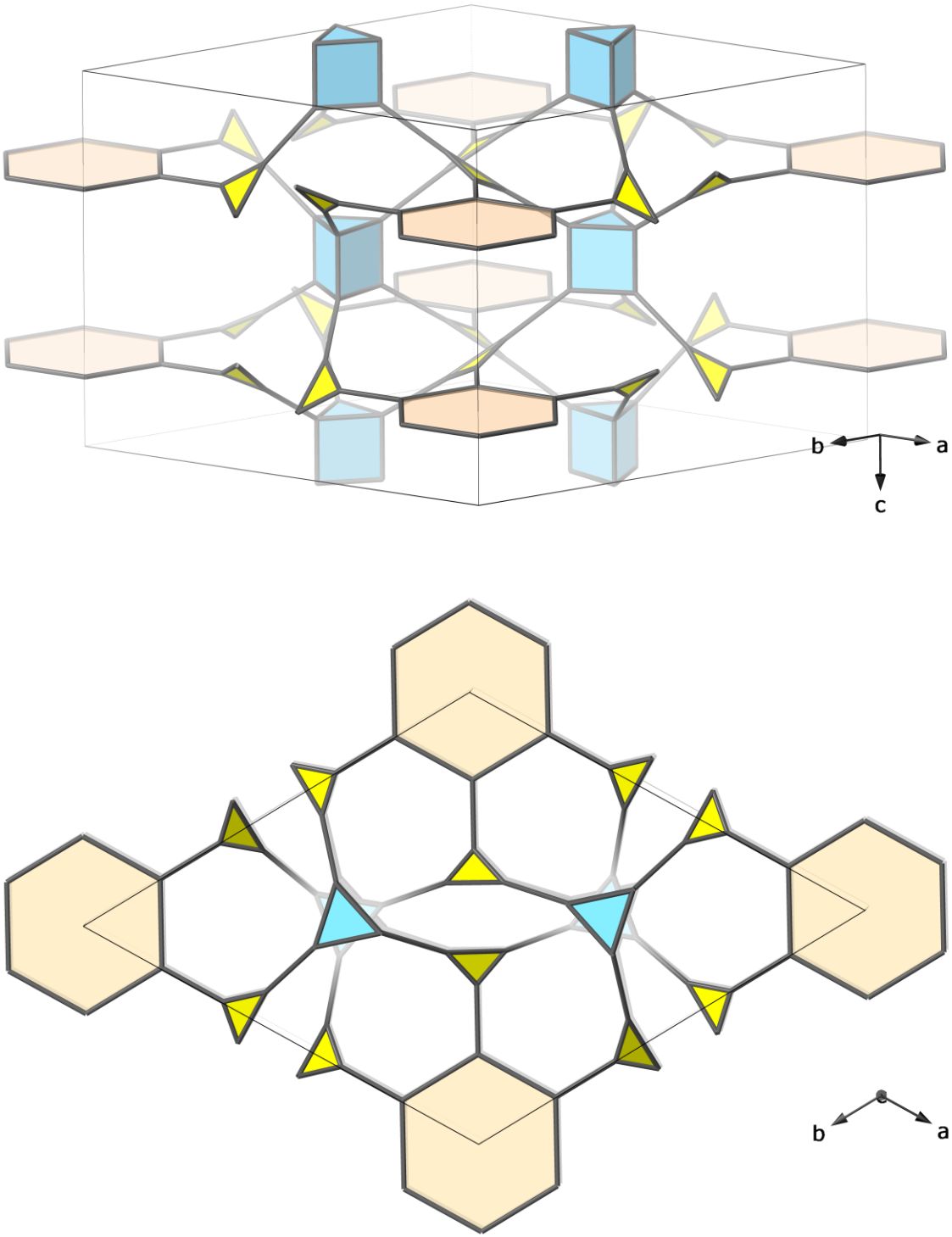

Figure S13. Side-view (top) and top-view (bottom) augmented representations of the **cez-a** topology.

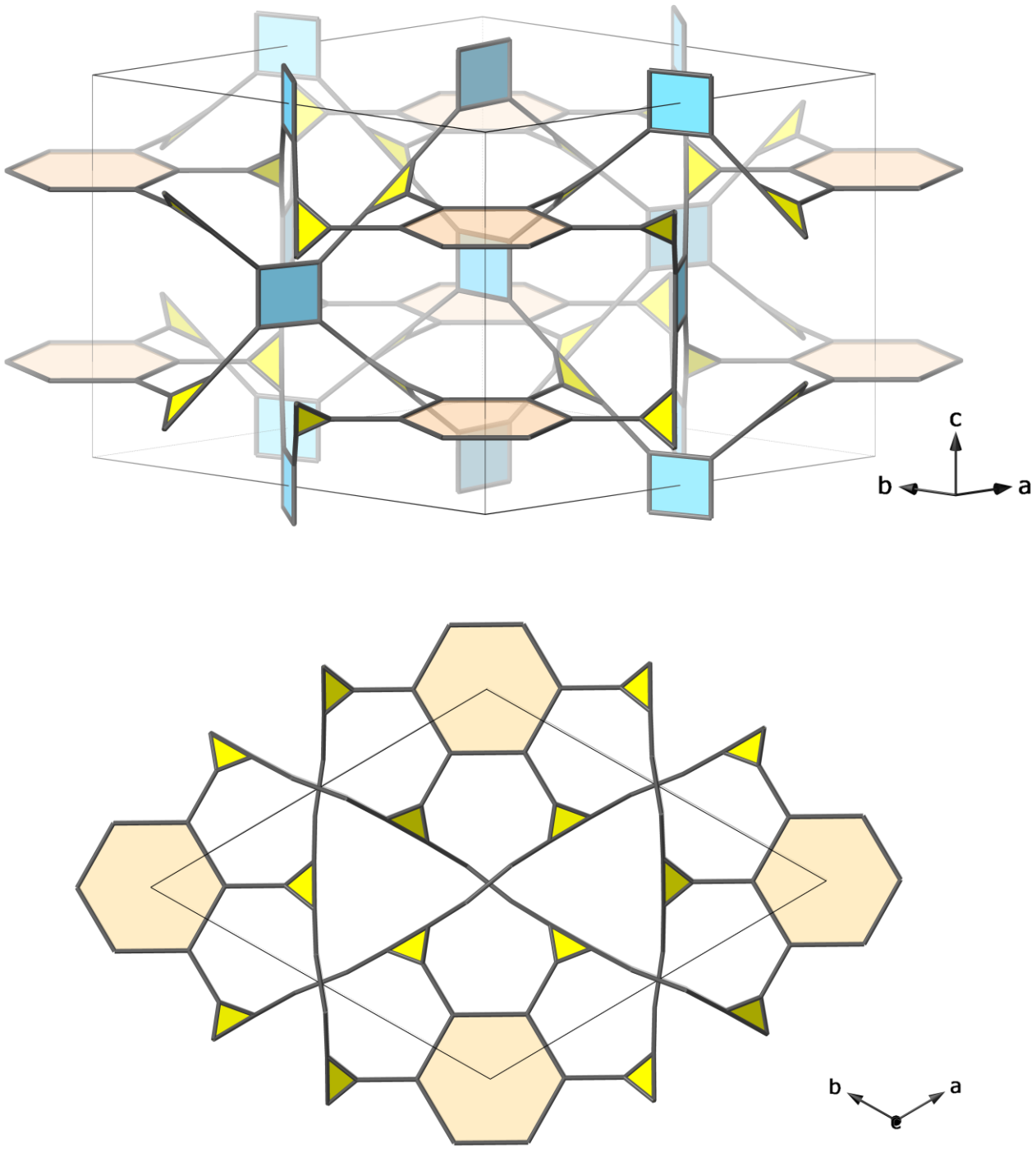

Figure S14. Side-view (top) and top-view (bottom) augmented representations of the **cee-a** topology.

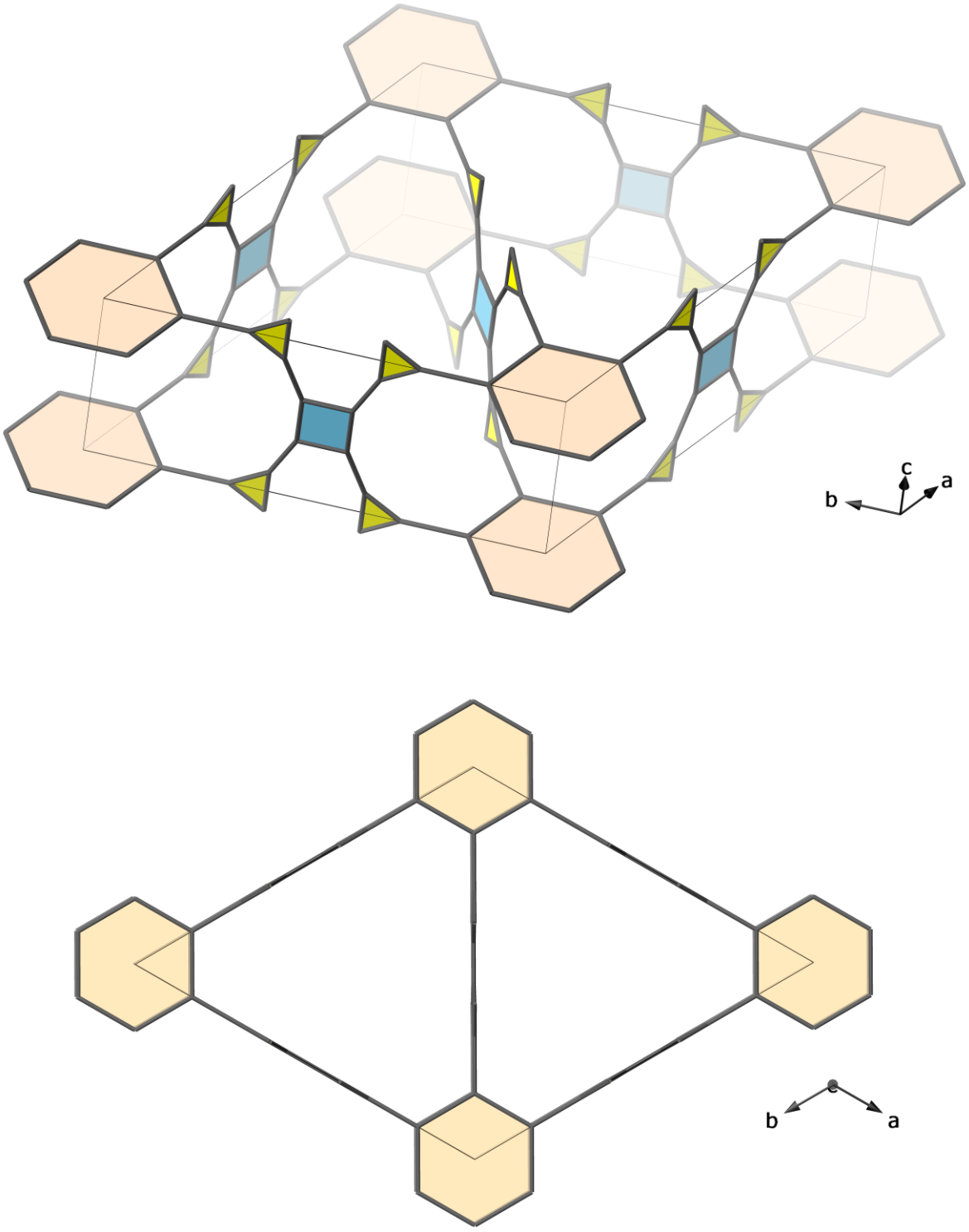

Figure S15. Overlay of the experimental pattern, Pawley refined pattern (calculated), difference pattern and Bragg positions of COF-612. The experimental PXRD pattern was collected using Bruker D8 Advance X-ray diffractometer.

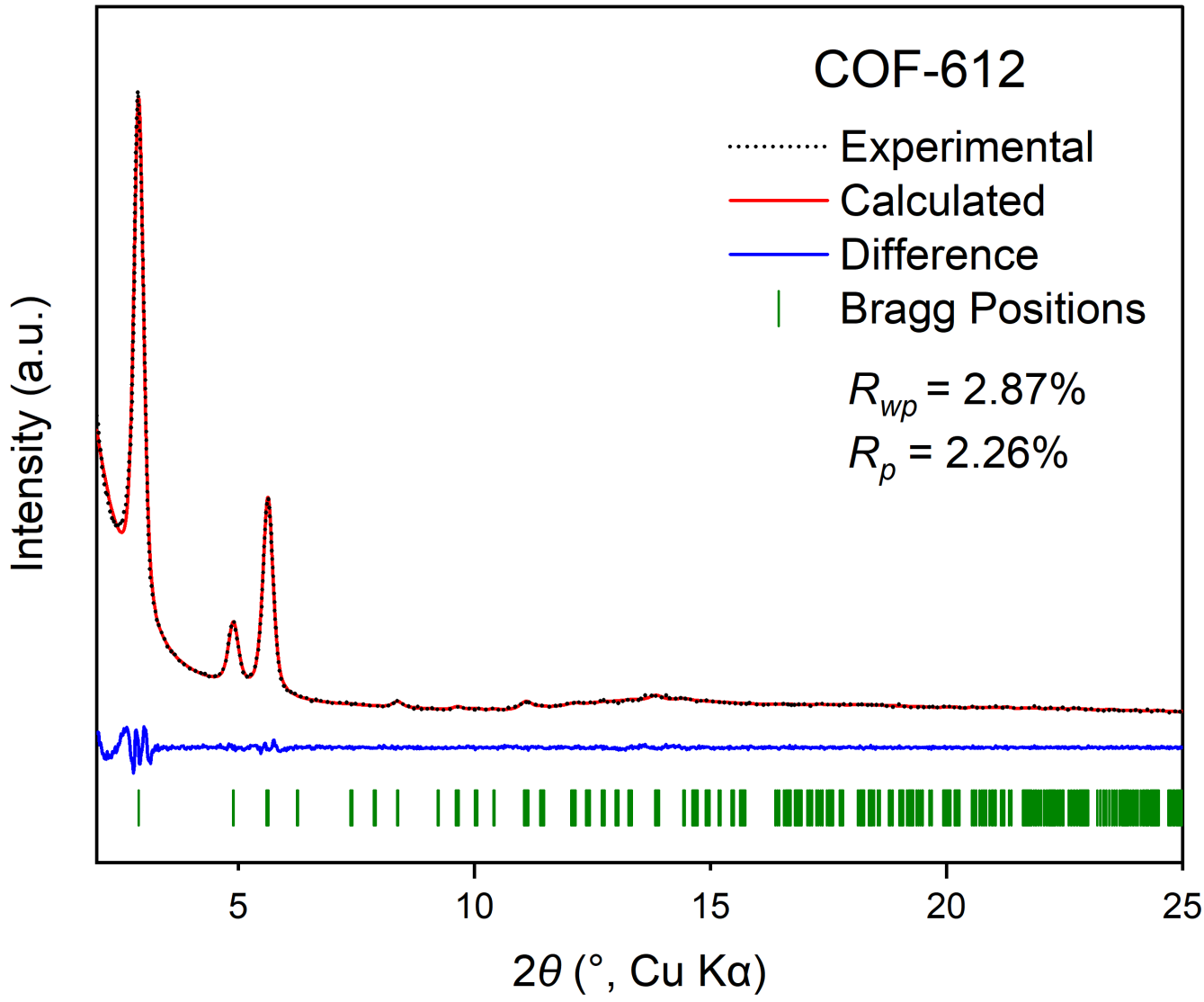

Figure S16. Overlay of the experimental pattern and simulated PXRD pattern of COF-612. The experimental PXRD pattern was collected using Bruker D8 Advance X-ray diffractometer. An initial discrepancy between calculated and experimental patterns in the relative intensities of several reflections was resolved by introducing a March–Dollase preferred orientation correction along the [001] direction, with a parameter value of 3. A zero-shift correction of 0.2° was also applied.

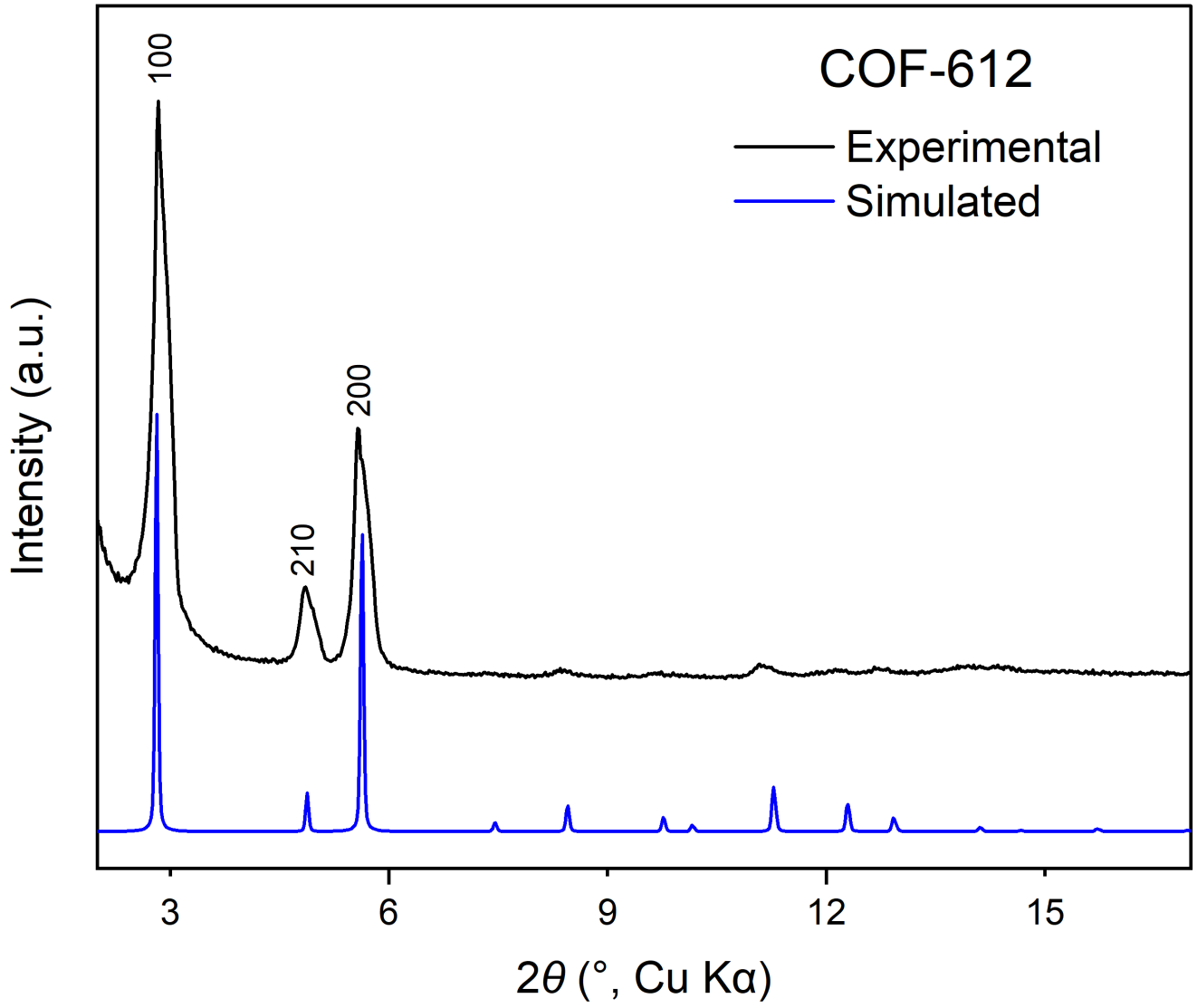

Figure S17. Overlay of the experimental pattern, Pawley refined pattern (calculated), simulated pattern, difference pattern and Bragg positions of COF-412. The experimental PXRD pattern was collected using Bruker D8 Advance X-ray diffractometer.

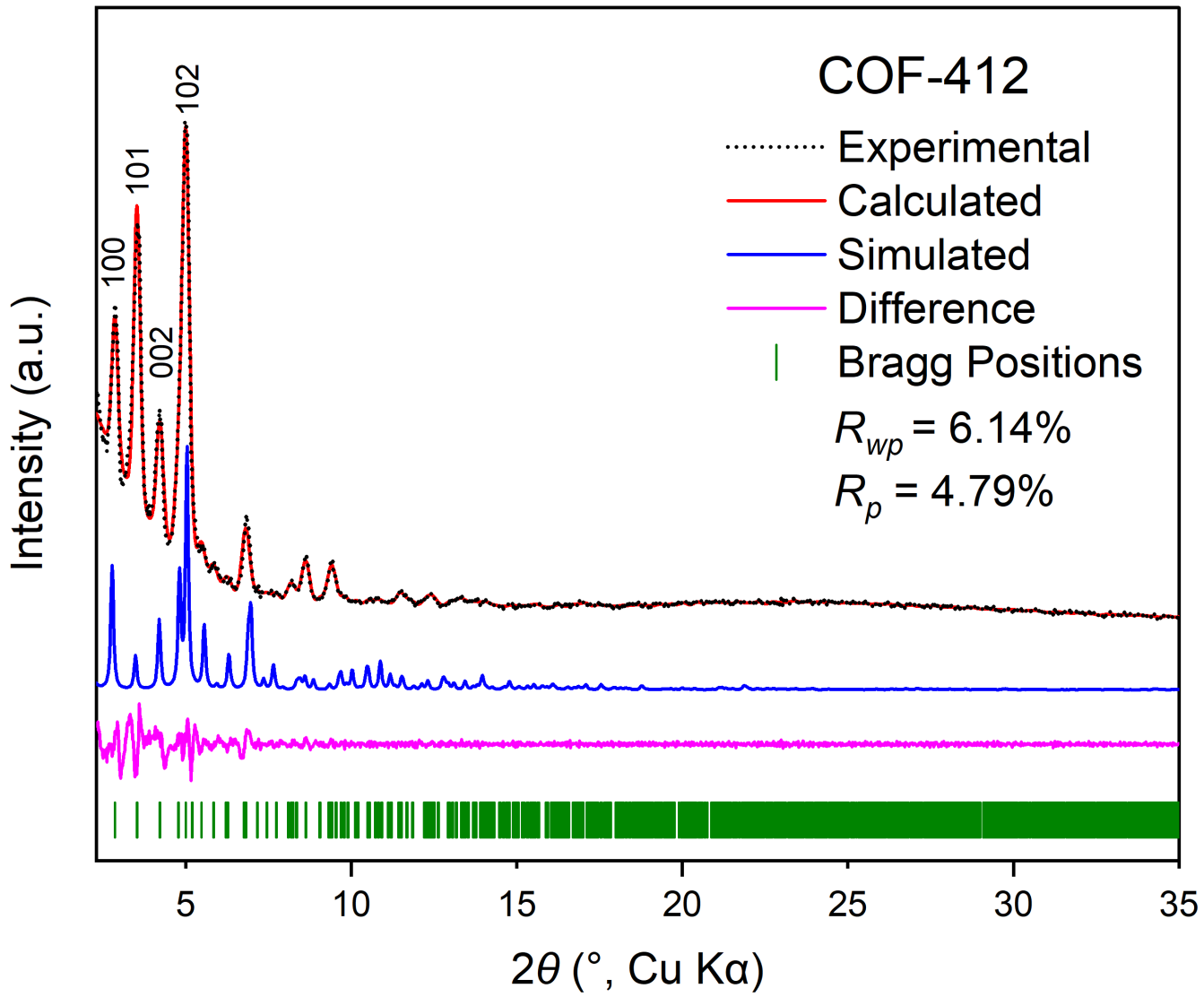

Figure S18. Overlay of the experimental pattern, Pawley refined pattern (calculated), simulated pattern, difference pattern and Bragg positions of COF-412. The experimental PXRD pattern was collected using synchrotron source.

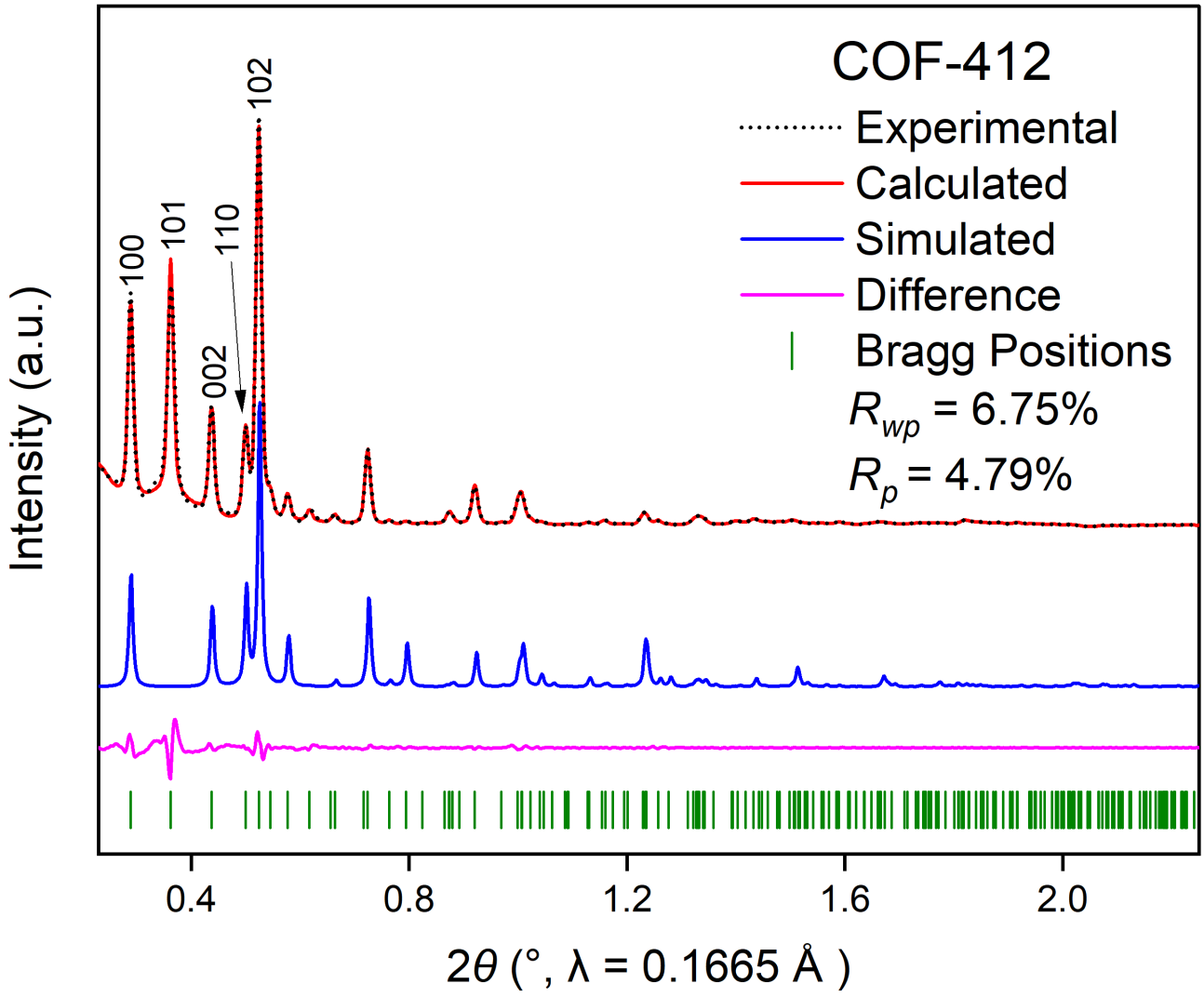

Figure S19. Overlay of the experimental pattern and simulated PXRD pattern of **cez** (vertical), **cez** (horizontal) and **cee** topologies of COF-412. The experimental PXRD pattern was collected using Bruker D8 Advance X-ray diffractometer. The horizontal and vertical directions denote the orientation of the pyrene moiety with respect to the crystallographic a-axis.

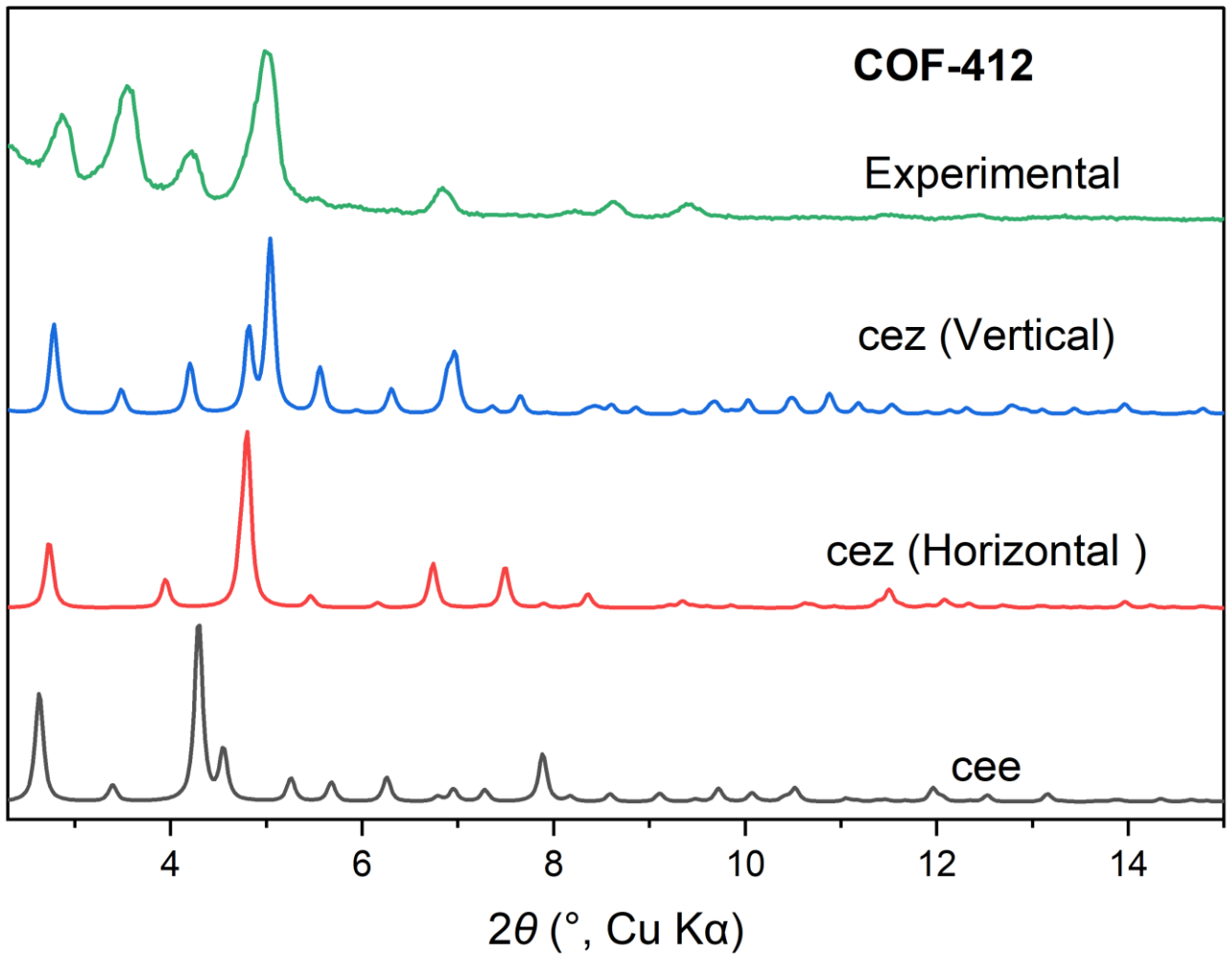

Figure S20. Overlay of the experimental PXRD patterns of COF-412 collected using a Bruker D8 Advance X-ray diffractometer and a synchrotron source.

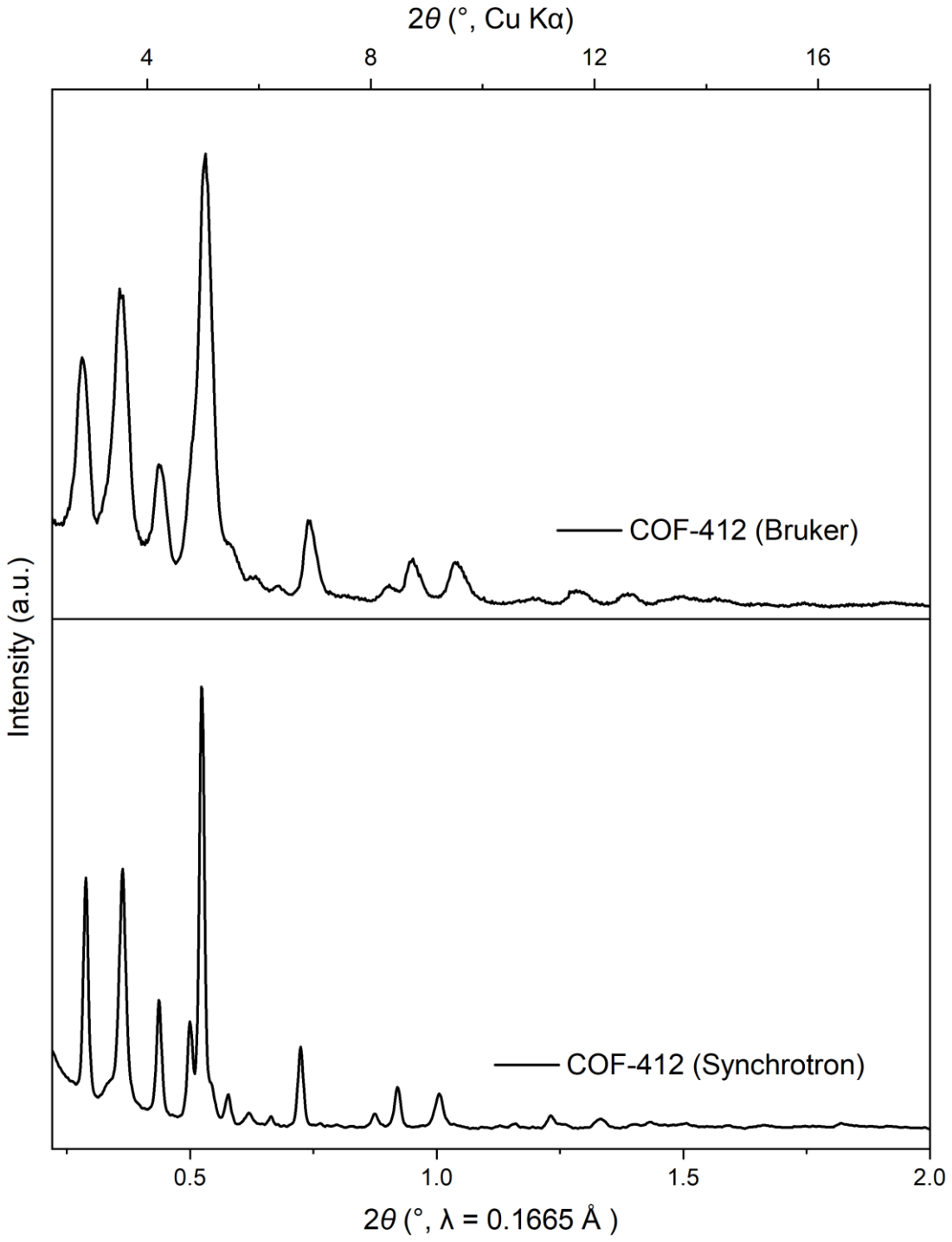

Figure S21. Overlay of the normalized experimental PXRD patterns of COF-612 after immersion in different solvents (10 mL) for 24 h, collected using a Bruker D8 Advance X-ray diffractometer. The as-synthesized crystals were immersed in the indicated solvents for 24 h, followed by solvent exchange with methanol (15 mL × 3) and subsequent supercritical CO2 (scCO2) drying.

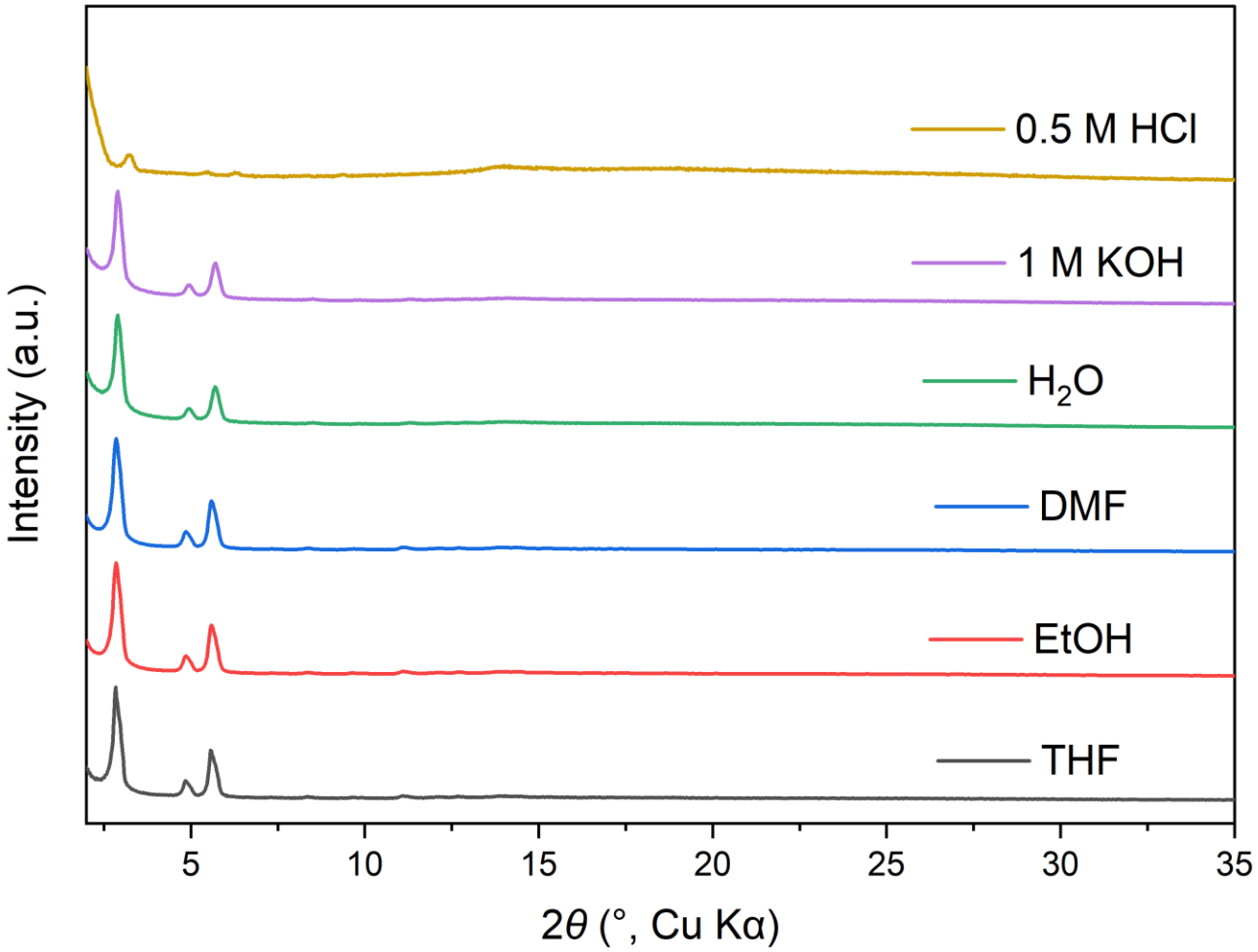

Figure S22. Overlay of the normalized experimental PXRD patterns of COF-412 after immersion in different solvents (10 mL) for 24 h, collected using a Bruker D8 Advance X-ray diffractometer. The as-synthesized crystals were immersed in the indicated solvents for 24 h, followed by solvent exchange with methanol (15 mL × 3) and subsequent supercritical CO2 (scCO2) drying.

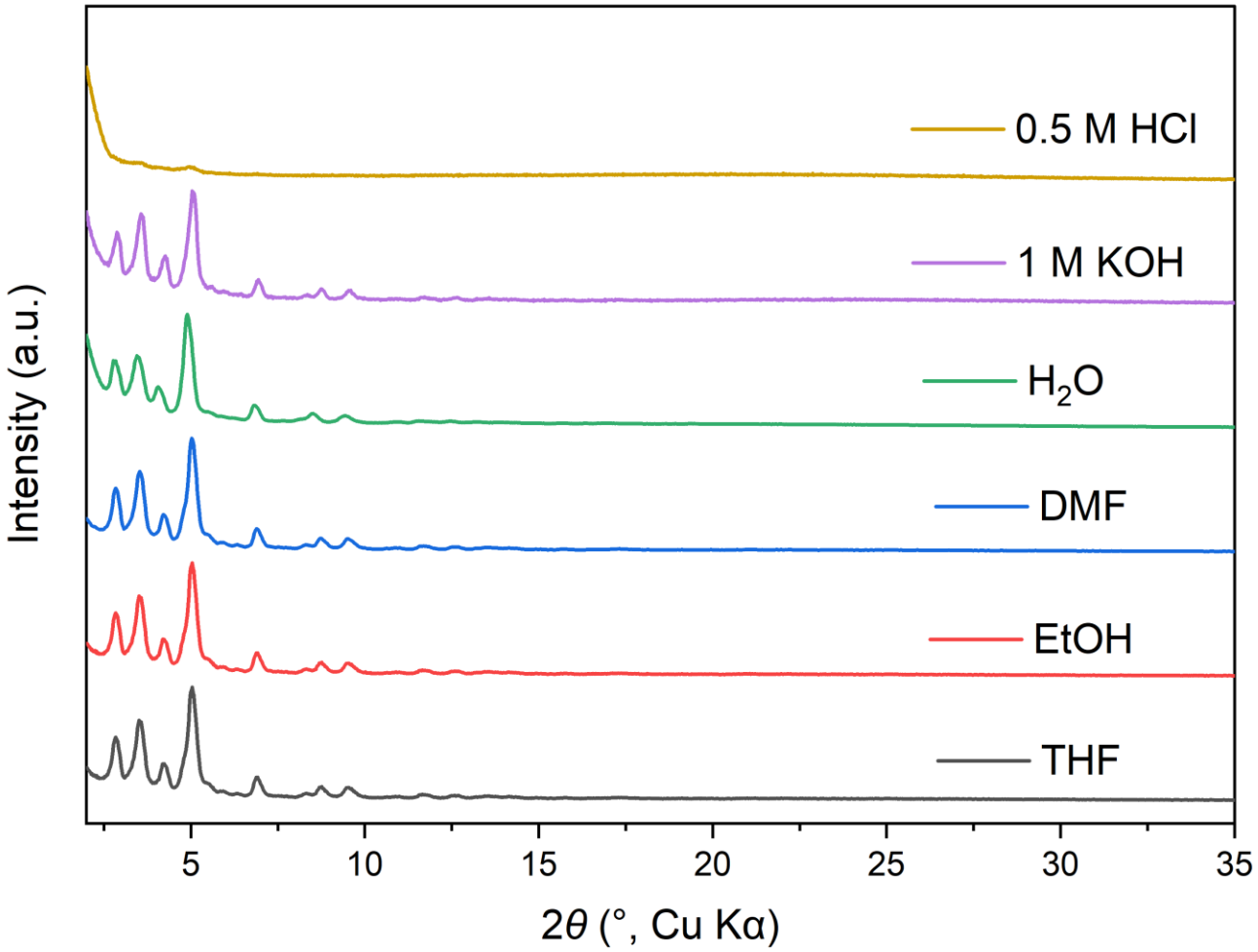

S4. Gas Sorption and TGA.

Figure S23. Ar and N_2 sorption isotherms of COF-612 and COF-412 measured at 87 and 77 K, respectively.

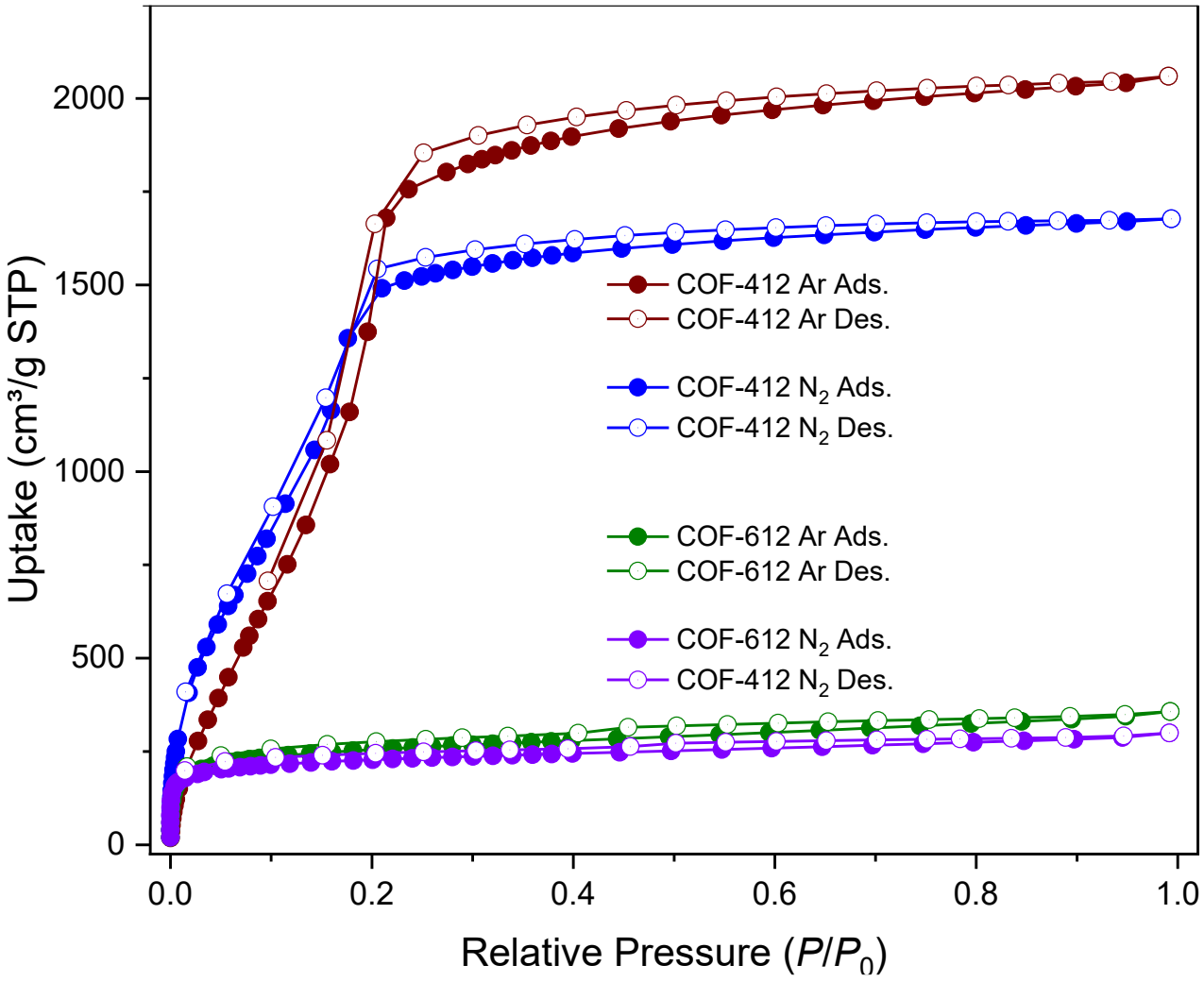

Figure S24. Ar adsorption isotherm of COF-612 measured at 87 K.

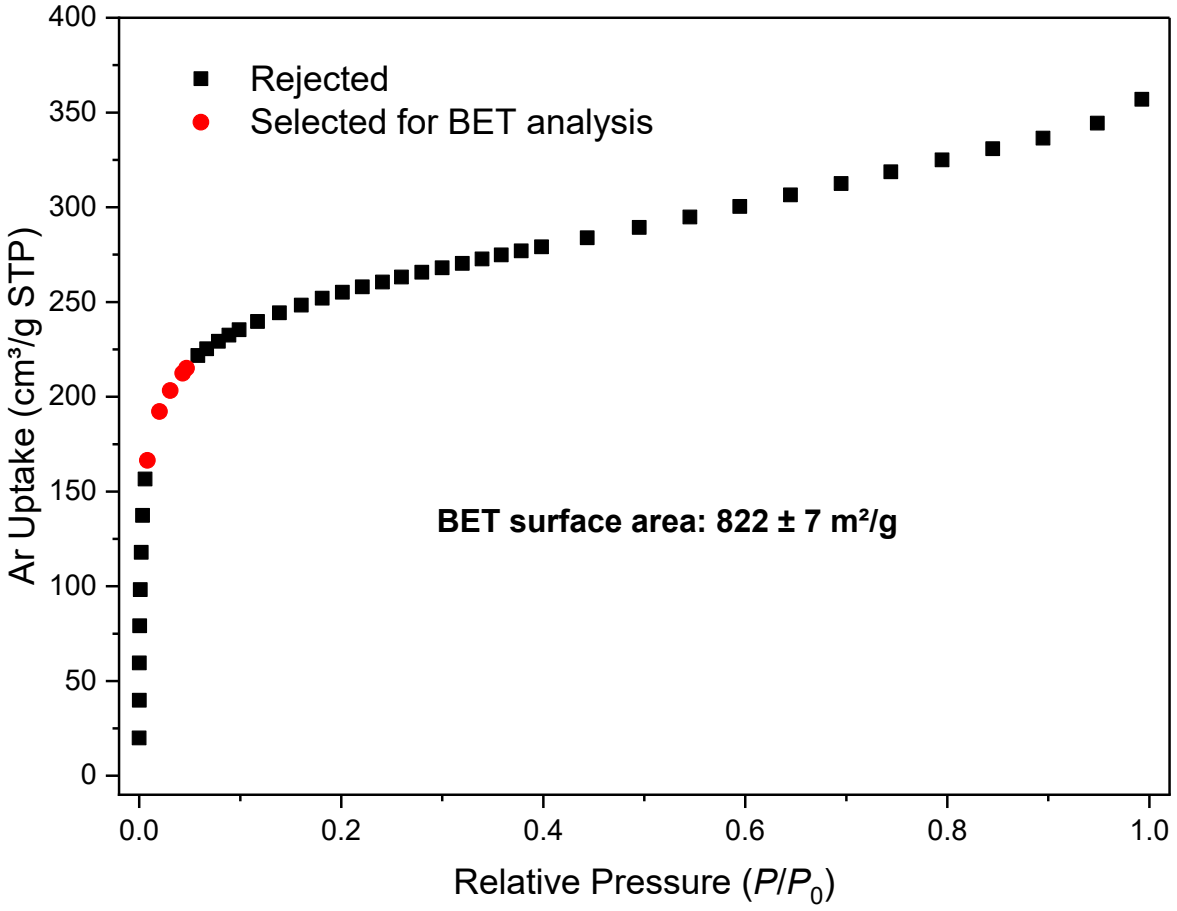

Figure S25. Rouquerol plot to determine appropriate points for BET analysis using the Ar sorption isotherm of COF-612 measured at 87 K.

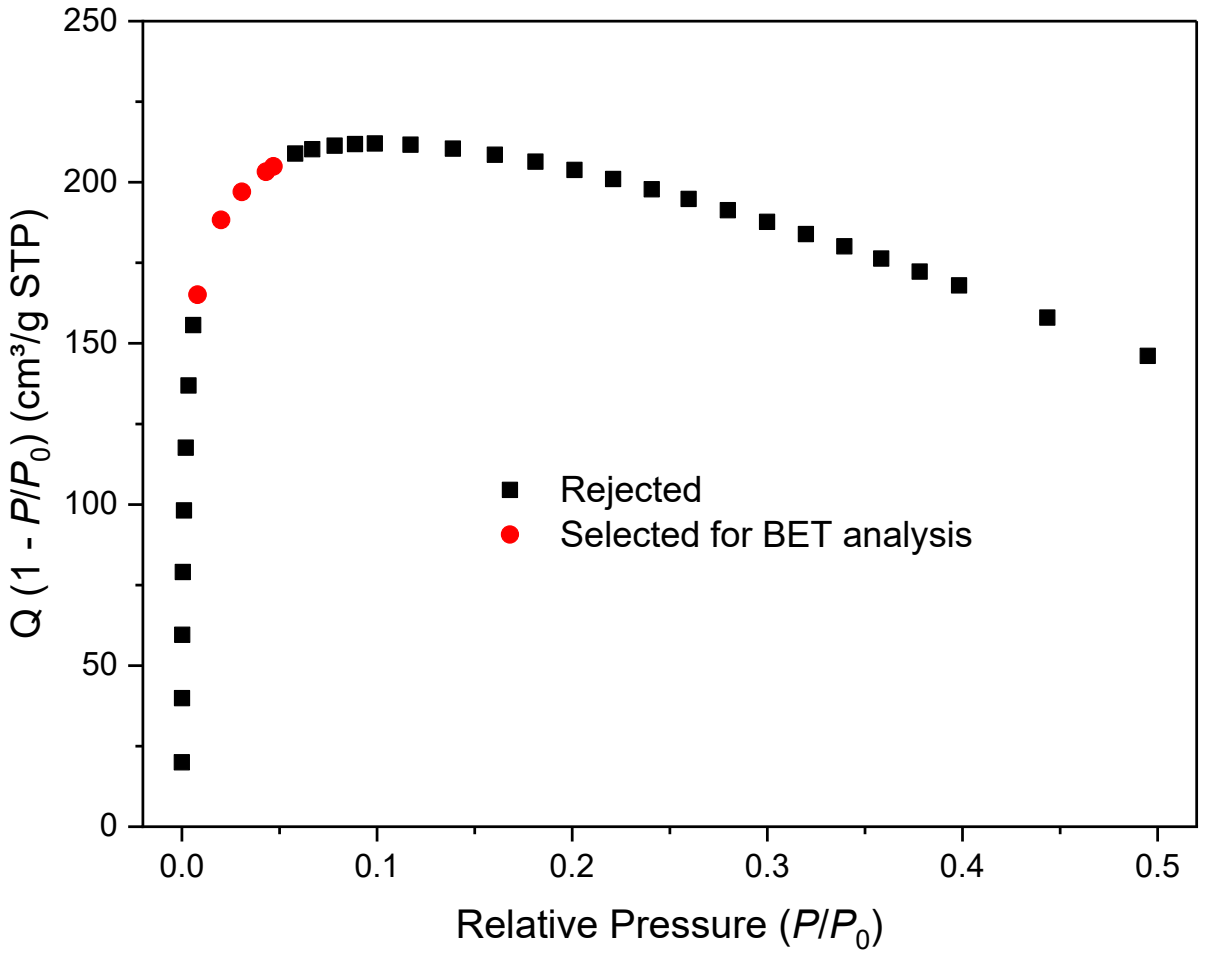

Figure S26. BET plot of COF-612 using the Ar sorption isotherm measured at 87 K.

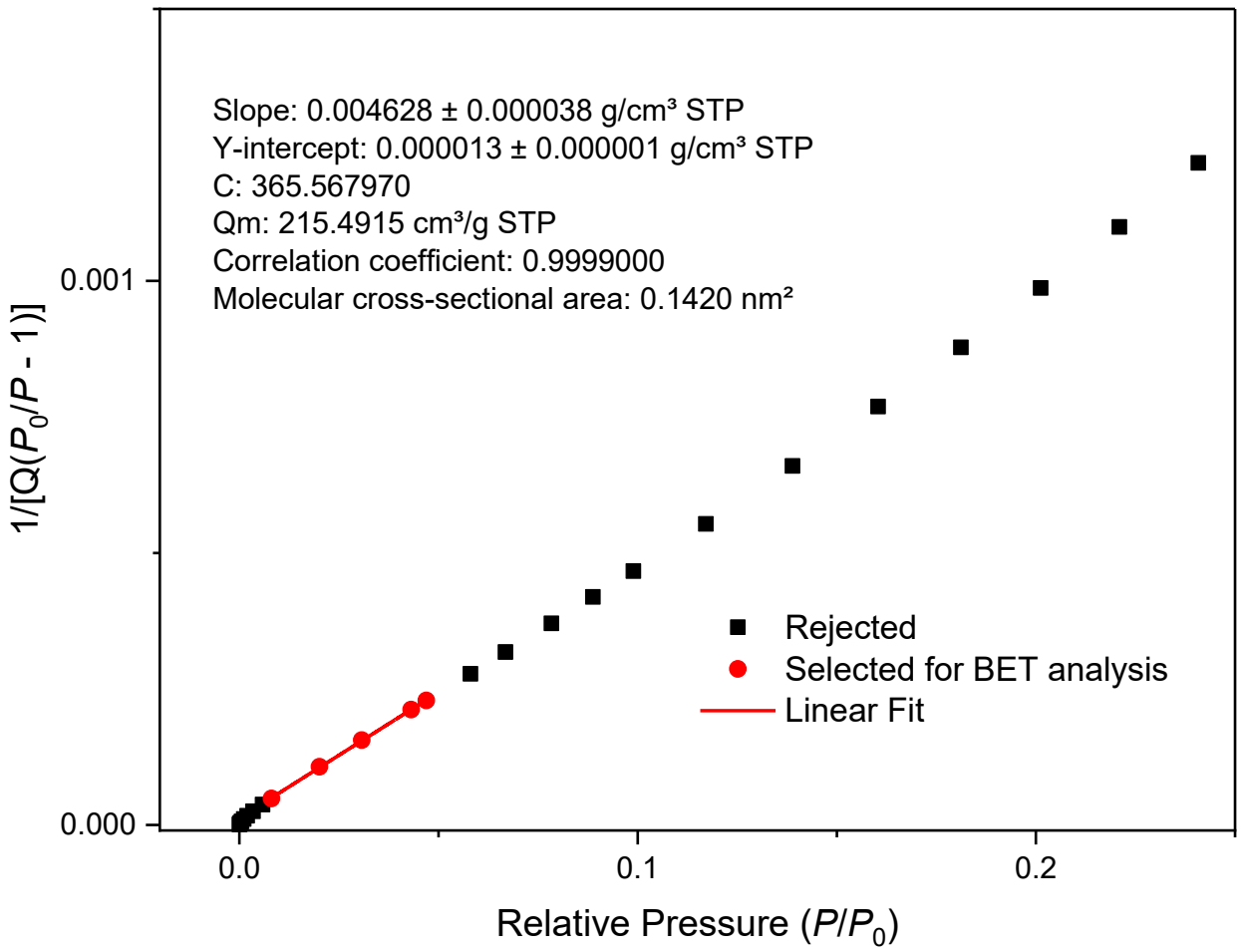

Figure S27. N_2 adsorption isotherm of COF-612 measured at 77 K.

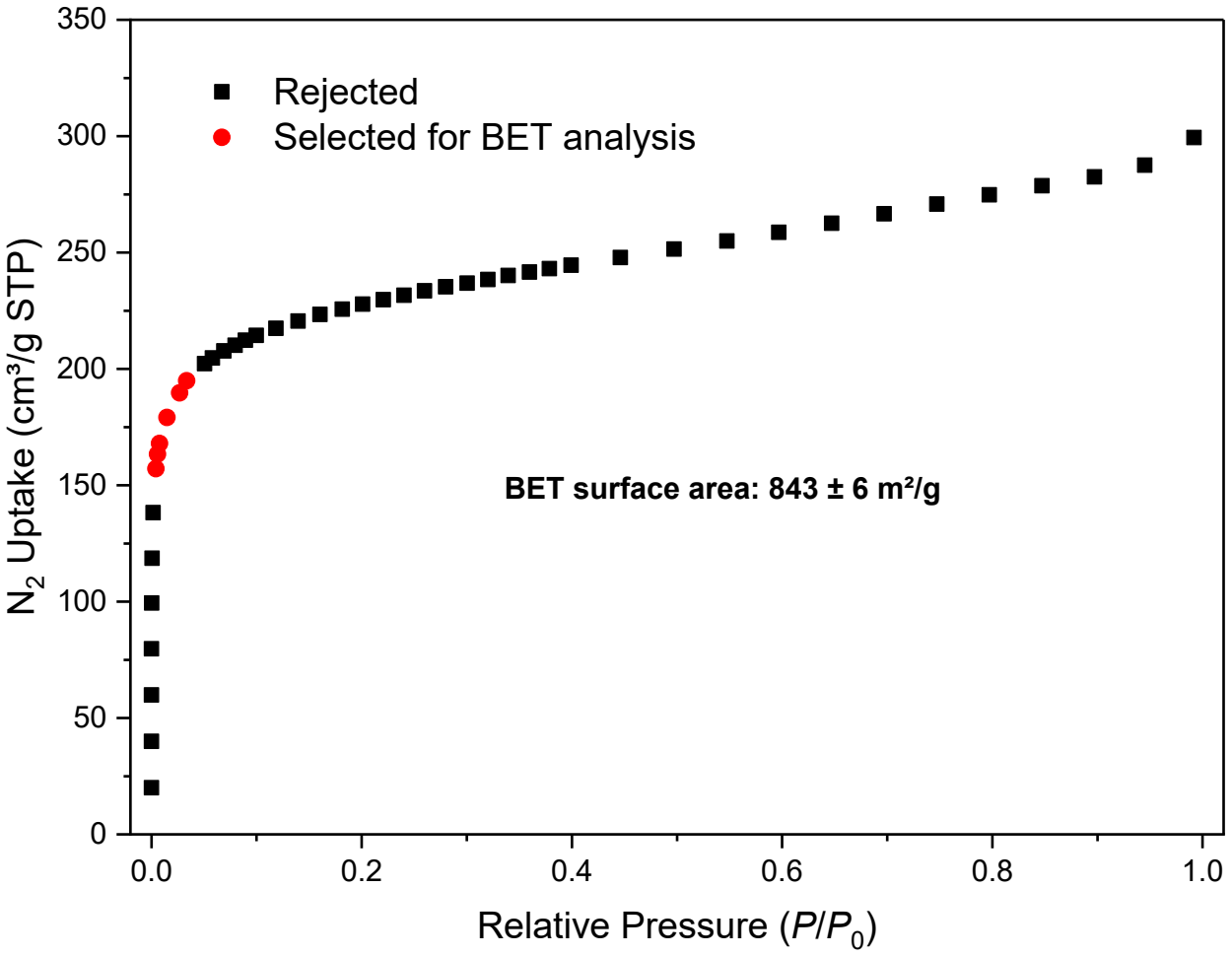

Figure S28. Rouquerol plot to determine appropriate points for BET analysis using the N_2 sorption isotherm of COF-612 measured at 77 K.

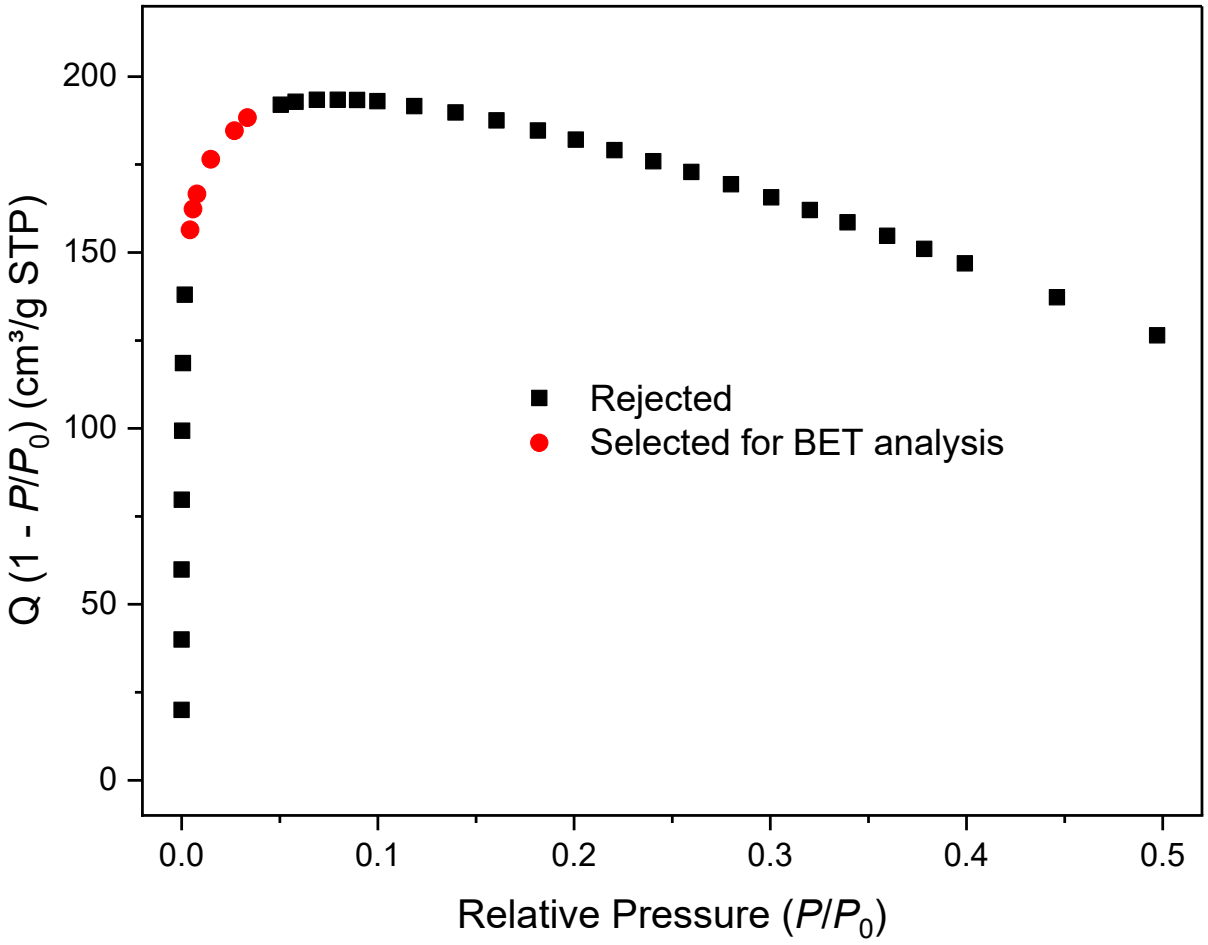

Figure S29. BET plot of COF-612 using the N_2 sorption isotherm measured at 77 K.

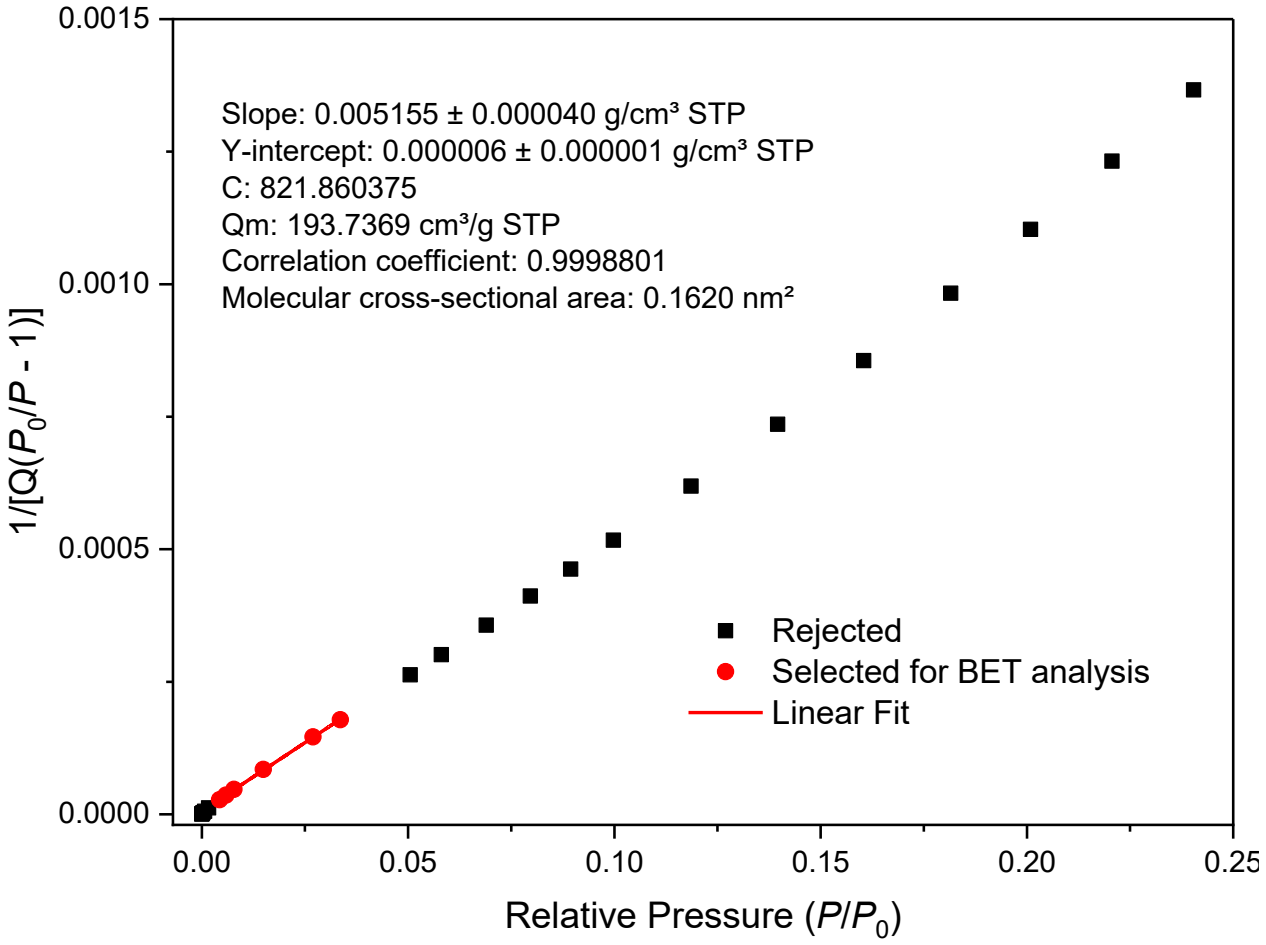

Figure S30. BET Surface area of COF-612 analyzed by BETSI[10] from the Ar adsorption isotherms collected at 87 K.

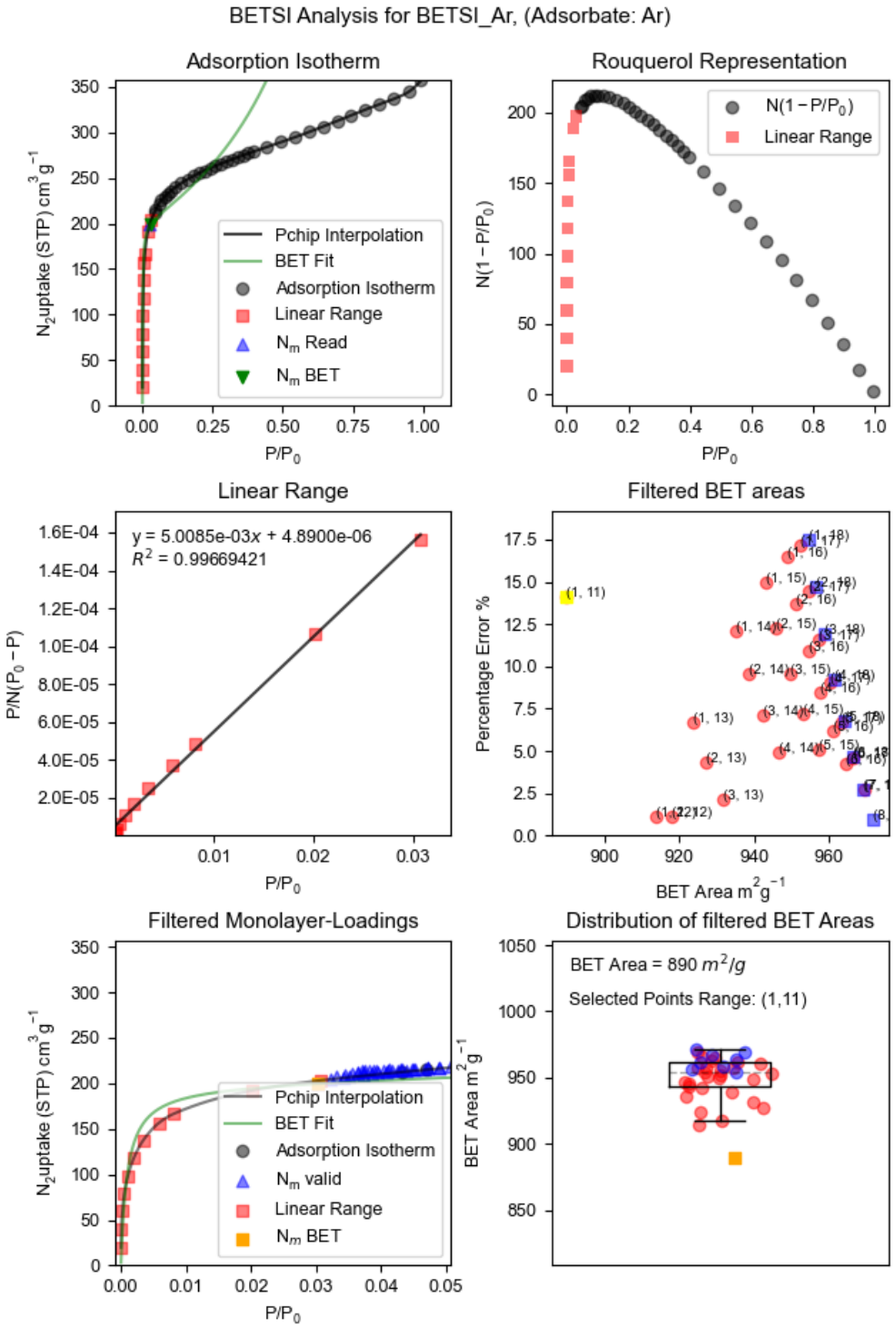

Figure S31. BET Surface area of COF-612 analyzed by BETSI[10] from the N_2 adsorption isotherms collected at 77 K.

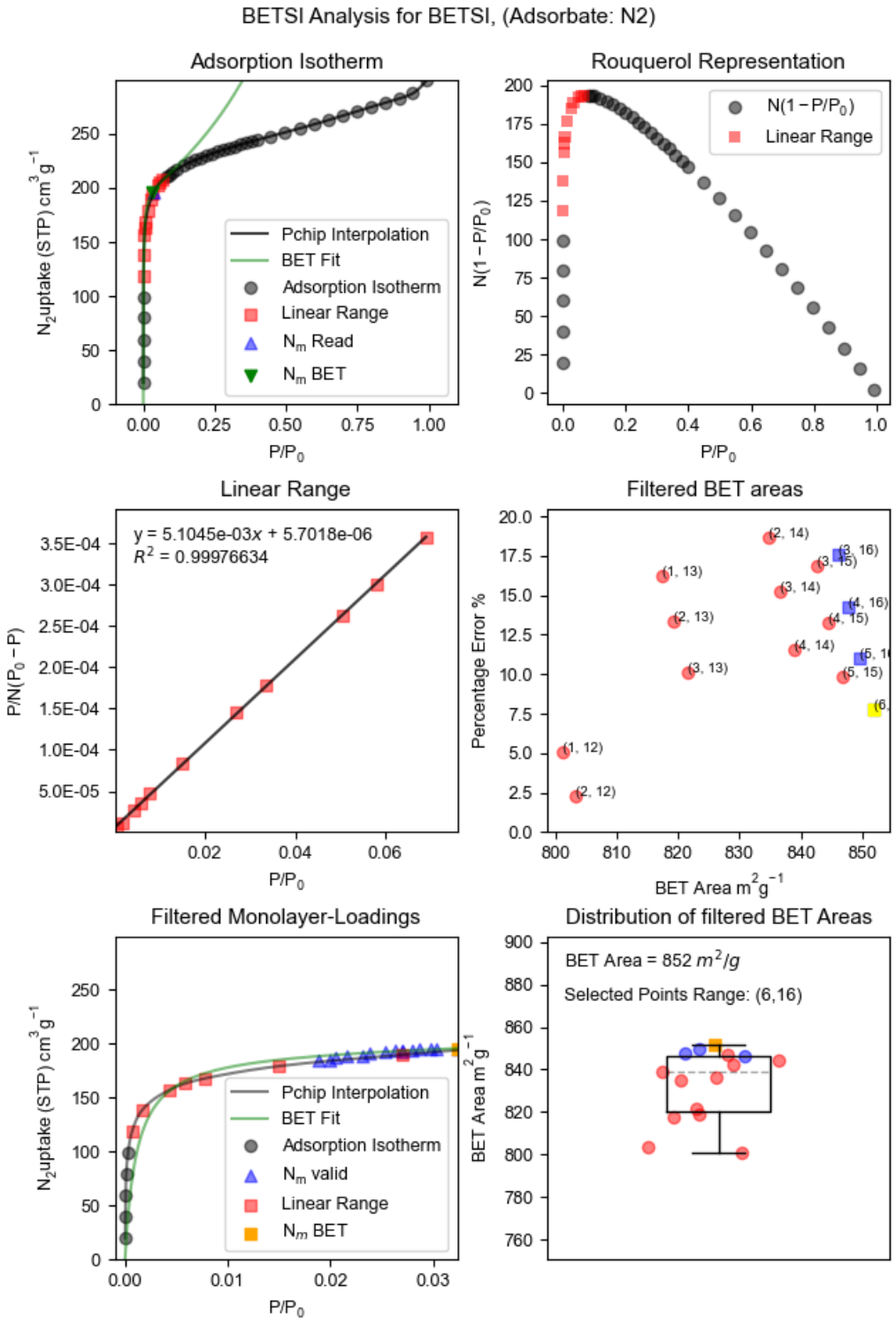

Figure S32. Ar adsorption isotherm of COF-412 measured at 87 K.

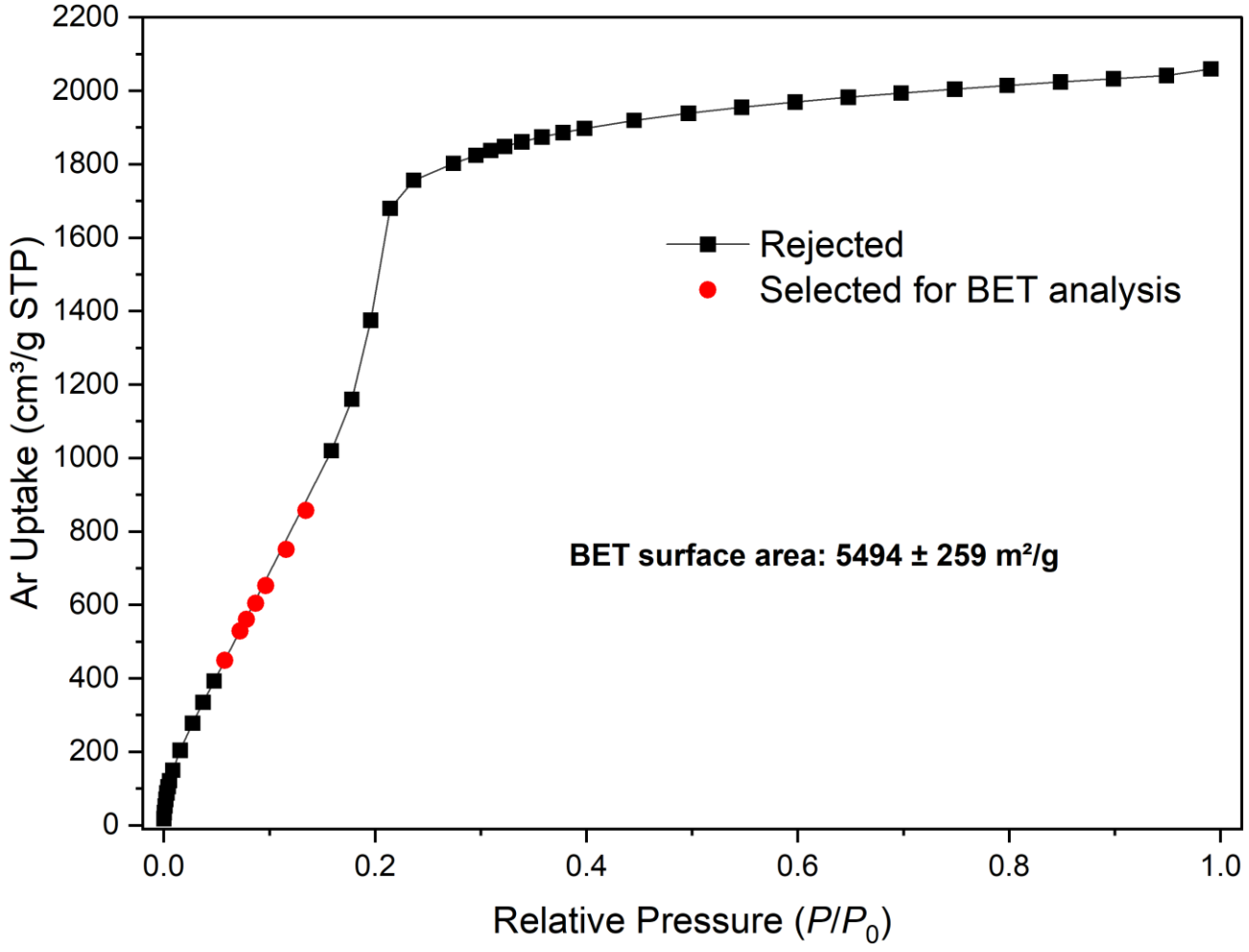

Figure S33. Rouquerol plot to determine appropriate points for BET analysis using the Ar adsorption isotherm of COF-412 measured at 87 K.

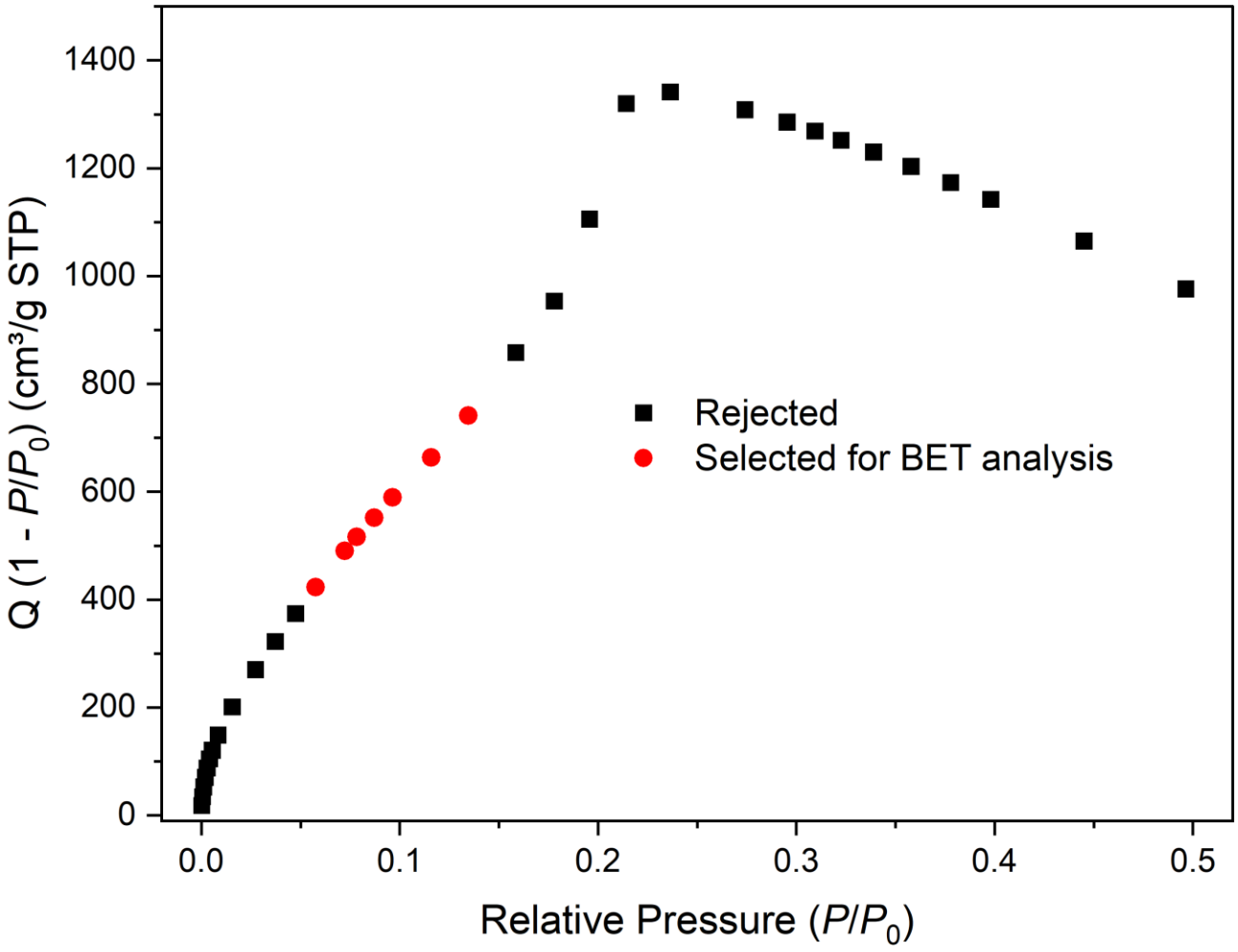

Figure S34. BET plot of COF-412 using the Ar adsorption isotherm measured at 87 K.

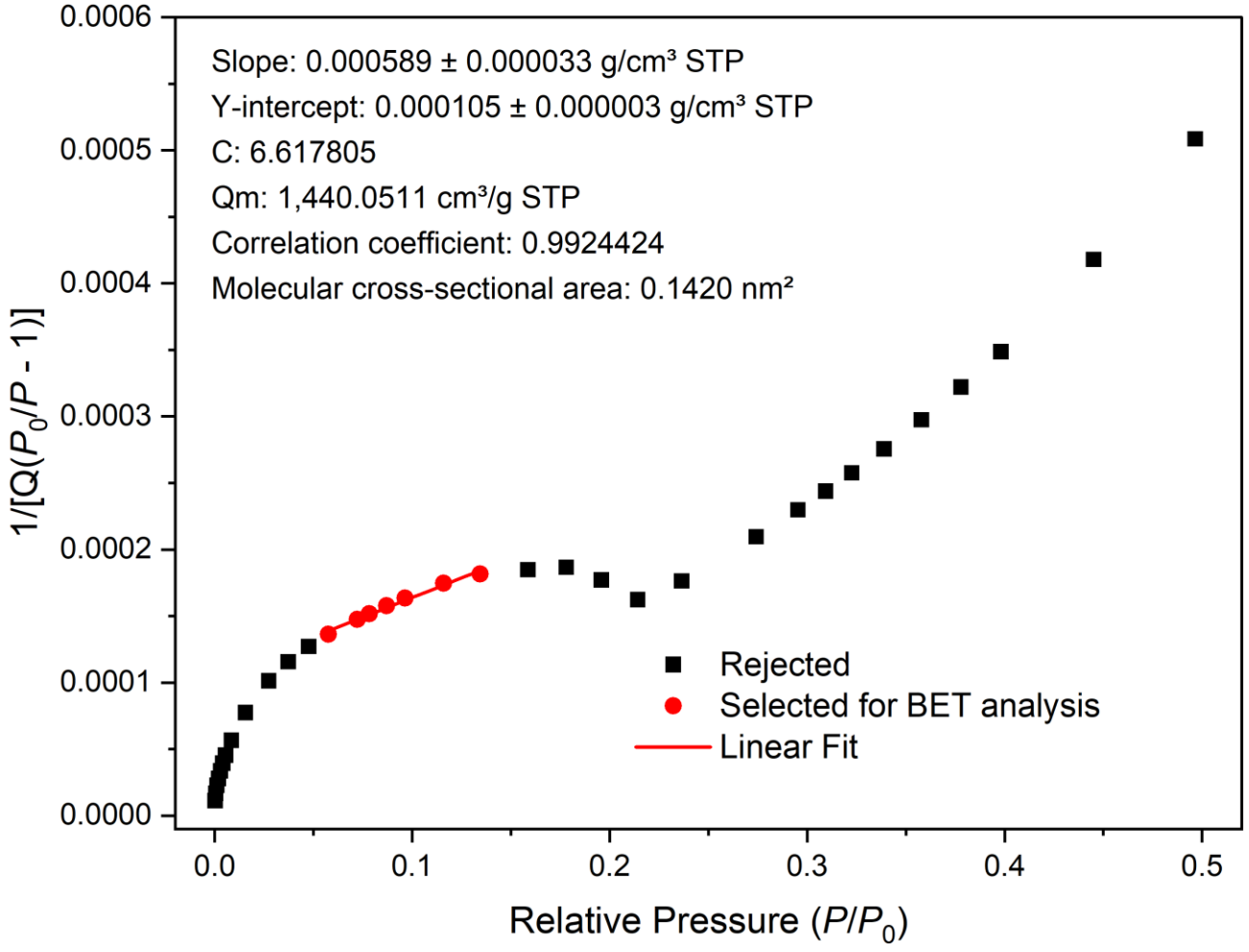

Figure S35. N_2 adsorption isotherm of COF-412 measured at 77 K.

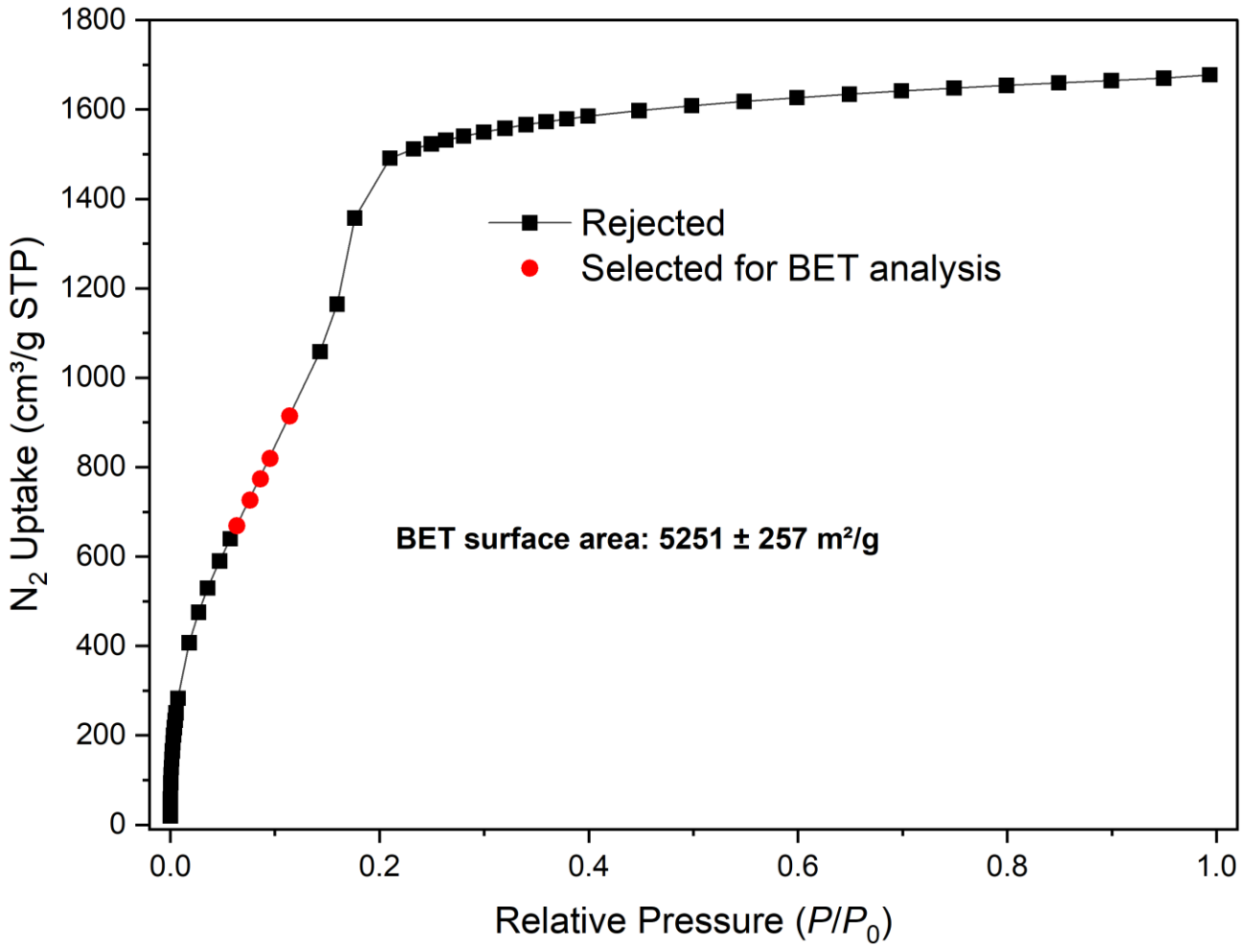

Figure S36. Rouquerol plot to determine appropriate points for BET analysis using the N_2 adsorption isotherm of COF-412 measured at 77 K.

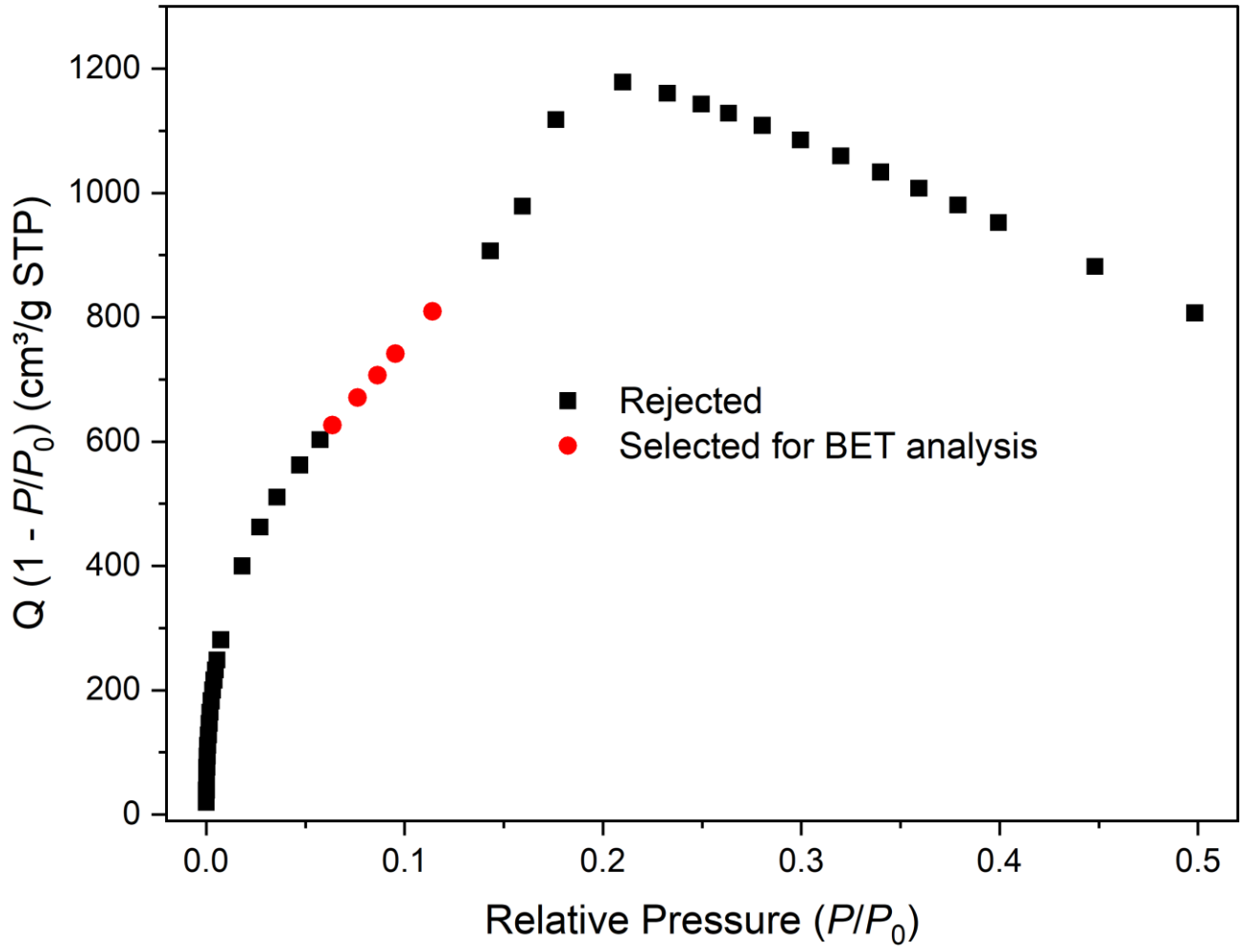

Figure S37. BET plot of COF-412 using the N_2 adsorption isotherm measured at 77 K.

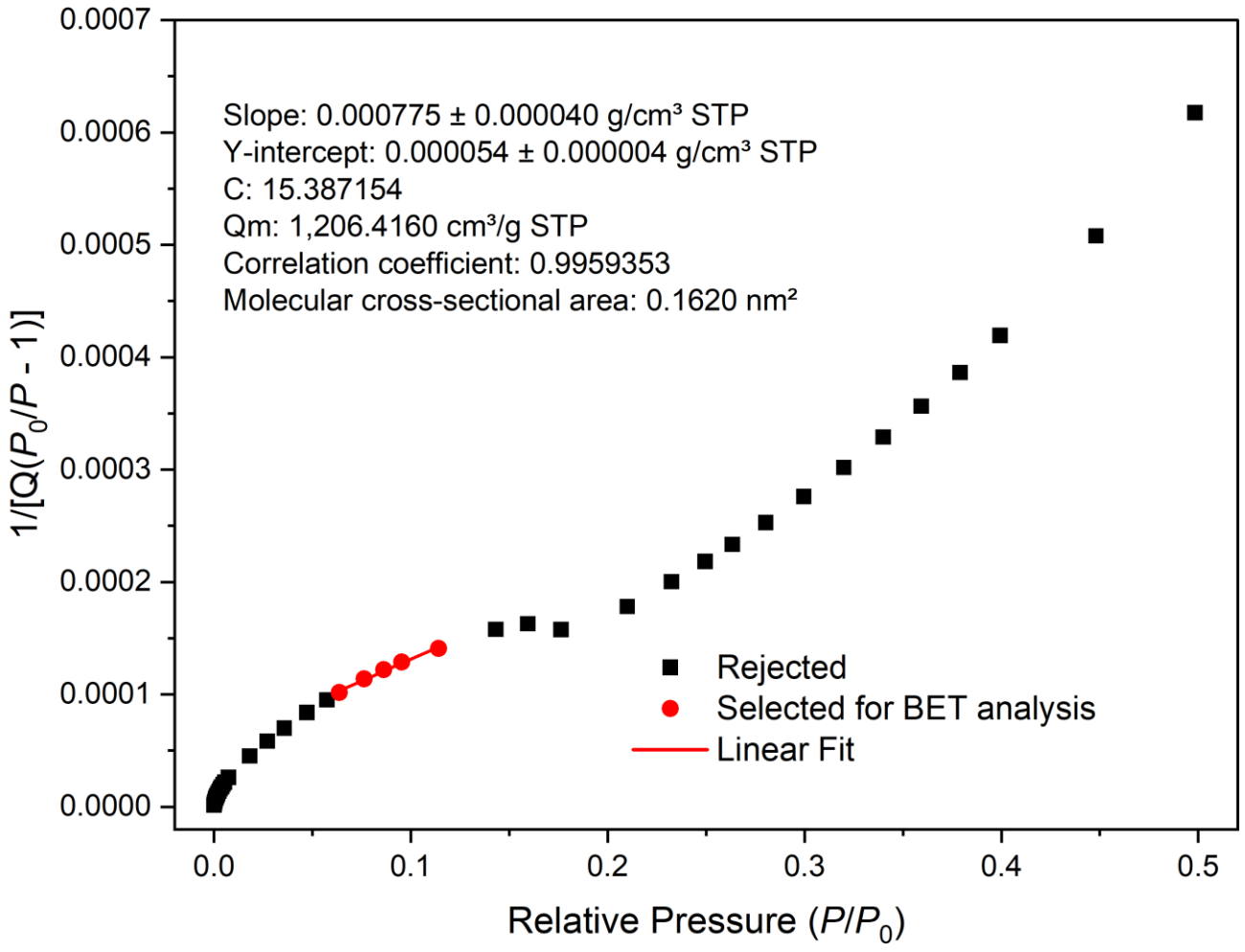

Figure S38. Pore size distribution (PSD) analysis of COF-612. PSD was determined from N_2 adsorption isotherms at 77 K using the NLDFT model (cylindrical pore geometry, pillared clay/AMS deconvolution) via MicroActive 7.00. Geometrical PSD was calculated using Zeo++ with a probe radius of 1.82 Å.

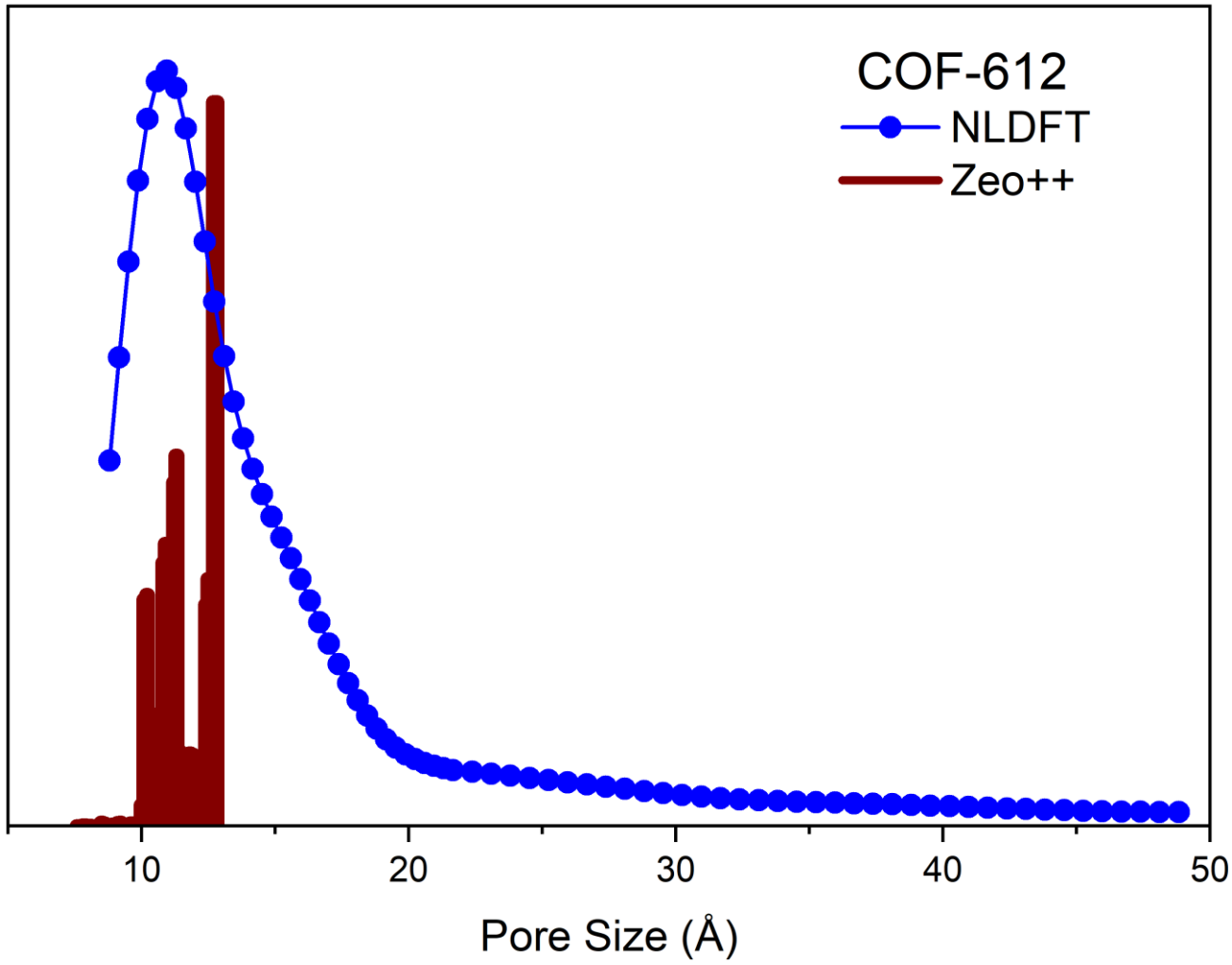

Figure S39. Pore size distribution (PSD) analysis of COF-412. PSD was determined from N_2 adsorption isotherms at 77 K using the NLDFT model (cylindrical pore geometry, pillared clay/AMS deconvolution) via MicroActive 7.00. Geometrical PSD was calculated using Zeo++ with a probe radius of 1.82 Å.

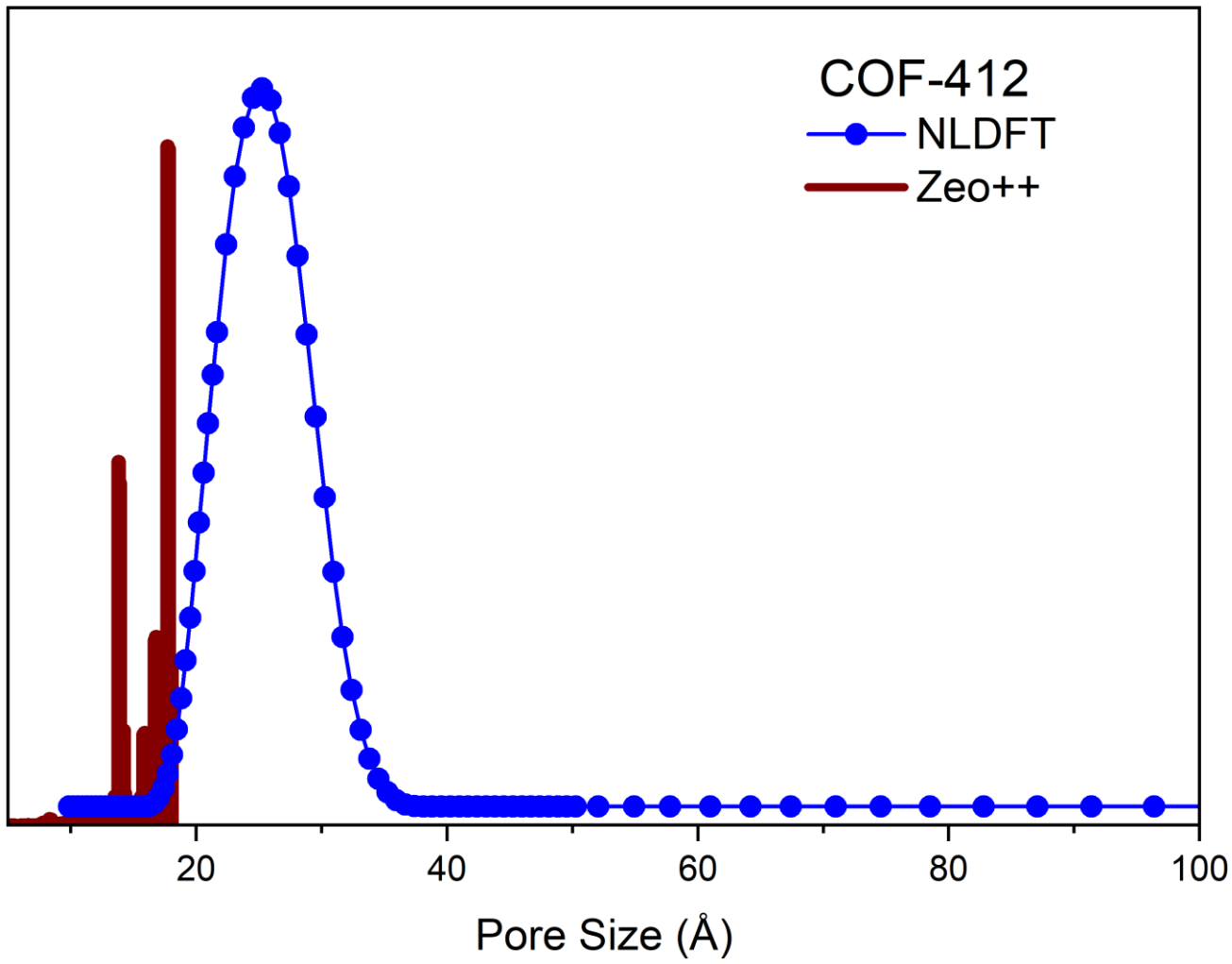

Table S2. Comparison of gravimetric BET surface areas (GSA) of selected highly porous COFs obtained from N_2 adsorption isotherms reported in the literature.

	GSA (m^2 g^{-1})	Ref.
COF-412	**5251 (5494)[a]**	**This work**
COF-612	**841**	
COF-682	3971	11
COF-683	5155	
DBA-3D-COF	5083	12
3D-TFBCOF-Me	4298	13
3D-TFB-COF-Et	4502	
TAPB-TFS-COF	4107	14
AM-TFPB-COF	3533	
COF-102	3620	15
COF-103	3530	
3D pts COF	3478	16
JUC-564	3383	17
JUC-552	3023	18
JUC-518	3018	19

[a] *Value in parentheses obtained from the Ar sorption isotherm measured at 87 K.*

Figure S40. TGA analysis of COF-612 after activation.

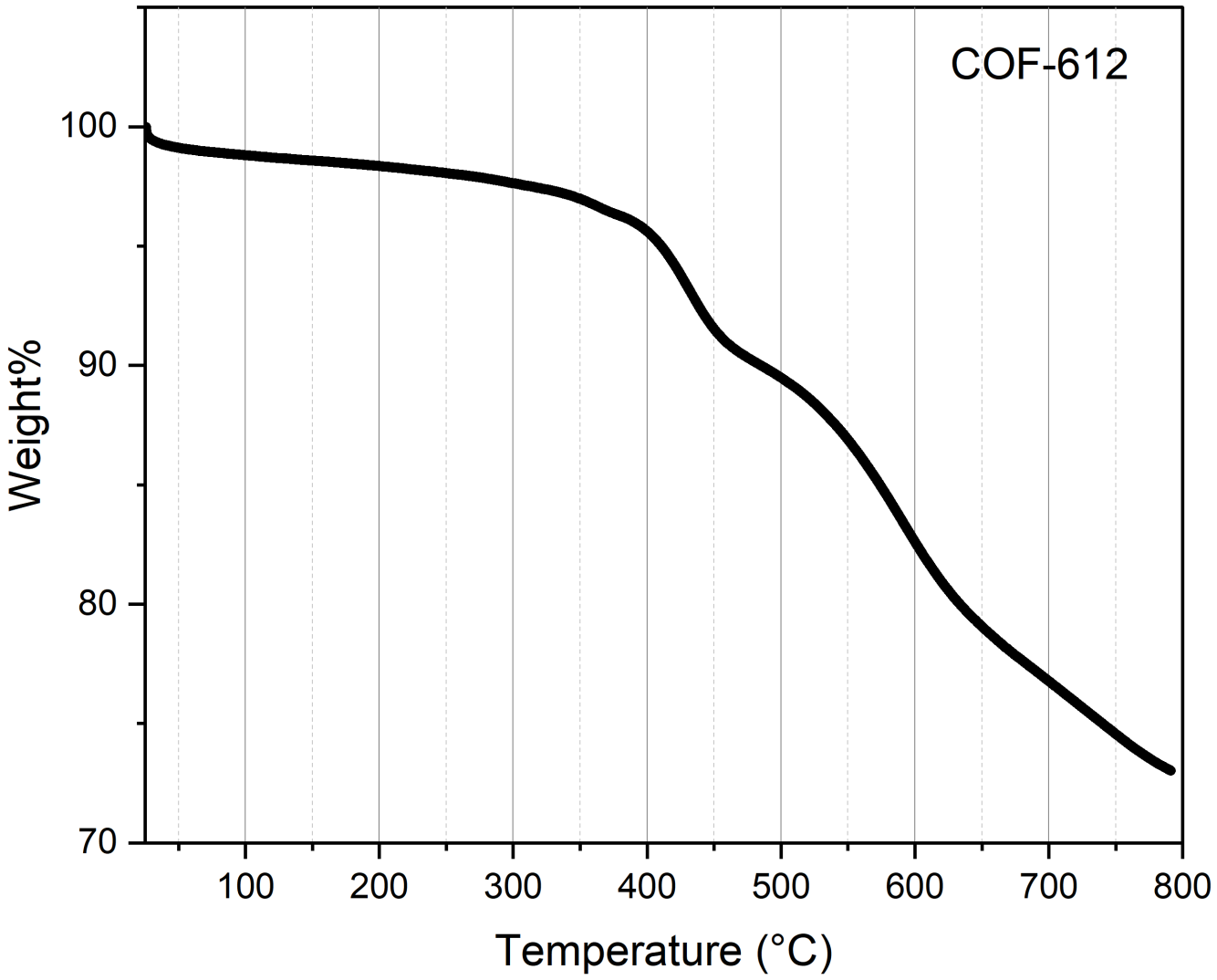

Figure S41. TGA analysis of COF-412 after activation.

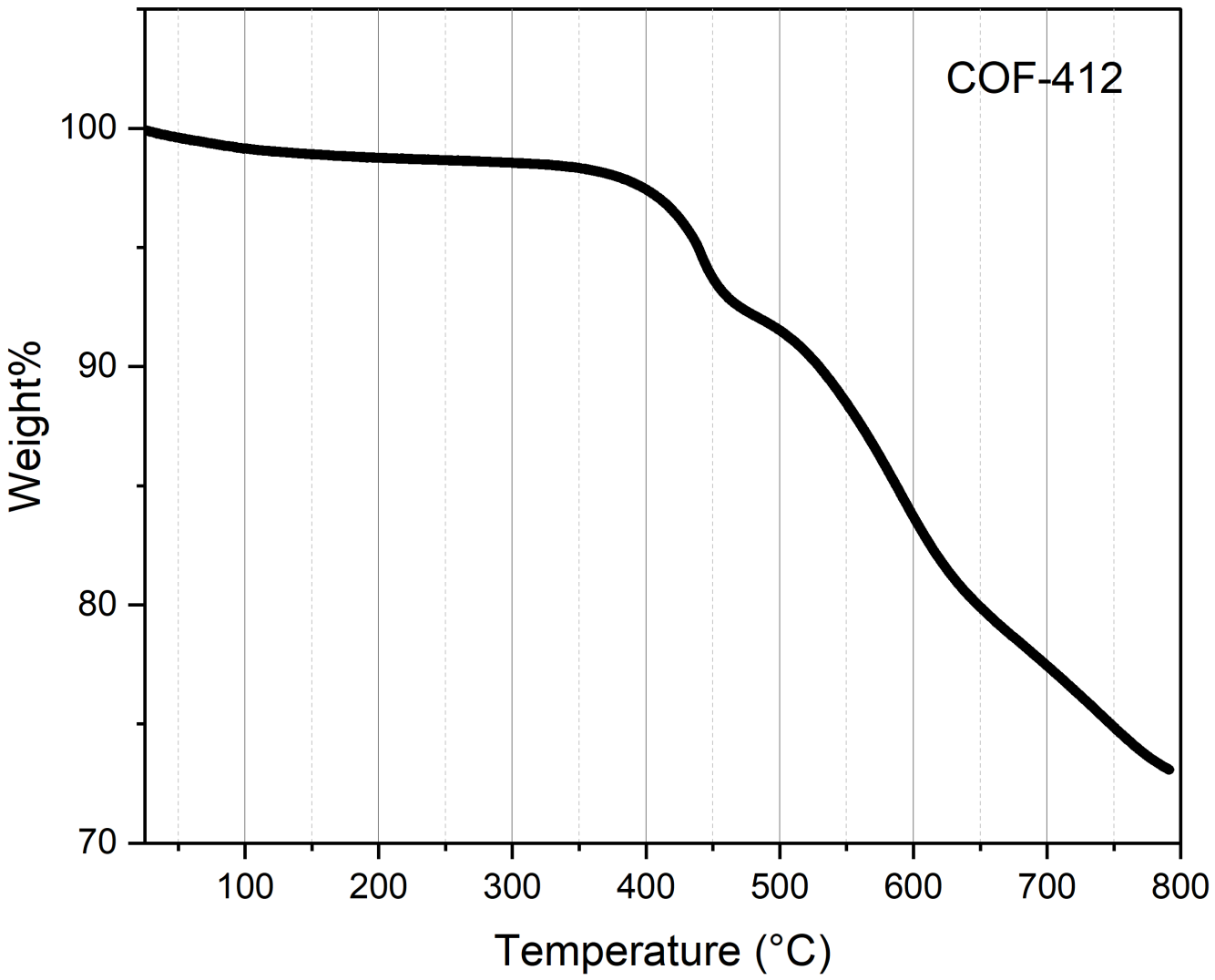

S5. Fourier-Transform Infrared Spectroscopy (FT-IR)

Figure S42. Stacked FT-IR spectra of HBC-LA_{12}, HAPT, and COF-612.

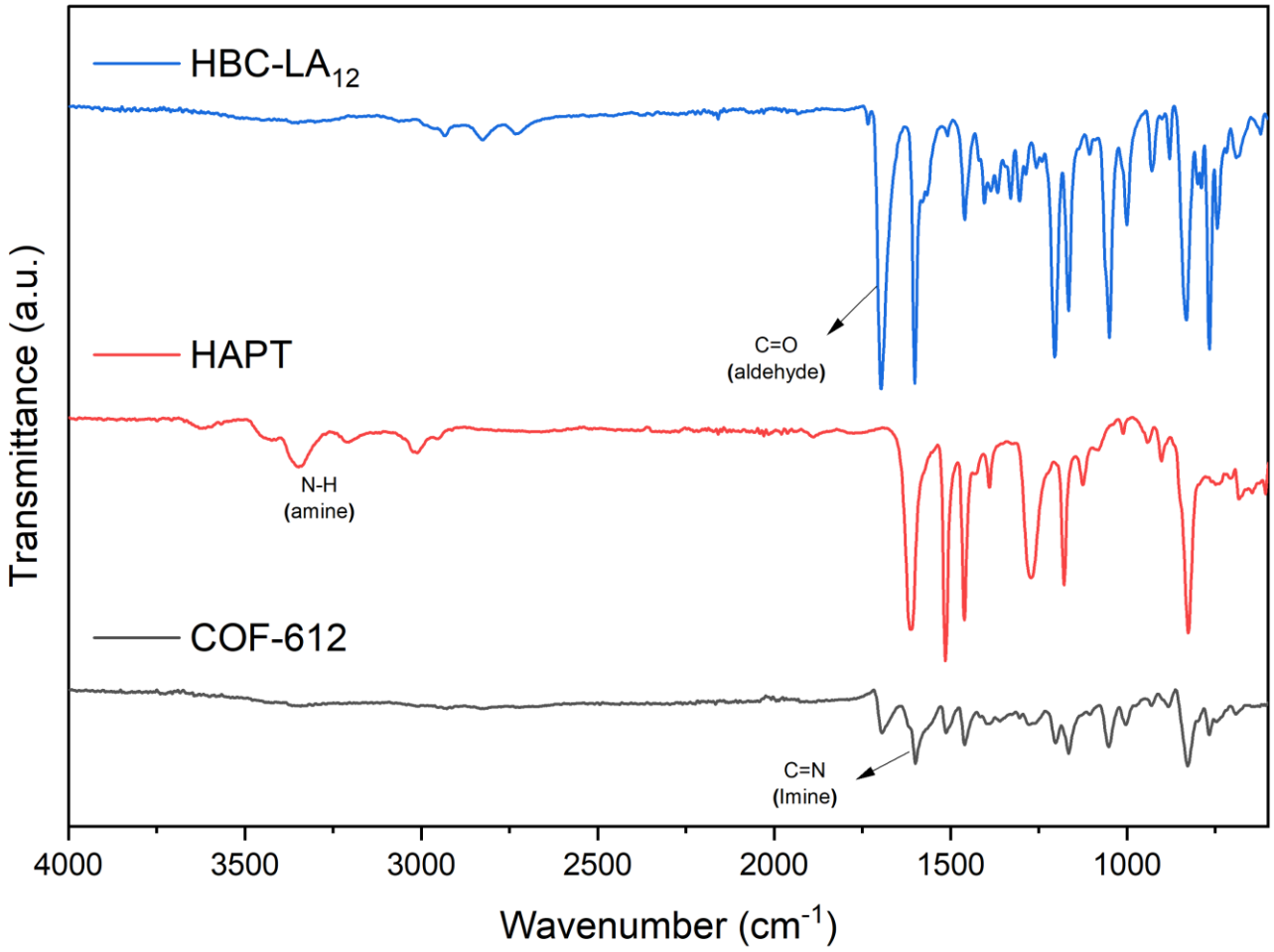

Figure S43. Stacked FT-IR spectra of HBC-LA$_{12}$, PyTTA, and COF-412.

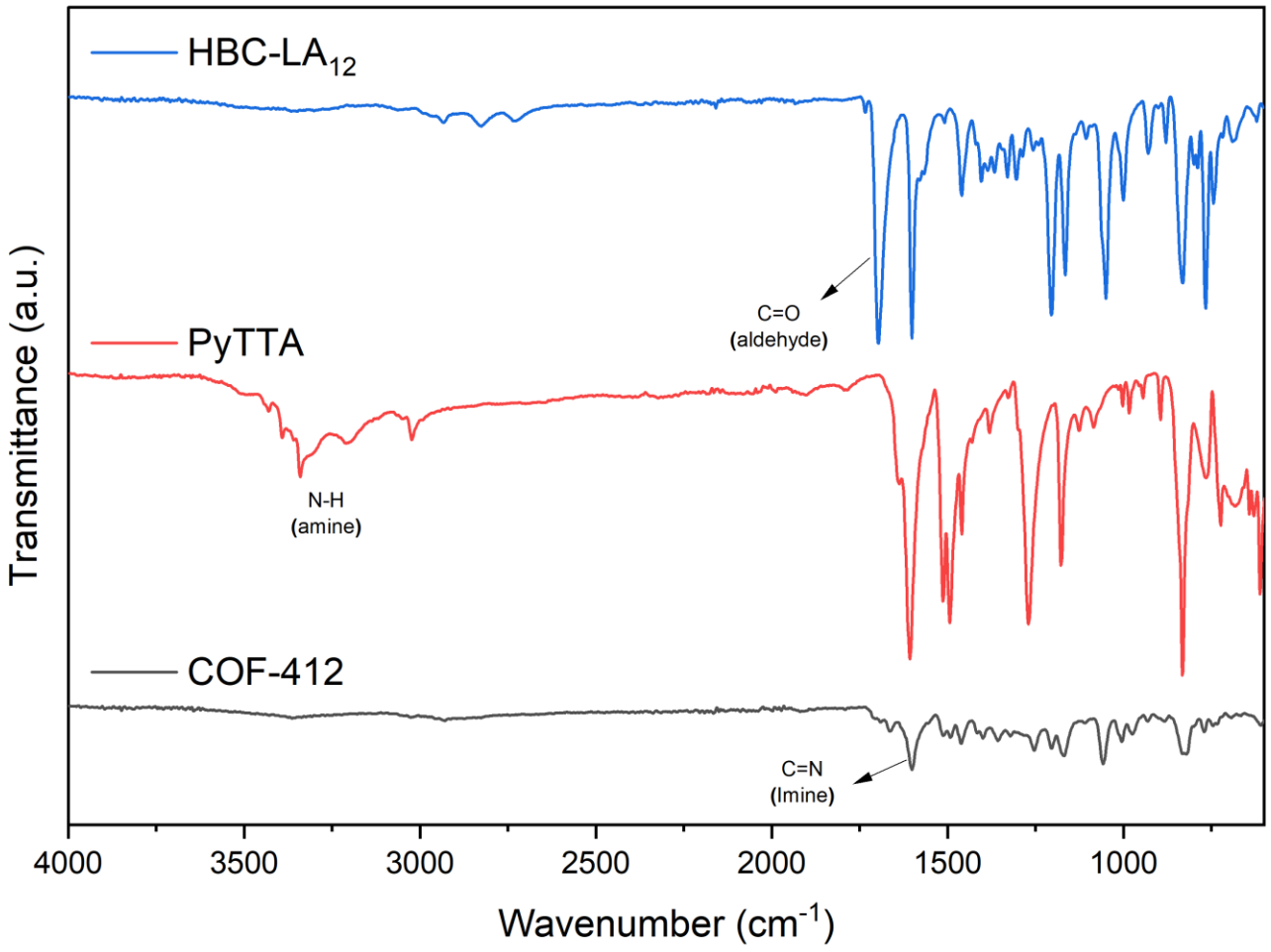

S6. Solid-state UV-vis and Emission

Figure S44. Stacked solid-state UV-vis spectra of HBC-LA_{12}, HAPT, and COF-612.

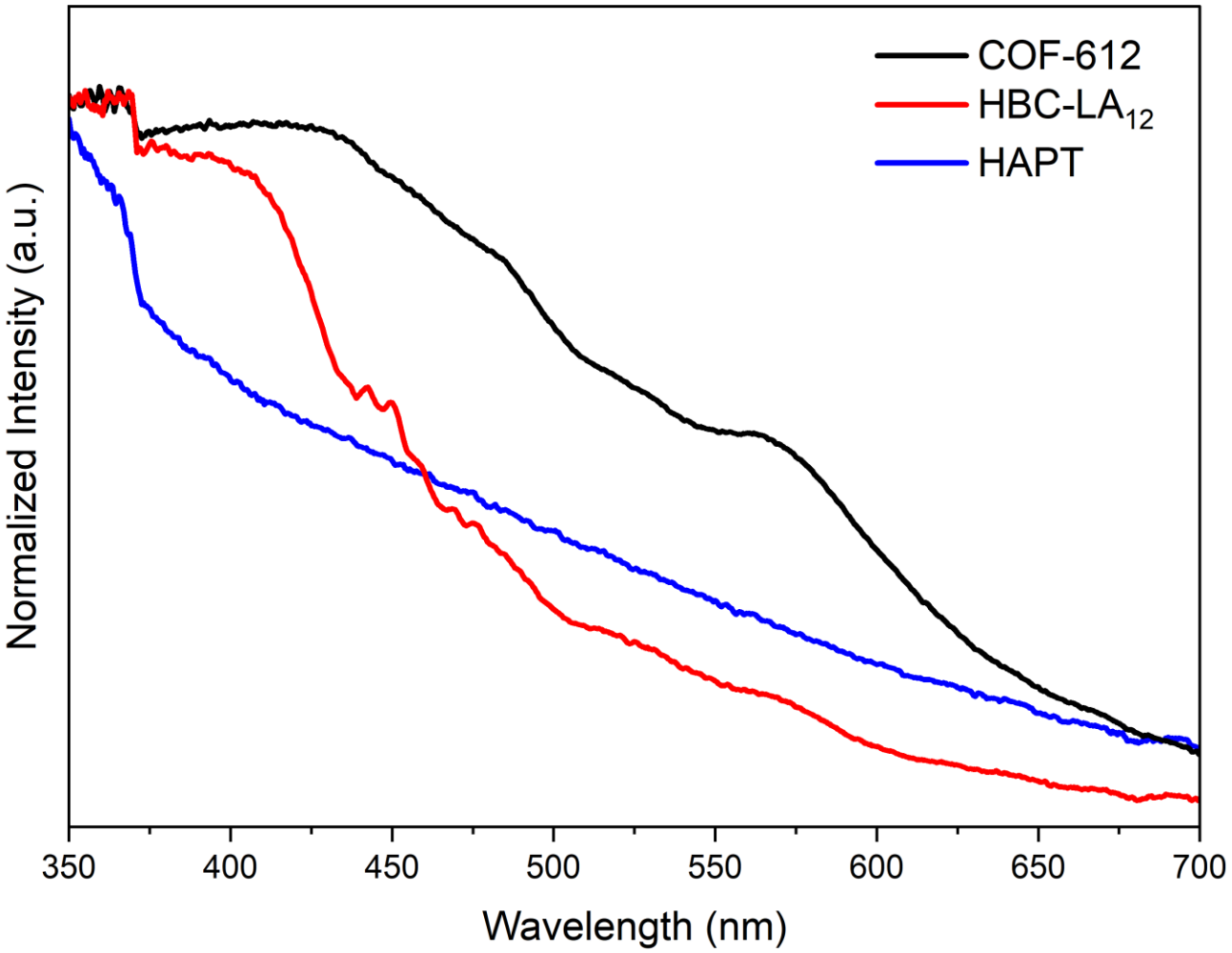

Figure S45. Stacked solid-state UV-vis spectra of HBC-LA_{12}, PyTTA, and COF-412.

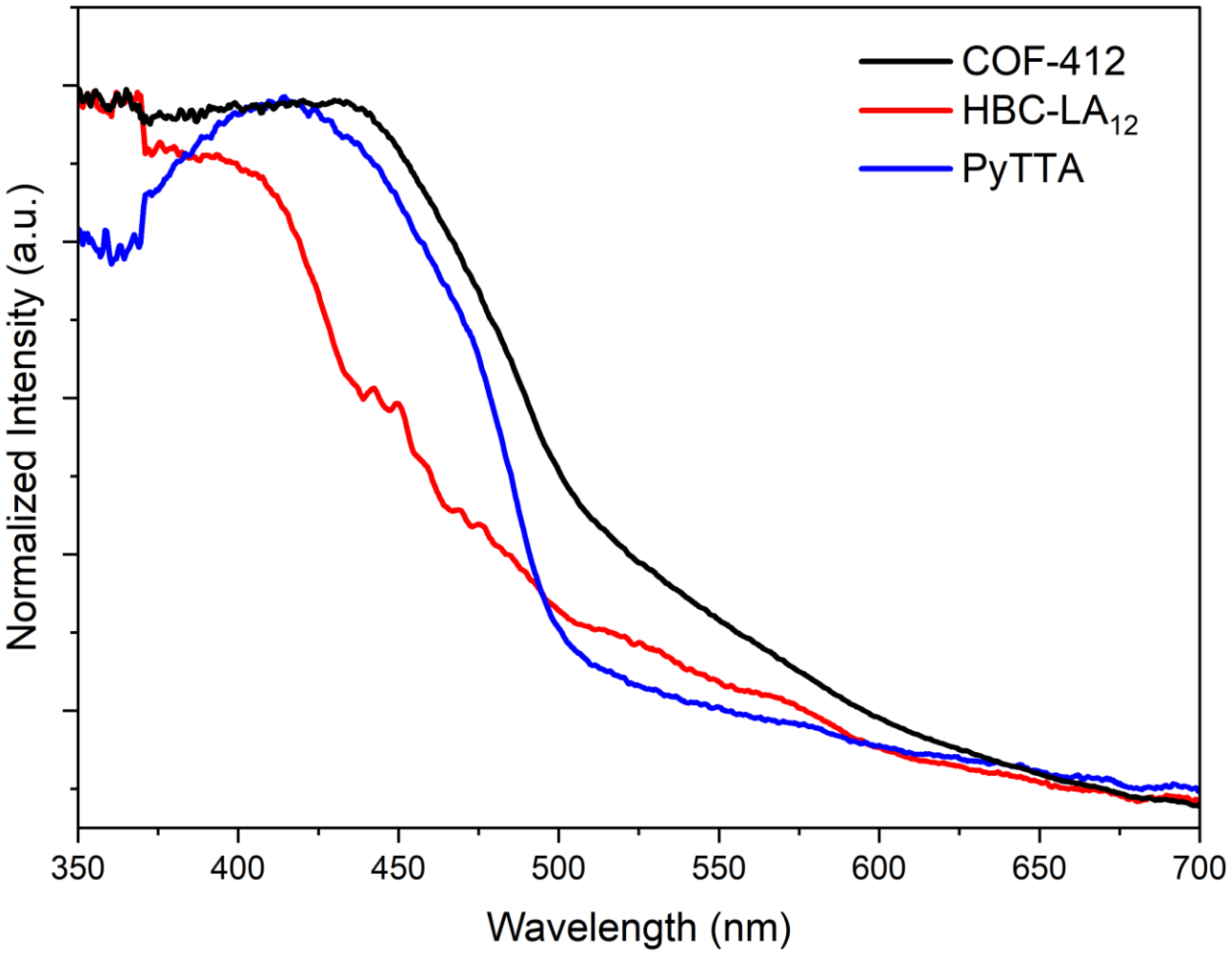

Figure S46. Tauc plot derived from the UV-Vis spectrum of COF-612 for the determination of the optical bandgap.

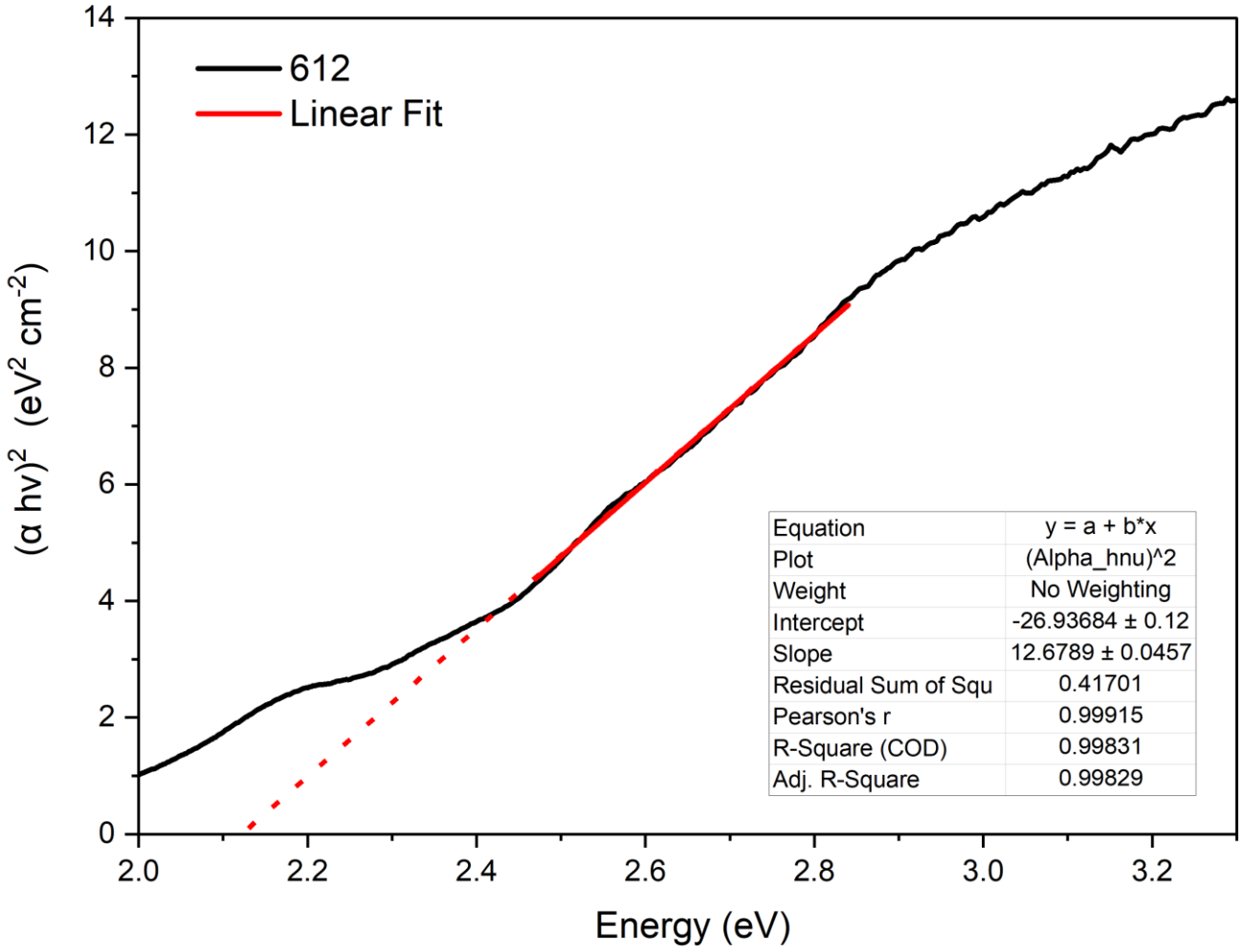

Figure S47. Tauc plot derived from the UV-Vis spectrum of COF-412 for the determination of the optical bandgap.

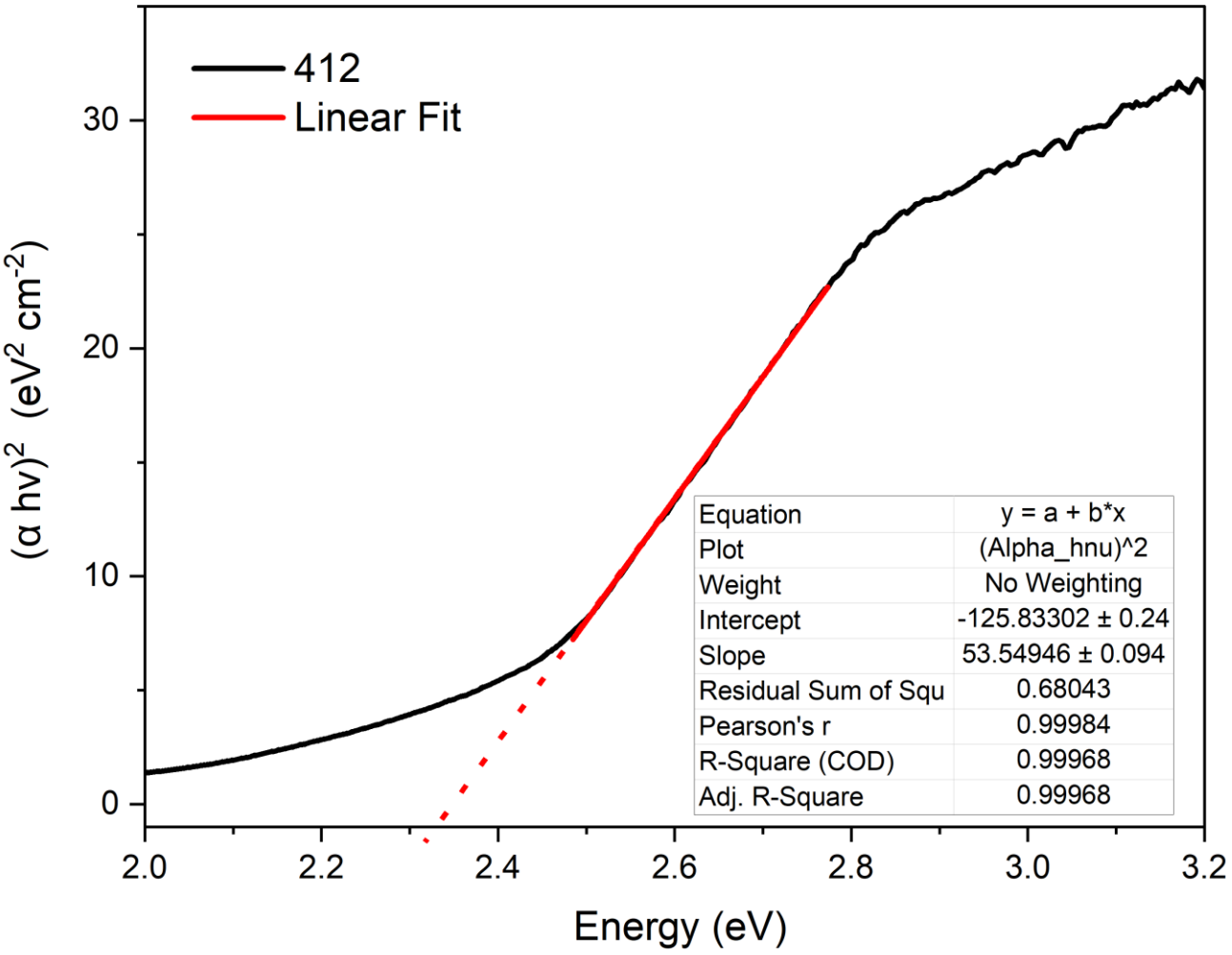

Figure S48. Stacked solid-state photoluminescence spectra of HBC-LA_{12}, HAPT, and COF-612.

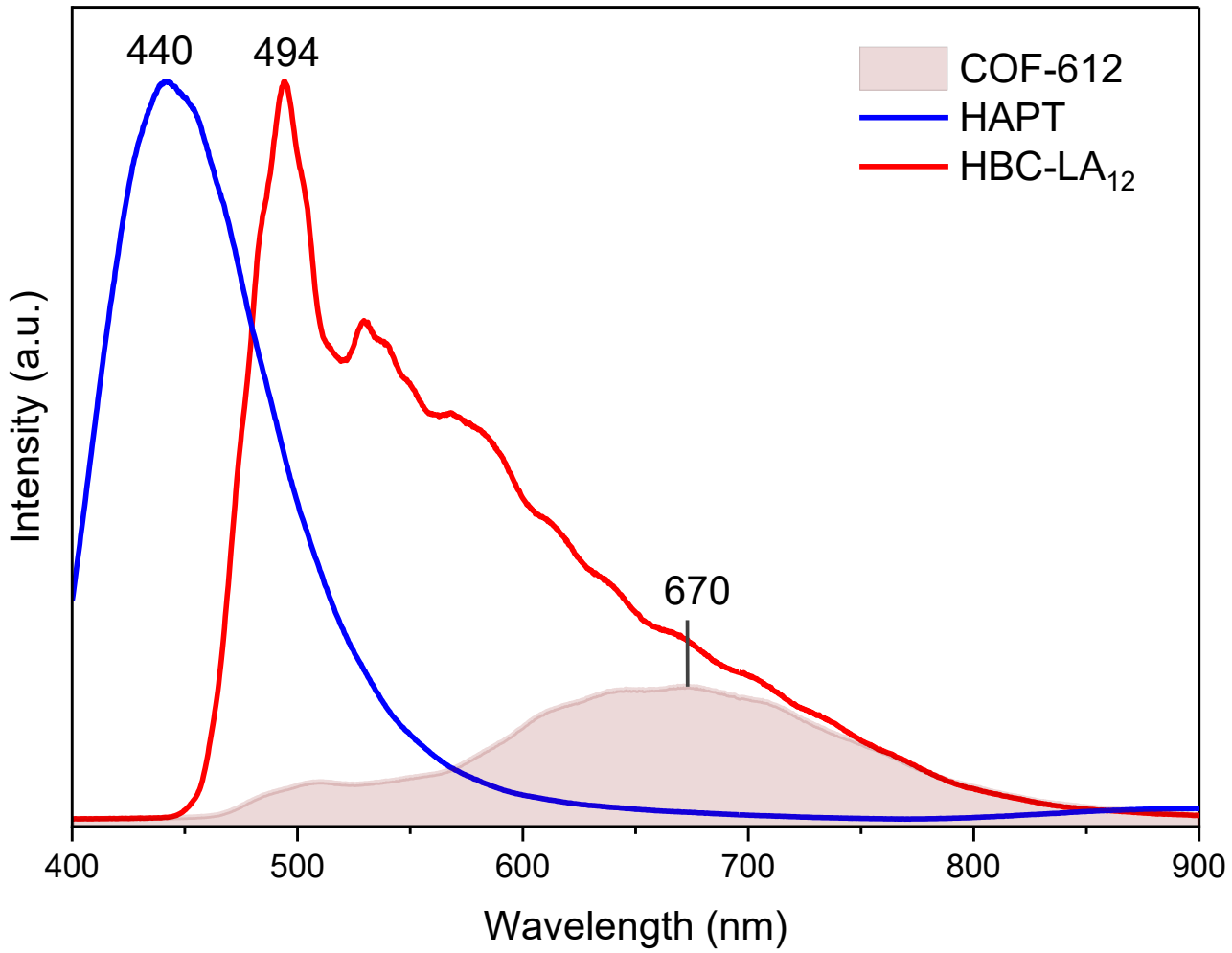

Figure S49. Stacked solid-state photoluminescence spectra of HBC-LA_{12}, PyTTA, and COF-412.

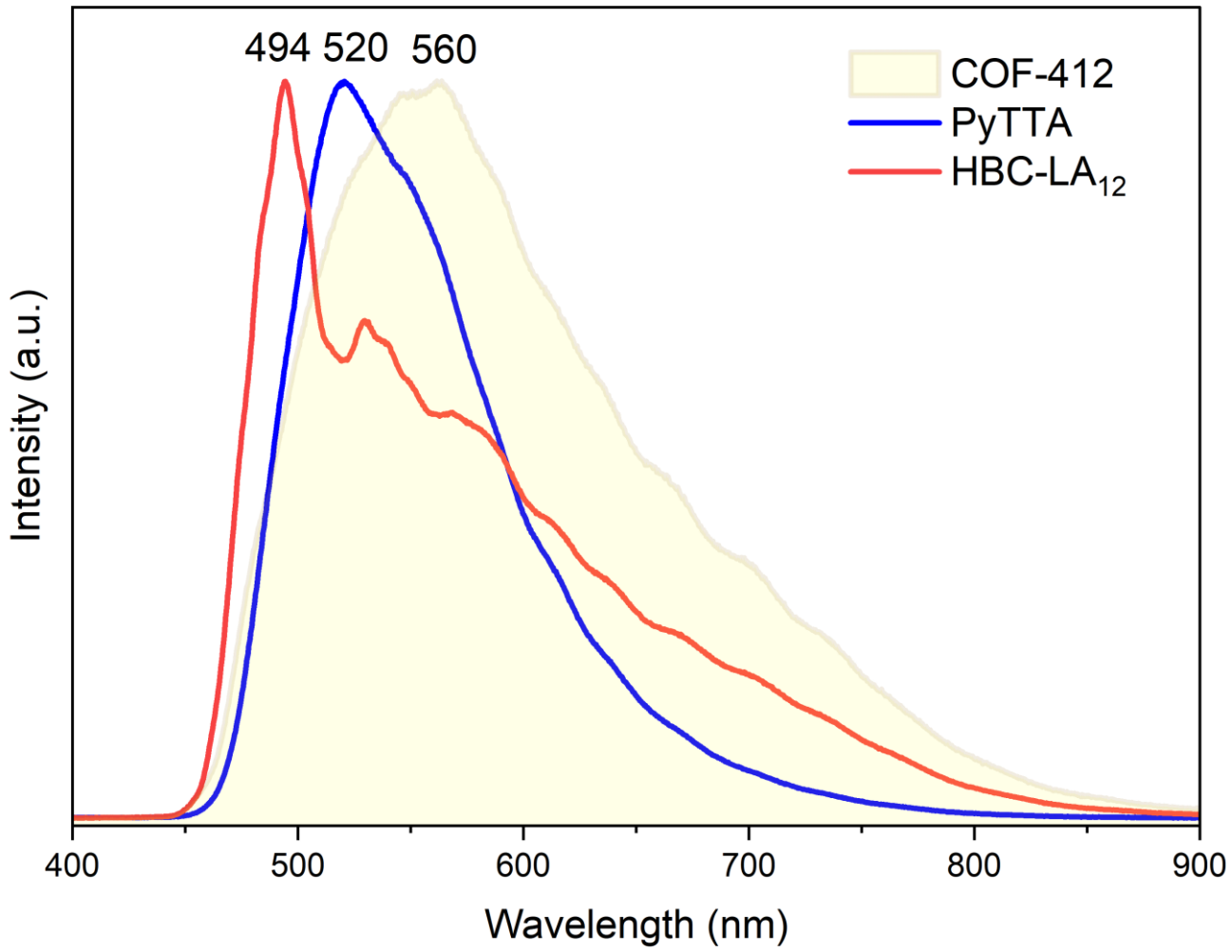

S6. NMR spectroscopy.

Figure S50. ^{1}H and ^{13}C NMR spectra of **HBC-LA$_{12}$** ($CDCl_3$, 20 °C)

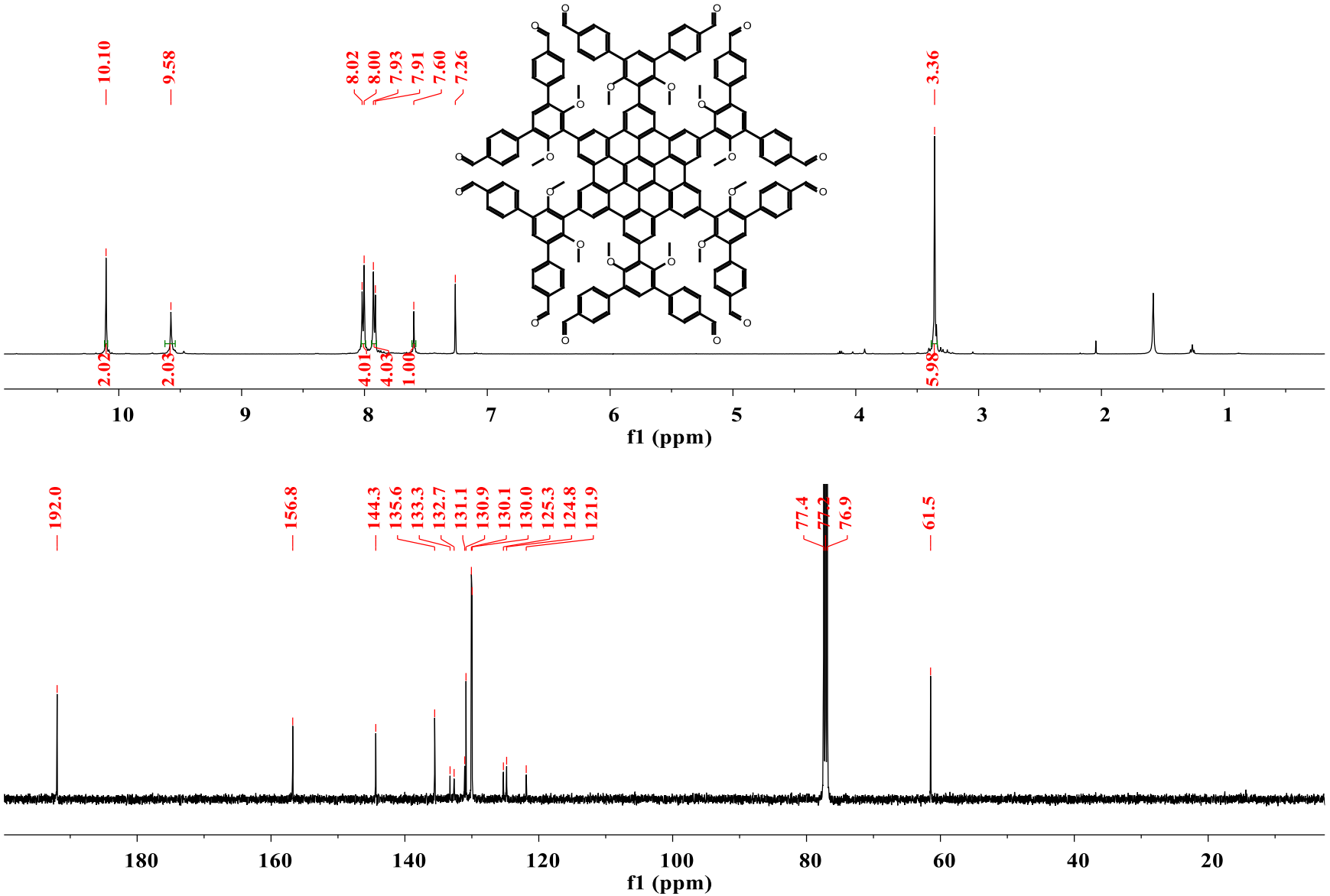

Figure S51. COSY NMR spectrum of **6** ($CDCl_3$, 20 °C)

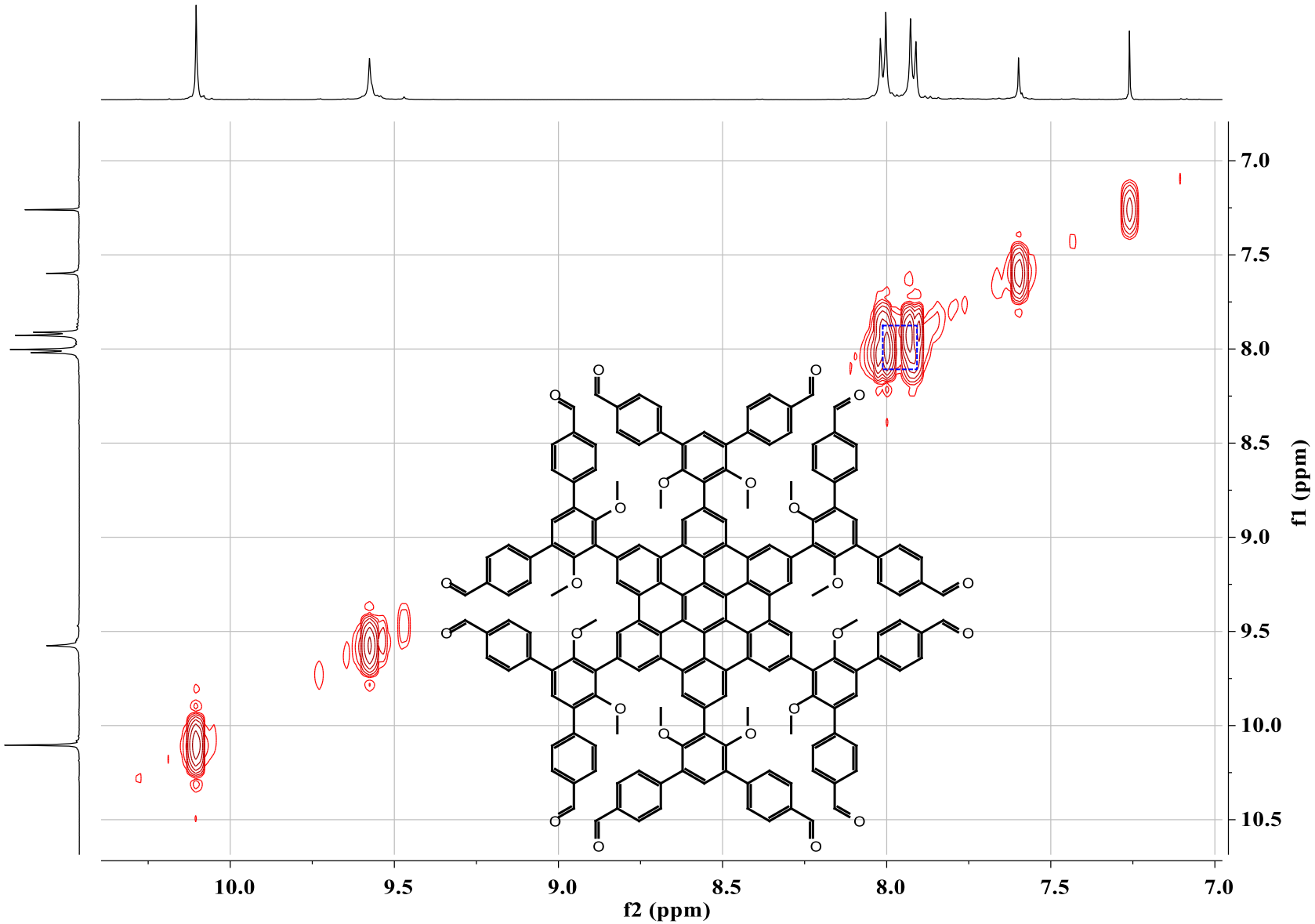

Figure S52. ^{1}H NMR spectrum of digested COF-612 (4 mg) in 35% DCl in D_2O/DMSO-d_6/$CDCl_3$ solution (v/v/v = 50/500/200 µL). The proton peak of DMSO is at 2.50. Methine peak of HAPT linker is covered by protonated amine groups at 5.89 ppm. Based on the integration of NMR peaks, the ratio of HBC-LA_{12} over HAPT linker is about 1:2 which exactly matches the 1:2 ration of these linkers in the COF-612.

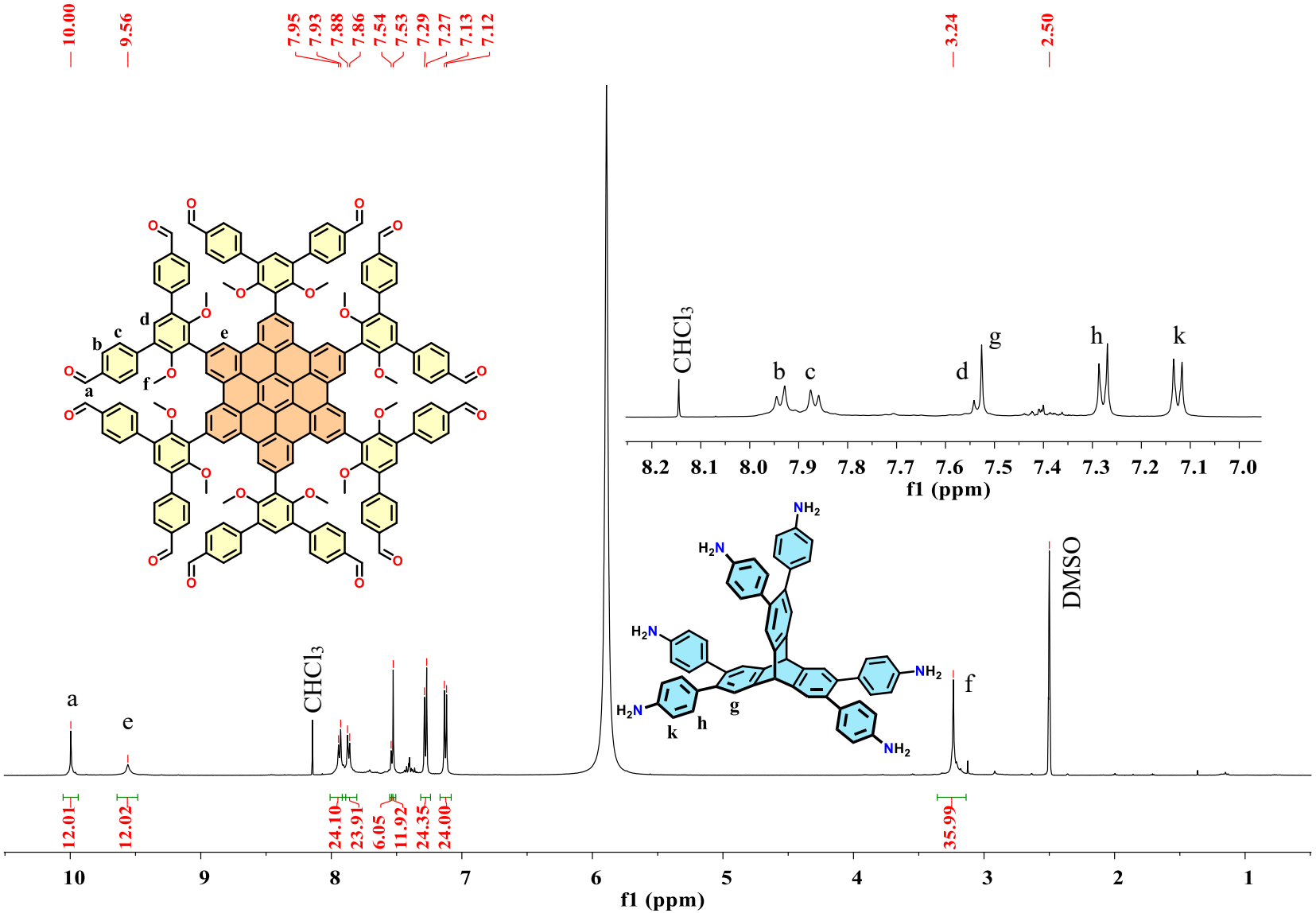

Figure S53. ^{1}H NMR spectrum of digested COF-412 (4 mg) in 35%DCl in D_2O/DMSO-d_6 solution (v/v/v = 50/700 µL). The proton peak of DMSO is at 2.50. Based on the integration of NMR peaks, the ratio of HBC-LA_{12} over PyTTA linker is about 1:3 which exactly matches the 1:3 ration of these linkers in the COF-412.

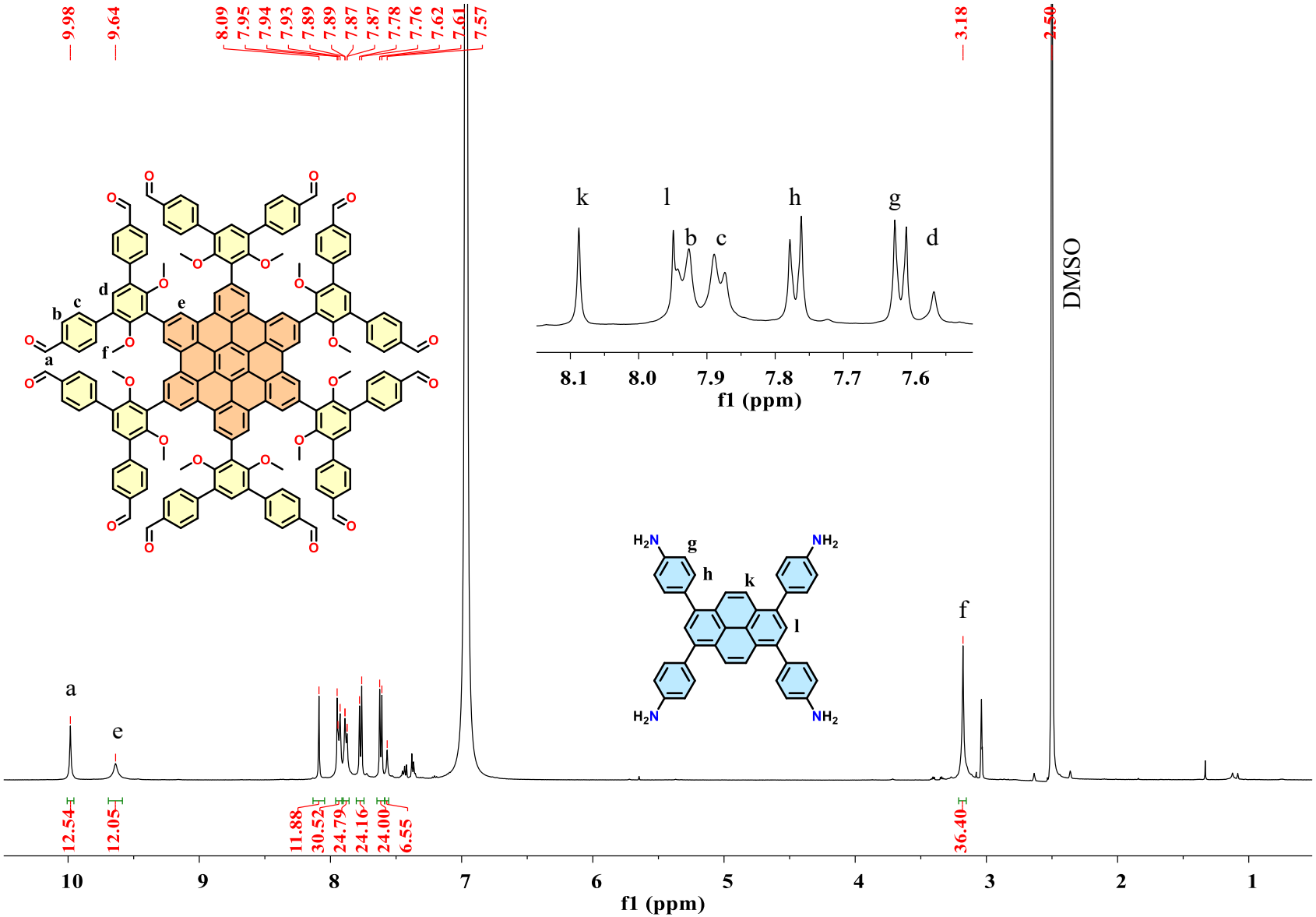

Figure S54. Stacked solid-state ^{13}C NMR spectra of HBC-LA_{12}, HAPT, and COF-612. The minor signal at ~190 ppm is attributed to residual aldehyde end-groups at the crystallite surfaces or defect sites within the COF-612.

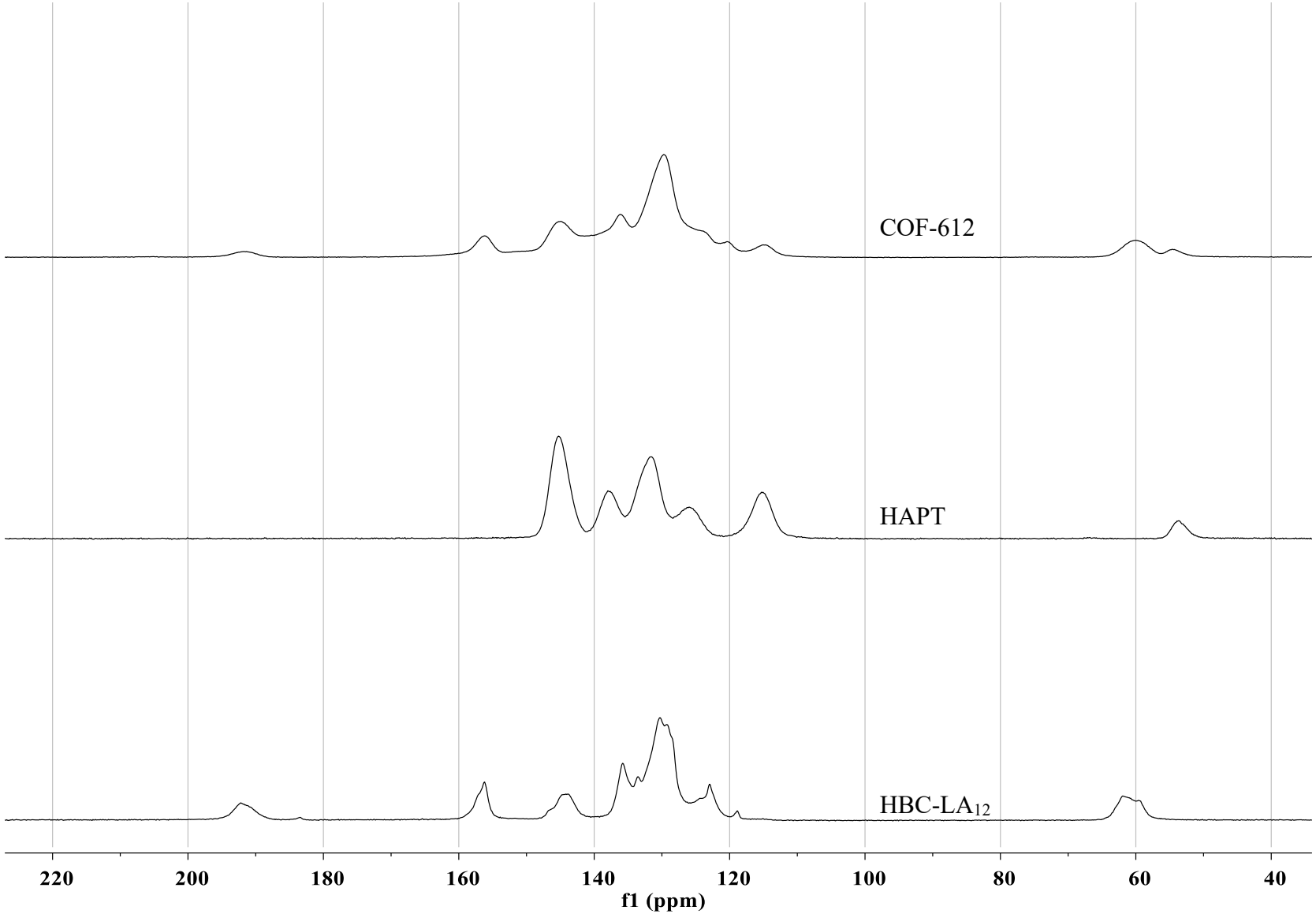

Figure S55. Stacked solid-state ^{13}C NMR spectra of HBC-LA_{12}, PyTTA, and COF-412. The minor signal at ~190 ppm is attributed to residual aldehyde end-groups at the crystallite surfaces or defect sites within the COF-412.

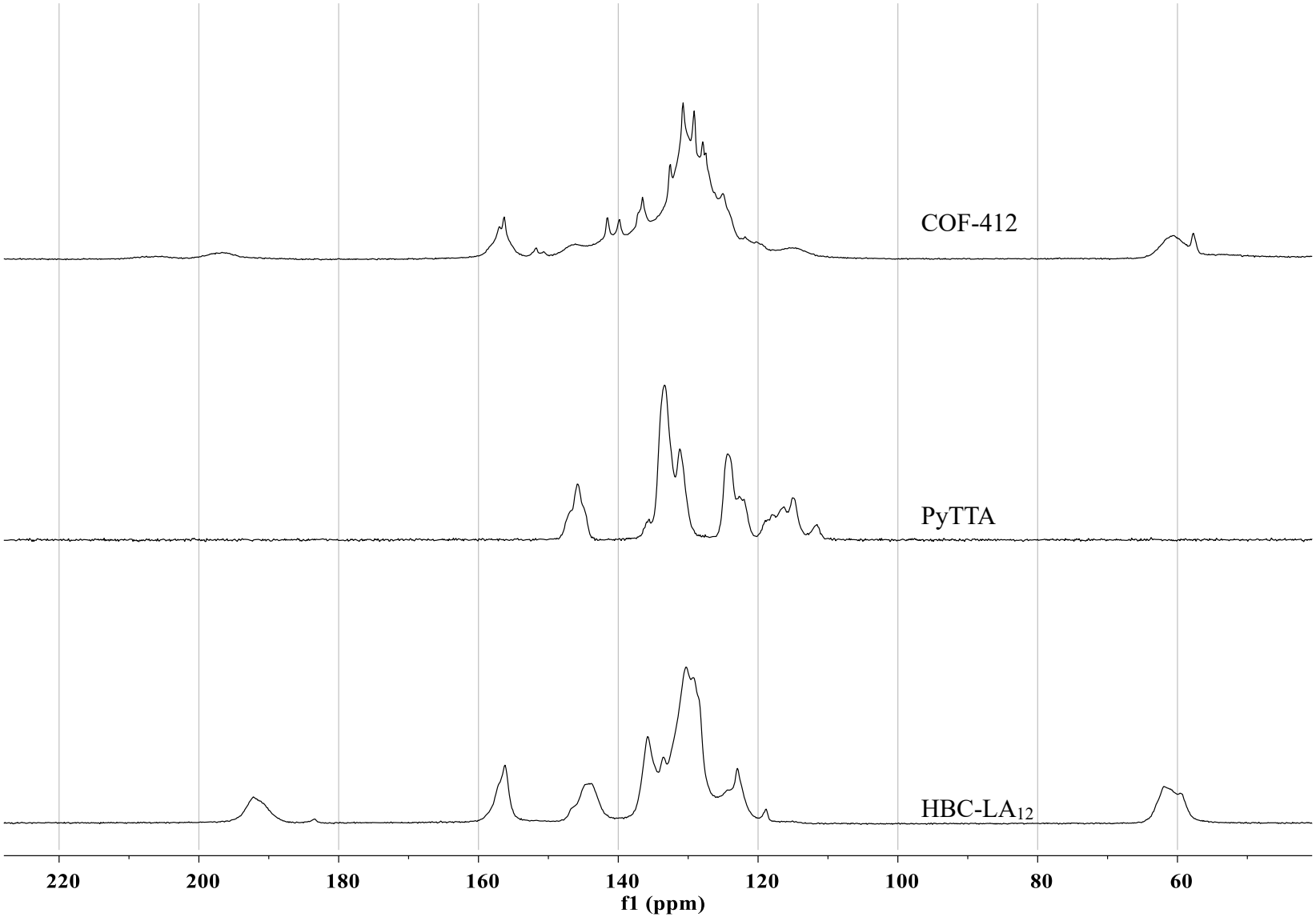

S7. References.

1. Fung, B.M., Khitrin, A.K., and Ermolaev, K. (2000). An Improved Broadband Decoupling Sequence for Liquid Crystals and Solids. J. Magn. Reson. *142*, 97-101. https://doi.org/10.1006/jmre.1999.1896.
2. Kieffer, J., and Karkoulis, D. (2013). PyFAI, a versatile library for azimuthal regrouping. Journal of Physics: Conference Series *425*, 202012. https://doi.org/10.1088/1742-6596/425/20/202012.
3. Bruker AXS Inc. SADABS. (2016).
4. Spek, A. (2003). Single-crystal structure validation with the program PLATON. J. Appl. Crystallogr. *36*, 7-13. https://doi.org/10.1107/S0021889802022112.
5. Sheldrick, G. (2015). SHELXT - Integrated space-group and crystal-structure determination. Acta Crystallogr. A *71*, 3-8. https://doi.org/10.1107/S2053273314026370.
6. Sheldrick, G. (2015). Crystal structure refinement with SHELXL. Acta Crystallogr. C *71*, 3-8. https://doi.org/10.1107/S2053229614024218.
7. Dolomanov, O.V., Bourhis, L.J., Gildea, R.J., Howard, J.A.K., and Puschmann, H. (2009). OLEX2: a complete structure solution, refinement and analysis program. J. Appl. Crystallogr. *42*, 339-341. https://doi.org/10.1107/S0021889808042726.
8. van der Sluis, P., and Spek, A.L. (1990). BYPASS: an effective method for the refinement of crystal structures containing disordered solvent regions. Acta Crystallogr. A *46*, 194-201. https://doi.org/10.1107/S0108767389011189.
9. Mirzaei, S., Gao, M.-Y., Alawadhi, A.H., Nguyen, H.L., Zhou, Z., Singh, V., Ahn, D.D., Proserpio, D.M., O'Keeffe, M., and Yaghi, O.M. (2026). Twelve-connected nanographene-based metal-organic frameworks. Chem *12*, 102830. https://doi.org/10.1016/j.chempr.2025.102830.
10. Osterrieth, J.W.M., Rampersad, J., Madden, D., Rampal, N., Skoric, L., Connolly, B., Allendorf, M.D., Stavila, V., Snider, J.L., Ameloot, R., et al. (2022). How Reproducible are Surface Areas Calculated from the BET Equation? Adv. Mater. *34*, 2201502. https://doi.org/10.1002/adma.202201502.
11. Mirzaei, S., Saeed Mirzaei, M., Wang, W., Nguyen, H.L., Wang, K., Gándara, F., Gao, M.-Y., Khosropour, A., Naninga, B.L., Zhang, Y.-B., et al. Single-crystalline covalent organic frameworks directed by π-stacking. ChemRxiv *2026*. https://doi.org/10.26434/chemrxiv.10001788/v1.
12. Baldwin, L.A., Crowe, J.W., Pyles, D.A., and McGrier, P.L. (2016). Metalation of a Mesoporous Three-Dimensional Covalent Organic Framework. J. Am. Chem. Soc. *138*, 15134-15137. https://doi.org/10.1021/jacs.6b10316.
13. Yin, Y., Zhang, Y., Zhou, X., Gui, B., Wang, W., Jiang, W., Zhang, Y.-B., Sun, J., and Wang, C. (2024). Ultrahigh–surface area covalent organic frameworks for methane adsorption. Science *386*, 693-696. https://doi.org/10.1126/science.adr0936.
14. Yu, B., Tao, Y., Yao, X., Jin, Y., Liu, S., Xu, T., Wang, H., Wu, H., Zhou, W., Zhou, X., et al. (2024). Single-Crystalline 3D Covalent Organic Frameworks with Exceptionally High Specific Surface Areas and Gas Storage Capacities. J. Am. Chem. Soc. *146*, 28932-28940. https://doi.org/10.1021/jacs.4c09680.
15. Furukawa, H., and Yaghi, O.M. (2009). Storage of Hydrogen, Methane, and Carbon Dioxide in Highly Porous Covalent Organic Frameworks for Clean Energy Applications. J. Am. Chem. Soc. *131*, 8875-8883. https://doi.org/10.1021/ja9015765.

16. Chen, L., Gong, C., Wang, X., Dai, F., Huang, M., Wu, X., Lu, C.-Z., and Peng, Y. (2021). Substoichiometric 3D Covalent Organic Frameworks Based on Hexagonal Linkers. J. Am. Chem. Soc. *143*, 10243-10249. https://doi.org/10.1021/jacs.1c03739.
17. Li, H., Ding, J., Guan, X., Chen, F., Li, C., Zhu, L., Xue, M., Yuan, D., Valtchev, V., Yan, Y., et al. (2020). Three-Dimensional Large-Pore Covalent Organic Framework with stp Topology. J. Am. Chem. Soc. *142*, 13334-13338. https://doi.org/10.1021/jacs.0c06485.
18. Wang, Y., Liu, Y., Li, H., Guan, X., Xue, M., Yan, Y., Valtchev, V., Qiu, S., and Fang, Q. (2020). Three-Dimensional Mesoporous Covalent Organic Frameworks through Steric Hindrance Engineering. J. Am. Chem. Soc. *142*, 3736-3741. https://doi.org/10.1021/jacs.0c00560.
19. Li, H., Chang, J., Li, S., Guan, X., Li, D., Li, C., Tang, L., Xue, M., Yan, Y., Valtchev, V., et al. (2019). Three-Dimensional Tetrathiafulvalene-Based Covalent Organic Frameworks for Tunable Electrical Conductivity. J. Am. Chem. Soc. *141*, 13324-13329. https://doi.org/10.1021/jacs.9b06908.